Water permeation through polymer electrolyte membranes

by

Xiaoyan Luo

M.Sc., Simon Fraser University, 2012

Thesis Submitted in Partial Fulfillment of the
Requirements for the Degree of
Doctor of Philosophy

in the
Department of Chemistry
Faculty of Science

SIMON FRASER UNIVERSITY

Summer 2017

Approval

Name:	**Xiaoyan Luo**
Degree:	**Doctor of Philosophy**
Title:	***Water permeation through polymer electrolyte membranes***
Examining Committee:	**Chair:** Roger Linington Associate Professor

Steven Holdcroft
Senior Supervisor
Professor

Michael Eikerling
Supervisor
Professor

Byron D. Gates
Supervisor
Associate Professor

Paul C. H. Li
Internal Examiner
Professor

Andrew Herring
External Examiner
Professor
Chemical & Biological Engineering
Colorado School of Mines

Date Defended/Approved: July 26, 2017

Abstract

Water management has a major impact on the performance of the polymer electrolyte membrane fuel cells. An understanding of water permeation through polymer electrolyte membranes is crucial to offset the unbalanced water activity within fuel cells. The work presented in this thesis includes contributions that provide insight into internal and interfacial water permeation behavior of membranes, as well as insight into how membranes could be designed to enhance water management. Three types of *ex-situ* water permeation techniques are used in this thesis work. These are: liquid-liquid water permeation (LLP) in which both sides of the membrane are in contact with liquid water; liquid-vapor permeation (LVP) where one side of the membrane is exposed to liquid, and the other is exposed to vapor; and vapor-vapor permeation (VVP) where both sides of the membrane are exposed to water vapor. Three polymer electrolyte membrane systems were investigated under varied experimental conditions: degraded Nafion®, short side chain (SSC) perfluorosulfonic acid ionomer membrane, and an emerging class of anion exchange membrane, poly(benzimidazolium). Correlations between membrane series were drawn and compared to the commercially-available materials. It was found that membranes of smaller thickness, greater water volume fraction (Xv), and higher ion exchange capacity (IEC) result in a higher overall water permeability. However, the membrane thickness, Xv, and IEC do not dominate the rate of water permeation through the membrane interface. In contrast, the side chain length of the polymer is found to influence the interfacial water permeation, wherein membranes with longer side chain length are more water permeable at the interface.

Keywords: Water permeation; interface; proton exchange membrane; anion exchange membrane; fuel cell

To my husband (Yun), my daughters (Olivia and Sophia), my mother, my father, and my brother for their support, unconditional love and always believing in me.

Acknowledgements

I would like to express my gratitude to my senior supervisor, Professor Steven Holdcroft, for his support throughout the project. I appreciate his guidance and patience, especially when circumstances were difficult. I also appreciate his advice and scientific freedom.

I would also like to thank my supervisory committee, Professor Michael Eikerling and Professor Byron D. Gates, for their supervision of this thesis project. My internal and external examiners, Professor Paul C. H. Li and Professor Andrew Herring, for their valuable suggestions to improve my thesis.

I would like to thank the following people for providing materials for this thesis study. Professor Yongming Zhang provided short side chain perfluorosulfonic acid membranes used in Chapter 3. Dr. Andrew Wright synthesized HMT-PMBI polymers studied in Chapter 5. Mr.Thomas Weissbach cast all HMT-PMBI membranes. Mr. Benjamin Britton spray-coated HMT-PMBI membranes.

I am grateful for the endless technical support from the staff in the chemistry IT service (Steve Obadia and Fred Chin), the electronics shop (Pawel Kowalski, Ray Holland and John Van der Est), the glass shop (Bruce) and the machine shop.

A special mention should be paid to my proof readers: Dr. Poh Tan (SFU library writing service), Dr. Shaoyi Xu (Chapters 1- 5) and Dr. Tim Peckham (Chapter 6).

Thank you to my colleagues in the APC joint project between SFU and Ballard Power Systems: Dr. Lida Ghassemzadeh, Dr. Tim Peckham, and Mr. Thomas Weissbach.

I would like to thank all my past and current group members for their friendship and valuable discussions. Dr. Lida Ghassemzadeh and Dr. Jiantao Fan are also greatly appreciated for assisting with drawing the graphical illustrations of Figure 2.1, 3.2 and 3.13.

Table of Contents

List of Tables

List of Figures

List of Acronyms

AC	Alternative current
AEM	Anion exchange membrane
AEMFCs	Anion exchange membrane fuel cells
AFCs	Alkaline fuel cells
AFM	Atomic-force microscopy
CCM	Catalyst-coated membrane
dm	Degree of methylation
DVS	Dynamic vapor sorption
EIS	Electrochemical impedance spectroscopy
EOD	Electro-osmotic drag
EW	Equivalent weight
HMT-PMBI	Hexamethyl-*p*-terphenyl poly (dimethylbenzimidazolium)
IEC	Ion exchange capacity
LLP	Liquid-liquid water permeation
LSC	Long side chain
LVP	Liquid-vapor water permeation
MEAs	Membrane electrode assemblies
N117	Nafion® 117
NMR	Nuclear magnetic resonance
NR211	Nafion® 211
PBI	Polybenzimidazole
PE	Polyethylene
PEM	Proton exchange membrane
PEMFCs	Proton exchange membrane fuel cells
PFSA	Perfluorosulfonic acid
RH	Relative humidity
SANS	Small angle neutron scattering
SAXS	Small angle X-ray scattering
SEM	Scanning electron microscopy
SSC	Short side chain
TEM	Transmission electron microscopy

TFE	Tetrafluoroethylene
VVP	Vapor-vapor water permeation

List of Symbols

A	Geometrical active area of water permeation / m^2
a_w	Water activity
C_w^{wet}	Concentration of water in a wet membrane / M
$\Delta C_w^{interface}$	Apparent water concentration difference at the surface of a membrane / M
$\Delta C_w^{internal}$	Apparent water concentration difference within a membrane / M
D'	Effective water diffusion coefficient / $m^2\ s^{-1}$
E	Activation energy / kJ mol^{-1}
F	Faraday constant / C mol^{-1}
j	Current density / A cm^{-2}
J_{EOD}	Electro-osmotic drag flux / mol $m^{-2}\ s^{-1}$
J_{net}^a	In-situ net water flux derived from the anode stream / mol $m^{-2}\ s^{-1}$
J_w	Water permeation flux / mol $m^{-2}\ s^{-1}$
k'	Effective mass transfer coefficient / m s^{-1}
$k'_{LVP-interfacial}$	Effective interfacial LVP water permeation coefficient/ $mol^2\ m^{-2}\ s^{-1}\ kJ^{-1}$
$k'_{LVP-internal}$	Effective internal LVP water permeation coefficient/ $mol^2\ m^{-1}\ s^{-1}\ kJ^{-1}$
$k_{background}$	Water permeation rate of the “background” plastic film / mol s^{-1}
k_{eff}	Effective permeation coefficient / $mol^2\ m^{-2}\ s^{-1}\ kJ^{-1}$
M_{H_2O}	Molar mass of water / g mol^{-1}
M_0	Initial weight of the container with sample assembly / g
M_F	Weight of the container with sample assembly, after the measurement / g
N_d	Electro-osmotic drag coefficient
P	Permeance of water / $mol^2\ m^{-2}\ s^{-1}\ kJ^{-1}$
p(z)	Pressure, z / atm
P_{LLP}	Hydraulic water permeability / $mol^2\ m^{-1}\ s^{-1}\ kJ^{-1}$
P_{LVP}	Water permeability for liquid-vapor water permeation / $mol^2\ m^{-1}\ s^{-1}\ kJ^{-1}$
P_{VVP}	Water permeability for vapor-vapor water permeation/ $mol^2\ m^{-1}\ s^{-1}\ kJ^{-1}$
r_E	Rate of water evaporation / g s^{-1}
R	Water permeation resistance / kJ m^2 s mol^{-2}
$R_{interfacial}$	Interfacial water permeation resistance / kJ m^2 s mol^{-2}
$R_{internal}$	Internal water permeation resistance / kJ m^2 s mol^{-2}
$\frac{R_{interfacial}}{R}$	Ratio of interfacial resistance to total resistance of water permeation
[-SO_3H]	Analytical sulfonic acid concentration / M

T_g	Glass transition temperature / °C
Δt	Duration of the experiment / s
V_{H_2O}	Volume of water / m^3
V_{dry}	Volume of a dry membrane / m^3
V_{wet}	Volume of a hydrated membrane / m^3
W_{dry}	Dry weight of the membrane / g
X_v	Water volume fraction / %

Greek

$\mu^{o}_{liq\_\chi\,K}$	Standard chemical potential of liquid water at the temperature of χ K / kJ mol^{-1}
$\mu^{o}_{vap\_\chi\,K}$	Standard chemical potential of water vapor at the temperature of χ K / kJ mol^{-1}
$\Delta\mu_{LLP\_p\,(Z)}$	Difference in chemical potential between liquid water at 1 atm and *z* atm / kJ mol^{-1}
$\Delta\mu_{LVP\_RH\,(y)}$	Difference in chemical potential between liquid water at 1 atm and water vapor at relative humidity of y% / kJ mol^{-1}
$\Delta\mu_{VVP\_RH\,(y)}$	Difference in chemical potential between vapor at relative humidity of y% and 96% RH / kJ mol^{-1}
γ_T	Temperature coefficient / J mol^{-1} K^{-1}
δ_P	Pressure coefficient for water, 1 atm / J mol^{-1} bar^{-1}
$\mu_{liq\_p(z)}$	Chemical potential of liquid water under pressure (z) / kJ mol^{-1}
$\mu_{vap\_RH(y)}$	Chemical potential of water vapor at y% relative humidity / kJ mol^{-1}
μ'_{H^+}	Effective proton mobility / cm^2 s^{-1} V^{-1}
ρ_{dry}	Membrane dry density / g cm^{-3}
σ_{H^+}	Proton conductivity / s cm^{-1}
$\Delta\mu_W$	Chemical-potential gradient / kJ m^{-1}
η	Viscosity coefficient of water / m Pa s
λ	Hydration number
γ	Effective pore radium of a membrane / nm
θ	Contact angle / °

Chapter 1.

Introduction

1.1. Fuel cells

The current growing concerns about global pollution causes an increased drive to find less polluting energy sources of non-fossil origin.[1] One attractive alternative is the conversion of chemical energy into electrical energy. Fuel cells are promising energy conversion candidates. Compared to the combustion engines, fuel cells have the potential of higher energy conversion efficiency.[2] The chemical energy in fuel cells is directly converted into electrical energy, whereas in the case of combustion engines, the heat of combustion of the fuel is first converted to mechanical energy and then converted into electrical energy. The electrochemical reaction in fuel cells is akin to a battery, by storing the energy within the chemicals from an external storage tank. The electrical power of a fuel cell is continuously generated as long as the reactants are supplied. In addition, fuel cell systems are also regarded as environmentally-friendly, due to their low greenhouse gas emissions.[3] Therefore, interest in the use of fuel cells as highly efficient, clean energy conversion devices has been rapidly increasing over the past several decades.

There are five major types of fuel cells classified as an ion conductor (i.e., electrolyte): alkaline fuel cells (AFCs), proton exchange membrane fuel cells (PEMFCs), solid oxide fuel cells (SOFCs), phosphoric acid fuel cells (PACFs) and molten carbonate fuel cells (MCFCs).[4] The operating temperature is the key parameter differentiating the applications of each fuel cell type. Temperature can range from 25 °C to 900 °C or even higher temperature in the case of SOFCs.

1.2. Proton exchange membrane fuel cells

Among all the fuel cells types, proton exchange membrane fuel cells (PEMFCs) are preferred for automotive and portable devices, because they are well suited for quick start-up and operate at lower temperatures (~ 80 °C).[4,5] Hydrogen is a common fuel used in PEMFCs, a range of other fuels such as methanol and ethanol can be used as well. Nevertheless, the best performance in terms of power output is achieved with the reaction of pure hydrogen with oxygen.

The main components of PEMFCs include an anode, a cathode, and an electrolyte. In an operating PEMFC, hydrogen and oxygen are electrochemically combined to produce water and electricity, as illustrated in Figure 1.1. Catalyst materials (e.g., platinum) are used for both anode and cathode to meet the requirement of high fuel cell performance.[6] In addition, a polymer-based membrane is used as the electrolyte to conduct ions and to separate the fuels and the electrons. The driving force for the movement of the conducting ions is their concentration gradient formed between two electrodes. In a proton exchange membrane fuel cell, hydrogen is oxidized to liberate two electrons and two protons at the anode:

$$H_2 \rightarrow 2\,H^+ + 2\,e^- \qquad \text{Equation 1.1}$$

The protons are transported through a proton exchange membrane to the cathode, and the electrons flow through an external electronic circuit to power the load. At the cathode, the oxygen is reduced:

$$\frac{1}{2}\,O_2 + 2\,H^+ + 2e^- \rightarrow H_2O \qquad \text{Equation 1.2}$$

to give the overall cell reaction

$$H_2 + \frac{1}{2}\,O_2 \rightarrow H_2O \qquad \text{Equation 1.3}$$

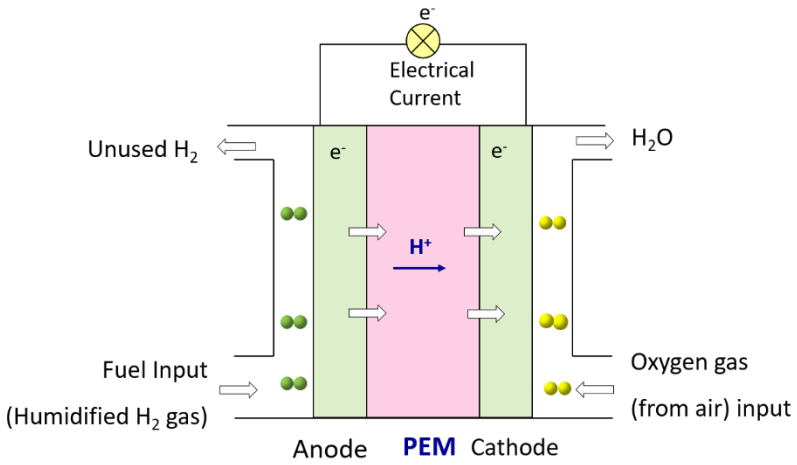

Figure 1.1 Schematic diagram of an operating proton exchange membrane fuel cell.

1.2.1. The challenges of proton exchange membrane fuel cells

- Currently, the high cost of proton exchange membranes (PEMs), the catalyst and fuel prevents large-scale (> 40 megawatts of power output) commercialization for transport applications (i.e., buses and vehicles).[7,8] Great efforts have been made to reduce the cost of PEMFCs,[7] including using inexpensive polymer membranes, reducing the amount of precious metal catalyst (or use of non-precious metal catalysts as an alternative), and utilizing of alternative fuels such as ethanol, and methanol.

- Durability is another key challenge facing the commercialization of fuel cells. Stability of materials, such as the membranes, are very important in developing membrane electrode assemblies (MEAs) that meet industry durability targets.[9,10] To be viable for automotive applications, PEMs must survive ten years in a vehicle and 5,500 hours of operation including transient operation with start/stop and freeze/thaw cycles.[9] The requirement for the chemical and mechanical stability of the thin membranes (typically no more than 20 microns thick) are significantly more demanding than the thicker membranes.[11] The stability of PEMs will be reviewed in Chapter 3.

- Water management is one of the key challenges in the commercialization of proton exchange membrane fuel cells (PEMFCs).[12,13] The balance of water within the fuel cell strongly affects its efficiency and reliability. The proton exchange membranes (PEMs)

are hydrophilic and will only conduct protons when there is water present. Hence, maintaining a high hydration level in the membrane is fundamental to ensure high proton conductivity.[14] Depending on the hydration state of the membrane, proton transport is associated with a drag of water molecules from the anode to the cathode in a running fuel cell. In order to prevent the anode side of the cells from drying out, an external fuel humidification system is often needed in the hydrogen fueled PEMFCs.[15] However, too much water is also a problem. During operation, excess water may be produced at the cathode and results in the cathode side of the cell flooding with water. In this case, oxygen can no longer reach the cathode to sustain the electrochemical reaction.[16] Therefore, PEMFCs must be maintained with a proper level of water-neither too little nor too much. Improper water management can lead to membrane dehydration and electrodes flooding. More details on the water management will be discussed later in Section 1.4 to Section 1.6 of this Chapter.

1.3. Proton exchange membranes

The proton exchange membranes (PEMs) (i.e. the electrolyte) is the key component of proton exchange membrane fuel cells (PEMFCs). Therefore, an increasing understanding of membranes and how they function can lead to improvements in fuel cell performance. The favorable membrane properties for PEMFCs include: excellent ionic conductivity, electron insulating (prevents short-circuiting between anode and cathode), high water permeation through membranes should be maintained to offset cathode flooding by allowing for back permeation of water from the cathode to anode.[2] minimal crossover of fuel especially for direct methanol fuel cells,[17] dimensional stability during fuel cell operation (minimal swelling and shrinking), good chemical, thermal stability and mechanical strength, durability under prolonged operation (~5000 h for transportation applications)[18], and low cost.[1] However, none of the reported membrane materials can meet all of these requirements.

1.3.1. The history of PEMs

Grubb first suggested the use of PEMs as the electrolyte of PEMFCs in 1959.[19] The first materials employed in PEMFCs were hydrocarbon-based membranes developed

by General Electric (GE) in the 1960s for National Aeronautics and Space Administration (NASA).[20] However, these hydrocarbon-based membranes were abandoned due to their low chemical stability. Current proton exchange membrane fuel cells (PEMFCs) utilize perfluorosulfonic acid (PFSA) ionomers, such as Nafion® as the electrolyte. The chemical structure of Nafion® is shown in Figure 1.2. Nafion®, invented and developed by E.I. Dupont company, has been the benchmark of PFSA ionomer membrane for low-to-medium temperature (25-80 °C) PEMFCs. PFSA ionomers are synthesized by copolymerization of perfluorinated vinyl ether monomers with tetrafluoroethylene (TFE). The higher stability of the C-F bond compared to C-H bond confers high resistance to strongly acidic or oxidizing environments. Therefore, PFSA membranes have higher chemical stability than hydrocarbon-based membranes. The equivalent weight (EW, g mol^{-1}) and thickness of the materials are commonly used to describe commercially available proton exchange membranes. The EW is determined by the ratio of the hydrophobic backbone (i.e., polytetrafluoroethylene) and hydrophilic side chains (i.e., pendent perfluorinated vinyl ether, terminated by sulfonic acid groups), and it is defined as the weight of dry Nafion® per mole of sulfonic acid groups when the material is in its H^+ form. All Nafion® membranes used in this thesis work possess EW of 1100, and are in different thickness. For example, Nafion® 211 which is fabricated by dispersion casting, has EW of 1100 and with a nominal dry thickness of 0.001 in. (i.e., 25 μm). The designation of “115” in Nafion® 115 refers to the membrane that was fabricated by extrusion and has an EW of 1100 with a nominal dry thickness of 0.005 in. (125 μm).[21]

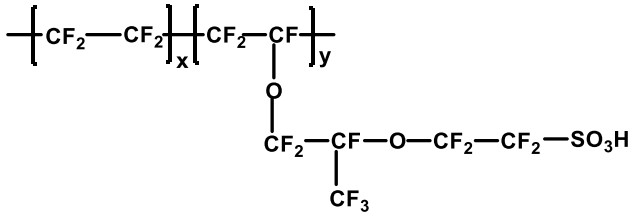

Figure 1.2 Chemical structure of Nafion®.

In the current perfluorosulfonic acid (PFSA) membranes, hydration must be high enough to produce sufficient conductivity. This requirement restricts the fuel cell operating temperature to ~ 80 °C (below boiling point of water) to prevent the membrane and catalyst layer from dry out. One current thrust of proton exchange membrane fuel cell research is to increase the operating temperature to 120 °C and above.[22] Nafion®, however, shows

low proton conductivity and poor thermal and mechanical stabilities under such conditions, which brings motivations for developing new polymer systems. One approach to maintain proton conductivity near and above the boiling point of water (90 to 160 °C) is to limit water loss from the ionic regions of the membrane by incorporating hydrophilic inorganic nanoparticles (e.g. ZrP,[23] Zeolite,[24,25] silicon dioxide (SiO_2),[26,27] TiO_2,[27]). These nanoparticles maintain water within the membrane even at elevated temperatures. Furthermore, there has been a lot of interest in polymer membranes that incorporated with acids, such as phosphoric acid, to replace the water in the membrane, due to the high boiling point of these acids.[28-30] However, these additives incorporated methods can be problematic, because the additives might be leached out under the fuel cell operation conditions, resulting in reduced fuel cell performance.

Changing the equivalent weight (EW) of the membrane by shortening the side chain length of polymer is a promising strategy to improve the durability and conductivity of membranes at high temperatures.[31] Figure 1.3 shows the chemical structure of PFSA ionomers with shorter side chain length than Nafion®. The so-called short side chain (SSC) PFSA ionomers were first synthesized by Dow Chemical Co., and commercialized by Solvay Solexis under the trade name of Aquivion® (-previous Hyflon Ion®). They have polymer structure akin to Nafion®, yet with shortest side chain length among the reported PFSA structures.[32] This type of PFSA membranes can theoretically be prepared with lower equivalent weight (EW) for a normalized polymer molecular weight. For a given EW, more tetrafluoroethylene (TFE) units are present in the SSC back-bond, providing a higher degree of crystallinity and higher glass transition temperature (T_g) relative to Nafion®.[33] These advantages that SSC PFSA membranes possess confer less membrane swelling, possibly higher conductivity and better mechanical stability, and consequently better fuel cell performance under high temperature operating condition.[34,35] Moreover, the absence of the ether group and the tertiary carbon also favors better stability for SSC PFSAs, making them more suitable for working at harsh fuel cell conditions.[35,36]

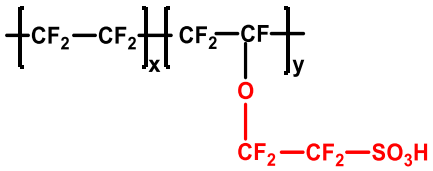

Figure 1.3 Chemical structure for short side chain (SSC) perfluorosulfonic ionomer membranes.

1.3.2. The challenges of PEMs

Even though PFSA membranes are the leading materials in the proton exchange membrane fuel cells (PEMFCs), membranes do have some drawbacks. The polymer is expensive to prepare and process due to its large number of C-F bonds.[37] Also, the polymer can not be easily dissolved by most solvents, which makes the membrane fabrication very challenging. Another drawback arises from expensive noble catalysts (e.g., Pt) used in proton exchange membrane fuel cells. Due to the utilization of strong acidic electrolytes, non-noble catalysts are usually found less favorable.[6,38,39]

1.4. The morphology of proton exchange membranes

In the dry state, the membrane behaves like an ionic insulator.[40] However, when membranes are exposed to an external water source, ionic groups in the membrane are hydrated, resulting in enhanced proton conductivity, which is critical to sustain desirable cell performance.[41] The conduction of ions relies on the presence of water. Thus, the morphology of hydrophilic domains in a polymer membrane is the predominant factor for proton conduction. Once hydrated, the membrane has a phase-separated nanostructure where interconnected water-swollen ionic-domains facilitate water and ion transport, which is illustrated in Figure 1.4.[21,42]

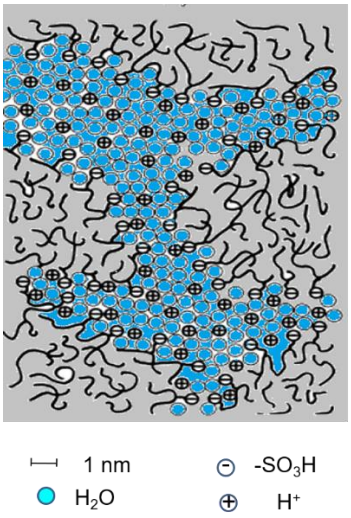

Figure 1.4 Schematic representation of hydrated Nafion® microstructure. (Adapted from ref.[43] with the permission of Elsevier, Copyright 2001)

1.4.1. The proposed structural models for proton exchange membranes

A variety of the scattering experiments were conducted to study the morphology of the Nafion® membranes. However, due to the rather complex nature of the membrane materials, so far, only simple morphological models that involve specific assumptions of structure have been proposed for Nafion®. Gierke[44] proposed the first model for Nafion®, cluster network model, assuming that both the ions and the sorbed water are all in spherical clusters, as illustrated in Figure 1.5. The diameter of these spherical water clusters was ~ 2 nm in dry state and can be increased to ~ 4 nm when the membrane is in a completely wet condition. In such model, the counter-ions, the fixed sites, and the swelling water phases are separated from the fluorocarbon matrix into approximately spherical domains which are connected by short narrow channels.

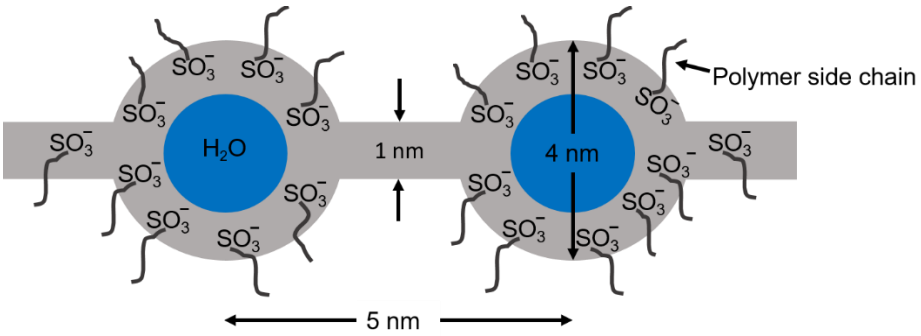

Figure 1.5 Schematic representation of hydrated ionic aggregates in PFSA ionomer membranes. (Adapted from ref.[45] with the permission of Wiley, Copyright 1981)

Several other morphological models have since been reported.[46-48] More recently, a water film-like model was proposed by Kreuer group (shown in Figure 1.6) for Nafion® membranes,[49] wherein the water film was suggested to act as a charged "glue" to keep the opposite charged polymer sites together.

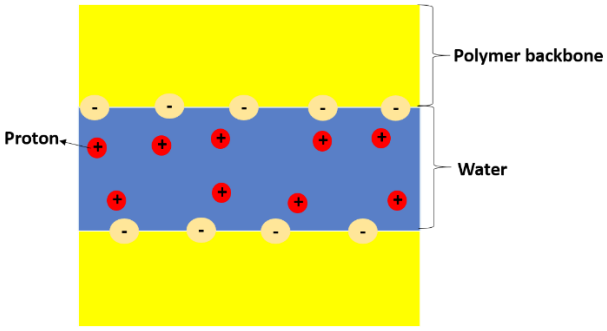

Figure 1.6 Schematic illustration of water film-like morphology of Nafion® membranes. (Adapted from ref. [49] with the permission of Wiley, Copyright 2013)

Allen and Weber et al. proposed the first nano-scale 3D views of the internal structure of hydrated Nafion® obtained by analytical transmission electron microscopy.[50] As shown in Figure 1.7, the diameter of the spherical cluster is ~ 3.5 nm for the dry membrane. When the membrane is in the hydrated condition, the hydrophilic sulfonic-acid containing phase formed an interconnected channel-type network, and the domain spacing is ~ 5 nm.

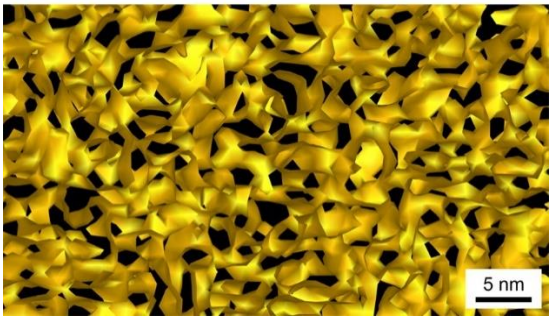

Figure 1.7 3D Nanostructure of hydrated Nafion® membrane obtained through cryo-TEM tomography. The hydrophilic domains are shown in gold. (Adapted from ref.[50] American Chemical Society, Copyright 2015.)

Experiments and modeling studies have been undertaken to understand the morphology of short side chain (SSC) perfluorosulfonic acid (PFSA) membranes.[33,51-54] It is reported that the morphology of SSC PFSA membrane is akin to Nafion®, in terms of hydrophilic/ hydrophobic phase-separated morphology. However, the size of hydrophilic cluster is different.

Even though numerous models that have been proposed, the exact morphology of the water-containing region of proton exchange membranes, is still under debate due to the inhomogeneous nature of the membranes when hydrated.[21] Nevertheless, these membrane models all suggest that a continuous aqueous phase composed of "water-channels" is formed due to nanophase separation of hydrophilic side chains and hydrophobic backbones at a given hydration level. The shape and size of these water channels vary with the amount of water uptake by the membrane.

1.5. The state of water and proton transport through membranes

The hydrophilic/hydrophobic nanophase separation nature of proton exchange membranes (PEMs) gives rise to different water domains and consequently controls the water transport rate within the membrane. These water domains strongly relate to the complex interactions between water and the membrane matrix.[43,46,47,55] Different water states, thus, have been proposed to exist in the membranes.[56] Water molecules that do not interact strongly with the polymer matrix would exhibit bulk-water dynamics, whereas

the water bound to the polymer hydrophilic groups would exhibit slower dynamics. Based on the order of decreasing hydrogen-bonding strength to the polymer, two types of water were suggested:[57] a) bulk-like water, which is not hydrogen bonded to the polymer; and b) bound water (strongly hydrogen bonded water to the charged ion groups in the membrane. As illustrated in Figure 1.8, in the center of the pore, water tends to have properties similar to bulk water and nearly bulk-like diffusion coefficients. However, outside of the pore center, the water molecules are strongly bound to the ionic groups (e.g., H^+) associated with the polymer.[58] The driving force for the mass transport of water molecules is the concentration difference between two clusters. The amount of water in the membrane and its interaction with the polymer can affect the membrane's structure, such as the morphology of the hydrophilic domains and their sizes.[41] As shown in the illustration in Figure 1.8, reducing the humidity in the membrane lowers the amount of bulk water present in the pore and alters the size of the hydrophilic pore. For example, as illustrated in Figure 1.8(d), in this case, bulk water in the pore is absent. The remaining water in the pore is highly polarized and confined to very small regions.

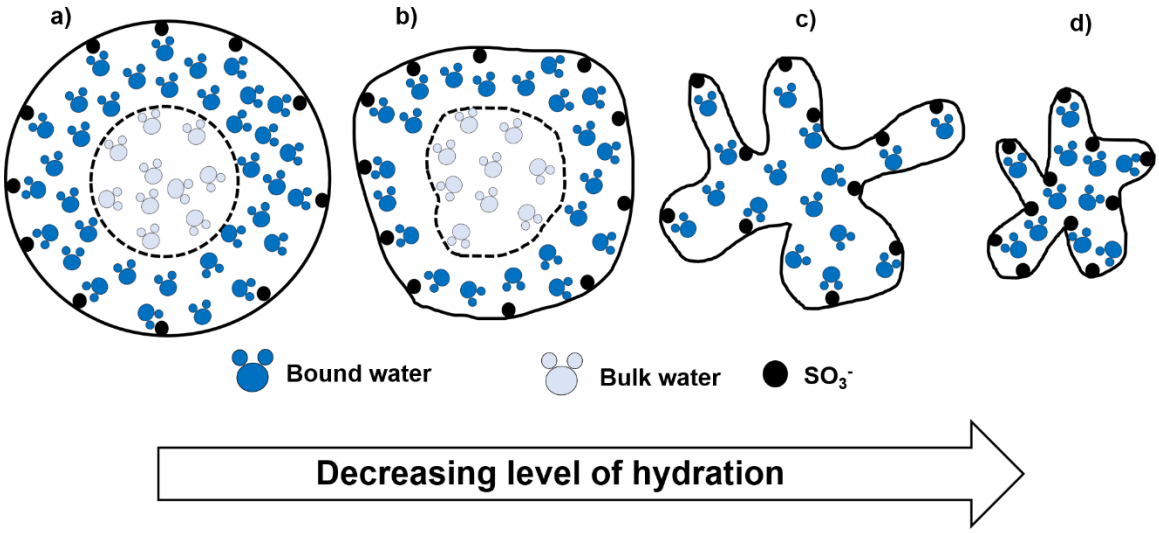

Figure 1.8 **Schematic diagram illustrating the different types of water in the hydrophilic pore of a Nafion® membrane. (Adapted from ref.[58] with the permission of American Chemical Society, Copyright 2006.)**

During operation of the proton exchange membrane fuel cells (PEMFCs), charge carriers (i.e., H^+) are transported through the membranes. The proton conductivity of a fully hydrated Nafion® membrane is ~ 100 mS cm^{-1} for the temperature ranging from 25 to 80 °C and decreases significantly with lowering of the level of hydration.[4,11,18] In the

presence of water, protons in the Nafion® membranes are strongly associated with water molecules to form aggregates, such as H_3O^+(Hydronium ion); $H_5O_2^+$(Zundel ion); and $H_9O_4^+$(Eigen ion).[59,60] Depending on the hydration level of the membrane, three transport mechanisms are proposed.[61,62] These mechanisms are the “surface” mechanism, the “Grotthuss” mechanism, and the “vehicle” mechanism, as illustrated in Figure 1.9.

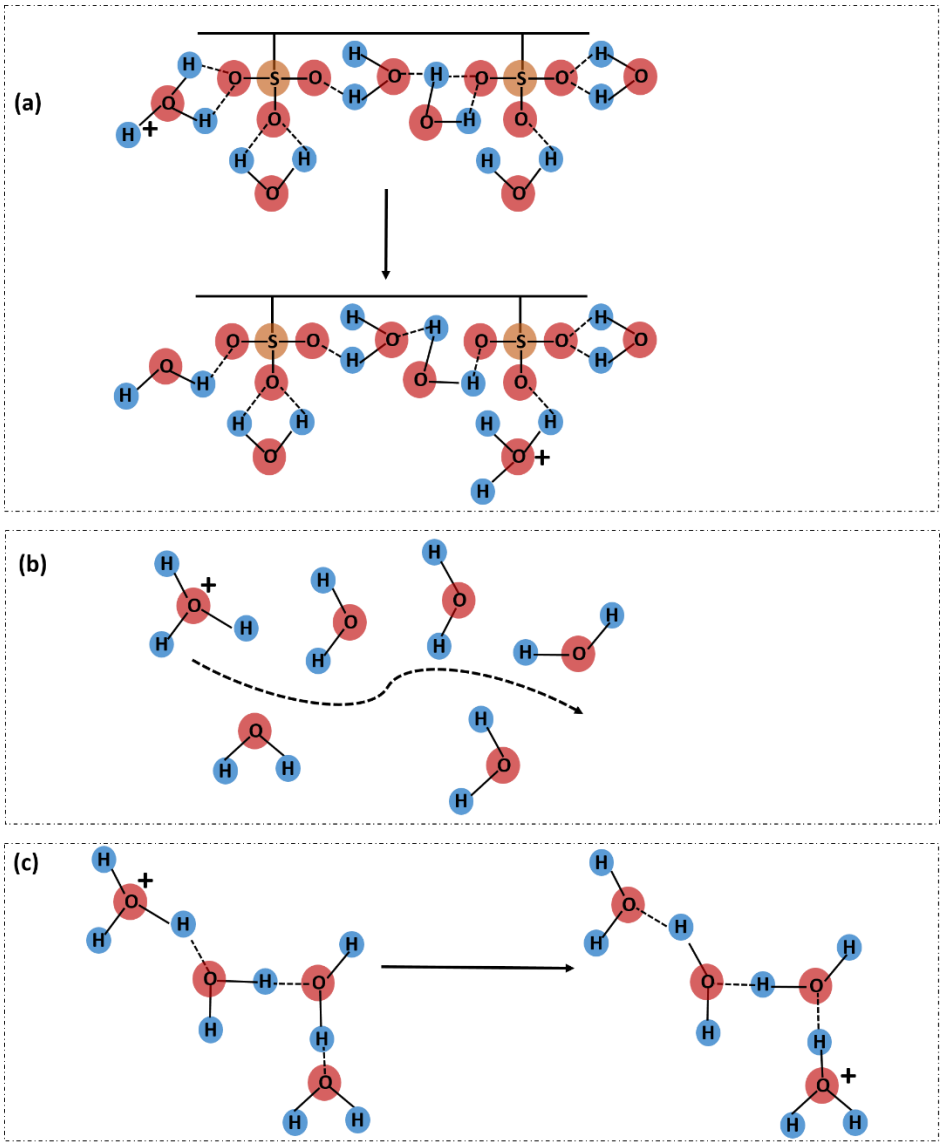

Figure 1.9 Simplified schematic of proton transport mechanisms in Nafion®. (a) Surface mechanism, (b) Vehicle mechanism and (c) Grotthuss mechanism.

At low hydration level, no bulk water is present. Proton transport is limited, and the movement of protons happens through surface mechanism (Figure 1.9 (a)), where H_3O^+

"hop" between the sulfonic acid groups along the hydrophilic pore surface. The rate of proton transport is directly dependant on the distance between two adjacent sulfonic sites. The shorter distance facilities faster proton transport, which is a reason for SSC PFSA membranes shown improved proton conductivity and better fuel cell performance than Nafion® at high temperature and low relative humidity conditions.[31] At higher hydration levels, the hydrophilic channels form continuous water pathways from cluster to cluster. Thus, the liquid phase in the membrane is well inter-connected. The interactions between the sulfonic sites and bulk water are reduced. Larger aggregates, such as $H_5O_2^+$ (Zundel ion) and $H_9O_4^+$ (Eigen ion) are present. As a consequence, protons transport through vehicle mechanism and Grotthuss mechanism. The vehicle mechanism (see Figure 1.9 (b)) is based on molecular diffusion process, where water molecules (e.g., $H_5O_2^+$ and $H_9O_4^+$) are used as a vehicle to transport protons. The Grotthuss mechanism (see Figure 1.9(c)) describes structured diffusion in the "water pool" where protons are transferred down a chain of hydrogen bonds followed by the bond formation and cleavage. The rate of proton transport depends on the rate of breaking and reforming of hydrogen bonds in the Grotthuss mechanism. The rapid transformation between the Zundel ion and the Eigen ion is the reason for rapid proton transport in proton exchange membrane, and thus proton transport via the Grotthuss mechanism is suggested to be faster than the vehicular type.[63]

1.6. Water transport through membranes

In addition to other critical functions (e.g., conduct protons and separate reactants), the membranes also act as a water transport medium to maintain proper hydration levels across the proton exchange membrane fuel cells.[64,65] If the hydration level across the membrane is too low, poor ion conduction results.[66] If the hydration level in the cell is too high, excess water may flood pores in the reaction sites on the electrodes.[67]

To achieve optimal water management in the cell, a highly water-permeable proton exchange membrane is required to facilitate the cathode water removal towards the anode.[68] Thus the problem of cathode flooding and anode dehydration could be solved. In addition, from a system operating perspective, making use of water produced at cathode to humidify the dry anode is beneficial, so that external humidifiers may not be needed. However, this process requires precisely controlling the water permeation rate

through the proton exchange membranes (PEMs) and electrodes. Therefore, it is crucial to understand how the rate of water transport through PEMs depends on polymer structure and morphology. In fact, water transport through PEMs have drawn massive attentions as part of general strategies of mitigating issues associated with water management and improving the fuel cell performance.[69,70] However, the role of polymer structure and morphology in water transport through membranes remains poorly understood.

In the past decade, water transport through PEMs has been studied in *in-situ* and *ex-situ* conditions. The large body of work under *in-situ* condition is focused on measuring the net water transport through PEMs.[71-78] This net water flux is quantified as the amount of water collected from anode outlet subtracting the one (humidified gas) introduced to anode. However, as illustrated in Figure 1.10, *in-situ* water transport through PEMs is complicated by different water resources. Water molecules are dragged by migrating protons (so called electro-osmotic drag) from the anode to the cathode.[79] In addition, there are water generation at the cathode, back-permeation of water from the cathode to the anode, water enters the system through humidifier and evaporates through electrodes.[80,81] Therefore, it is challenging to separate these contributions from the net water transport through fuel cell, which in turn have prevented in-depth discussions on the water transport through proton exchange membranes in the *in-situ* approach. In contrast, under *ex-situ* conditions, water transport through membranes can be studied as a function of applied gradients (i.e., relative humidity and hydraulic pressure). Thus, it can decouple the contributions of different water fluxes.

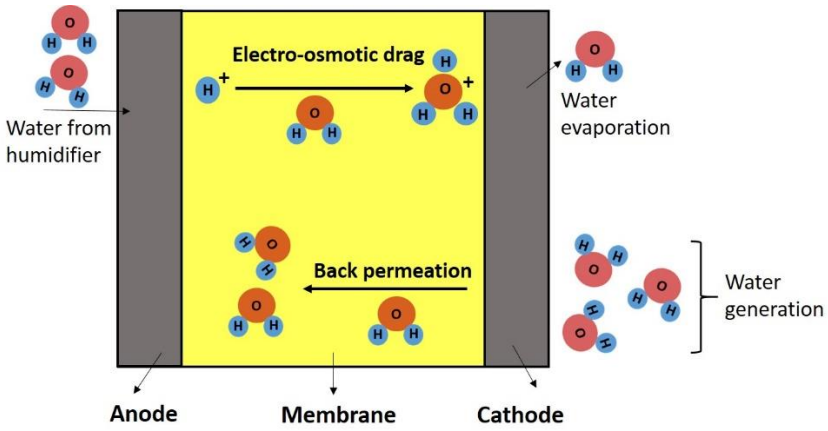

Figure 1.10 Schematic illustrating modes of water transport, uptake into proton exchange membrane fuel cell.

1.6.1. Ex-situ measurement

Ex-situ water transport through membranes is generally determined using experimental methods such as dynamic vapor sorption (DVS),[41,82] permeation,[13,64,71,83-87] and pulsed-field gradient spin-echo (PGSE) nuclear magnetic resonance (NMR).[88-91] These experiments provide useful information on the process of water transport through membranes (mostly Nafion®). However, a complete understanding of the water-transport mechanism is still under investigation.

Most studies assumed water transport through the membrane by diffusion. Diffusion coefficients are calculated from the measured transport rates. Diffusion coefficients determined by water sorption measurements give the smallest values ($\sim 10^{-8}$ cm^2/s);[84,92-99] permeation gives intermediate values of water diffusion coefficient ($\sim 10^{-7}$ cm^2/s);[64,85,100-106] and NMR measurements gives the highest values (10^{-6} cm^2/s).[81,90,91,107-114] Therefore, the large differences of diffusion coefficient obtained from these three methods make the results less comparable. In addition, these techniques do not capture the same information about water transport.

The NMR measurement can determine the self-diffusion of water in the membrane. However, NMR measurements provide a homogenous water environment, where there is no water activity gradient. In fact, in a typical operating fuel cell, water usually transports through membranes under the condition where water activity gradients exist.

Water sorption in the PEMs are commonly investigated using time-dependent gravimetric measurements (e.g., DVS analyzer). Most studies rely on measuring the change in the mass of the membrane with time at a given temperature and relative humidity, from which diffusion coefficient is determined. However, water sorption in the membranes is a complicated process, which involves interfacial water transport at the membrane interface, water diffusion in the membrane, a solvation reaction between ionic charge groups and water, as well as swelling and relaxation of the polymer network.[65,115] In addition, similar to the condition of the NMR experiment, there is no water activity gradient in the water sorption experiment. As a result, water sorption is problematic for determining water diffusion coefficient unless all aspects of transport are considered and carefully modeled.

Permeation experiment is usually performed under the condition of different water activities across both sides of the membrane. Thus, compared to the experiments of NMR and water sorption, permeation experiment is more closely approximate the transport of water into and through the membrane occurring in an operating fuel cell, where water transport at the membrane interfaces as well as diffusion through the membrane are present during the permeation process.[87] Therefore, the focus of this thesis work is the water transport through membranes by permeation experiments.

1.6.1.1. Water permeation

The first study of gas permeation through a polymer was conducted by Thomas Graham in 1829.[116] During the 1950s and 1960s, the permeation of synthetic membranes to permanent gases (O_2, N_2) and vapor was studied extensively.[117] Researchers have attempted to explain specific mechanisms by which permeation occurs in polymeric systems, but there is no unified theory to explain this phenomenon.[118]

Water permeation through polymer membranes can be described mathematically using the following equation, assuming a Fickian process.[119]

$$J = -D_f \nabla C_W \qquad \text{Equation 1.4}$$

where C_W is the concentration of water and D_f is diffusion coefficient for steady-state (Fickian) diffusion, i.e., when the concentration does not vary with time.

Darcy's law (formulated by Henry Gaspard Philibert Darcy in 1856) can also be used to describe water permeation through the membranes:[120]

$$J = -K_H \nabla P \qquad \text{Equation 1.5}$$

where K_H is the water permeation coefficient of the membrane and ∇P is the pressure gradient.

These two laws are commonly used to understand and predict permeation through membranes. Both laws are similar and suggest water transfer through polymer

membranes proceeds through the following five consecutive steps (illustrated in Figure 1.11)[121]:

1) Water diffusion to the polymer membrane from a high chemical potential atmosphere.

2) Sorption of the water by the membrane at the interface with the high chemical potential atmosphere.

3) Diffusion of the water inside and through the polymer membrane.

4) Desorption of the water at the interface of the low chemical potential side of the membrane.

5) Diffusion of the water away from the membrane into the low chemical potential atmosphere.

The primary difference between Fick's and Darcy's laws is the assumption of the pressure differential through the membrane.[122] The pressure is assumed to be uniform through the membrane and equal to the higher chemical potential side in the Fick's law model. However, in the Darcy's law, the pressure is assumed to drop uniformly across the membrane.[121,122]

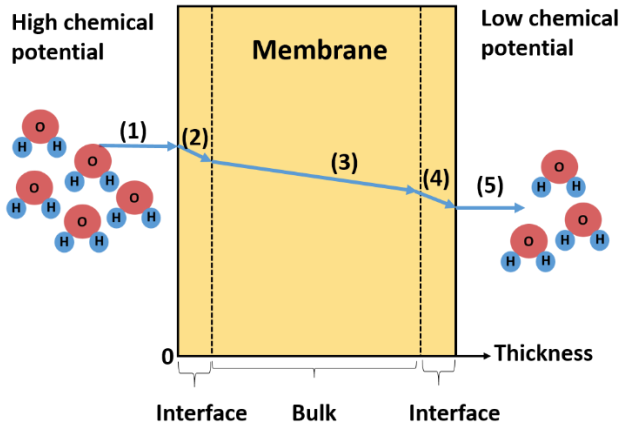

Figure 1.11 Schematic diagram of water transport through a membrane

Ex-situ water permeation through proton exchange membranes (mostly Nafion® membranes) is generally investigated using a permeation cell where the membrane is exposed to an applied gradient by controlling the relative humidity (RH) or hydraulic pressure (typically done with liquid water) at both surfaces of the membrane. For gases,

water flux, J_w, was measured under the conditions of different RH gradients across the membrane, $\Delta RH = RH_1 - RH_2$.[71,83-86] For liquids, a hydraulic pressure gradient is applied on the membrane and the responding water flux is then measured.[11,13,123] Three typical water permeation experiments were reported in literature,[71,13,86] and the details regarding these experiments are summarized in Chapter 2 and briefly in the following points:

1) Liquid-vapor permeation (LVP)- wherein one side of the membrane is in contact with liquid water and the other side is exposed to water vapor. The driving force for water permeation is controlled by varying the relative humidity of the water vapor side.
2) Vapor-vapor permeation (VVP)- wherein both sides of the membrane are exposed to water vapor, and the driving force for water permeation is created by the relative humidity difference on both sides of the membrane.
3) Liquid-liquid permeation (LLP)- wherein both sides of the membrane are in contact with liquid water and the driving force for water permeation is created by applying hydraulic pressure.

Our previous studies examined the impact of membrane thickness on water vapor permeation through Nafion® membranes. It was found that water permeation rates do not increase linearly with increasing thickness.[13]. However, Duan et al.[123] shown that the liquid water permeation rate increases with decreasing thickness of Nafion® membranes. In general, the water permeability from liquid is higher than that from humidified water vapor for a given applied gradient of driving force,[83,13,106] though the actual flux of liquid transport is often lower due to a smaller accessible range of the applied gradient.

1.6.1.2. Liquid water permeation vs. vapor water permeation

A membrane in contact with liquid water on both sides promotes a flux if a pressure gradient exists. Liquid/liquid permeation experiments are different from the permeation experiments in vapor. As illustrated in Figure 1.12 (a), when exposing a Nafion® membrane to liquid, the fluorocarbon groups are repelled from the polar environment and the ionic species are immediately attracted and “diffuse” to the outermost of the surface.[124] This surface rearrangement facilitates rapid permeation of water into the membrane bulk. Also, it seems that liquid/liquid conditions result in negligible interfacial permeation

resistance,[13,85,97,103,104] due to this rearrangement of the membrane's surface ionic species in liquid.

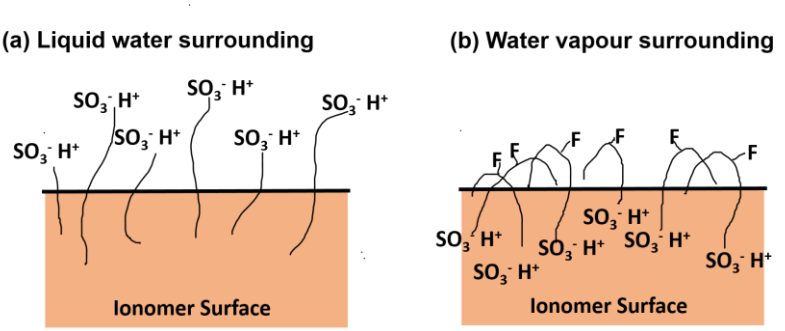

Figure 1.12 Schematic diagram illustrating a Nafion® membrane surrounded by (a) liquid water, and (b) water vapor. (Adapted from ref. [124] with the permission of American Chemical Society, Copyright 2000)

As illustrated in Figure 1.12(b), unlike the case of liquid water exposure, vapor exposure can not cause a fast rearrangement of the surface ionic species in the membrane. The reason is because the low attractive force for driving ionic species migration to the surface, due to the relatively low water content in the vapor phase. Thus, water vapor molecules from the outside are repulsed by the hydrophobic surface and cannot entirely "diffuse" into the bulk.[124]

The Freger group compared surface structures of Nafion® membranes in water vapor and liquid using grazing incidence SAXS (GISAXS), atomic-force microscopy (AFM) and contact angle measurements.[125,126] Their study suggested that changing the membrane hydration levels from low to high, drastically altered the surface morphology. At high hydrations, the membrane surface structures are normal type micelles, whereas, at low hydrations, the surface structures change to tightly packed bundles of inverted micelles with aqueous cores and fused hydrophobic shells. Also, they used GISAXS to examine the surface structure of thin Nafion® films and found that Nafion® micelles in vapor at the surface tend to be separated and align parallel to the surface. In contrast, these micelles are preferentially oriented normal to the surface when exposing to liquid (as illustrated in Figure 1.13),[127] which indicated that the membrane has significantly lower water transport in vapor as compared to that under liquid water conditions. Zhao et al. ascribed this phenomena to reducing tortuosity of water channel in the membrane when exposing to liquid water in contrast to water vapor.[113]

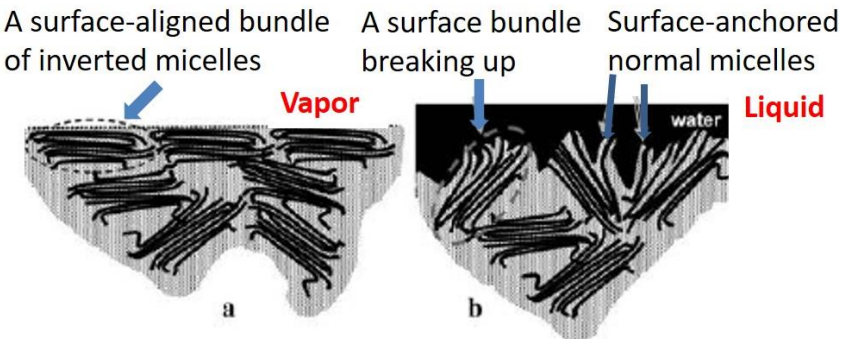

Figure 1.13 Schematic diagram of Nafion® membrane interface exposed to (a) vapor and (b) liquid water, showing the breakup of surface-aligned bundles to separate micelles upon transfer from liquid to water vapor. (Adapted from ref.[127] with the permission of American Chemical Society, Copyright 2011)

1.6.1.3. Internal and interfacial water permeation resistances

Recently, evidence shown that Nafion® membranes might possess different morphologies at the interface in contrast to the membrane bulk, and consequently have different interfacial transport properties compared to the membrane bulk.[13,85,88,124,128] As illustrated in Figure 1.14, the Nafion® membrane was suggested to possess a fluorine-rich "barrier" layer covering the entire membrane surface (~ a few nm thick),[129] thus, water transport rate is significantly hindered by this layer.

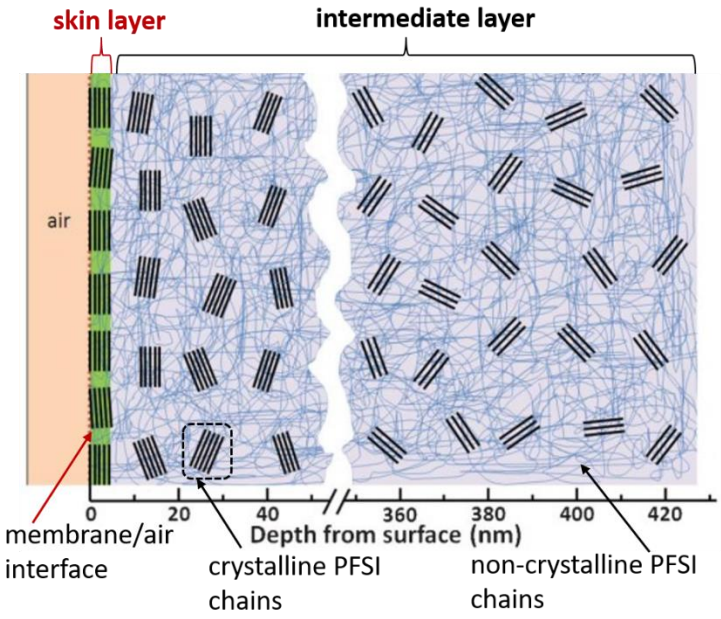

Figure 1.14 Schematic diagram showing the different regions in the Nafion® membrane based on data from synchrotron grazing incidence X-ray diffraction (GIXRD) (Adapted from ref.[129] with the permission of Royal Society of Chemistry, Copyright 2013)

Weber and Newman introduced chemical potential (μ) as the overall driving force for water transport to combine the driving forces of water activity and pressure.[5,78,130]

$$\Delta\mu\ (\mathrm{kJ}\ mol^{-1}) = \mathrm{RT}\nabla \ln a_w + V_W \nabla p \qquad \text{Equation 1.6}$$

where Δμ is the differential chemical potential, a_w is the activity of water, R is the universal gas constant, T(K) is the absolute temperature, $V_W(m^3)$ is the molar volume of water and p is the pressure (atm).[88]

The interfacial resistance and the bulk resistance to water transport can be determined from a steady-state permeation experiment by measuring the water flux (J_W) through the membrane at different chemical potential gradients ($\Delta\mu$, assuming local equilibrium, namely, there is only one overall gradient, that of chemical potential) and using membranes with different thickness.[5,78,130] The overall resistance to water permeation can then be written as:

$$R\ (kJ\ m^2\ s\ mol^{-2}\ ) = \frac{\Delta\mu\ (kJ\ mol^{-1})}{J_w\ (mol\ m^{-2}\ s^{-1})} = R_{interfacial} + R_{internal} \qquad \text{Equation 1.7}$$

$$R(kJ\ m^2\ s\ mol^{-2}\ ) = \frac{1}{k'_{1-interfacial}(mol^2\ m^{-2}\ s^{-1}\ kJ^{-1}\ )} + \frac{1}{k'_{2-interfacial}(mol^2\ m^{-2}\ s^{-1}\ kJ^{-1})} + \frac{T_M\ (m)}{D'(mol^2\ m^{-1}s^{-1}\ kJ^{-1})} \qquad \text{Equation 1.8}$$

where J_W is the water flux, the resistance (R) is the sum of the interfacial resistance ($\frac{1}{k'_{1-interfacial}} + \frac{1}{k'_{2-interfacial}}$) at both sides of the membrane and the internal resistance ($\frac{T_M}{D'}$), which is inversely proportional to the permeation coefficient (D'). Thus, the plot of the measured overall transport resistance to water (R) as a function of membrane thickness, T_M, gives a straight line (as shown in Figure 1.15 b). The slope of this plot gives the effective permeation coefficient (D'). The non-zero intercept, if it exists, gives the total interfacial resistance ($R_{interfacial}$). Surface water transport coefficient ($k'_{interfacial}$) can be calculated from the interfacial resistance ($k'_{interfacial} = 1/R_{interface}$). If the intercept is zero, then the interfacial resistance does not exist, meaning that the permeation process is not limited by interfacial water transport.

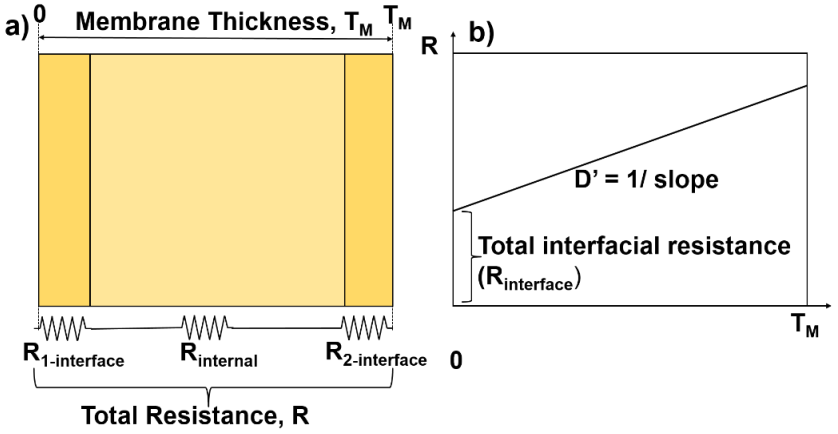

Figure 1.15 Schematic diagram of water transport resistances within a membrane.

The importance of the water transport through the gas/membrane interface was addressed in the study of Rivin et al.[94] and Zawodzinski et al.[81] Ever since the surface water transport coefficient ($k'_{interfacial}$) in Nafion® membrane have started to play a role in the water transport analysis. However, due to the novelty of this area, these surface water

transport coefficients ($k'_{interfacial}$) are less well studied in the literature than bulk permeation coefficients (D'). Nevertheless, the water transport resistance at the Nafion® membrane/vapor interface has been investigated,[83,104,113,97,131] disagreements yet exist. For instance, Zhao et al.[113] reported a humidity-independent interfacial resistance. However, Kienitz et al.[106] suggested a decrease in surface water transport coefficients ($k'_{interfacial}$) with humidity.

Moreover, a correlation was found to exist between the surface water transport coefficients and the fraction of hydrophilic surface area.[132] The inaccessible hydrophilic groups at the membrane surface was indicated to control the interfacial resistance, which can be determined using conductive atomic force microscopy (AFM). For example, O'Dea et al.'s AFM study suggested an increase in the conductive surface area with humidity, which can be an indication of an increase in overall hydrophilicity of the surface.[133] As shown in Figure 1.16, at ambient conditions, Nafion®'s surface morphology is similar to that proposed in the parallel-pore and bicontinuous network models, with the exception that hydrophilic domains are larger at the surface of Nafion® compared to the bulk. At hydrated conditions, a network of worm-like, insulating domains extends several micrometers over Nafion®'s surface with more conductive, water-rich regions. At dehydrated conditions, however, those features observed in ambient and hydrated conditions were absent. Instead, a low coverage of isolated hydrophilic surface domains was observed. These domains are similar in size to the ones at ambient conditions.

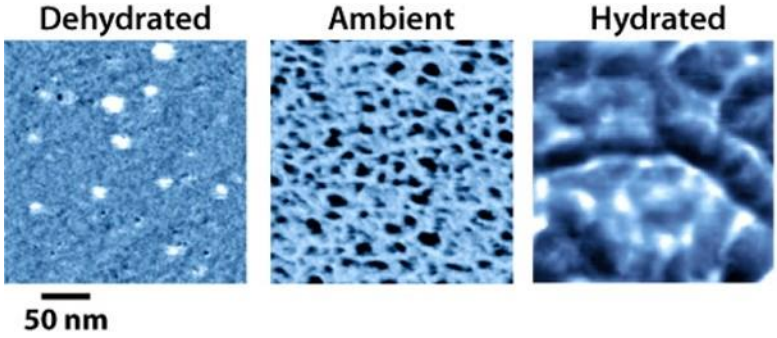

Figure 1.16 Atomic force microscopy image of evolution of Nafion® surface morphology with water content. (The ionic domains are shown in blue) (Reprinted from ref.[133] with the permission of American Chemical Society, Copyright 2013)

Bass et al.[125] recently investigated the surface of Nafion® membrane using GISAXS. It was suggested that the surface of Nafion® membrane is hydrophobic in vapor and becomes hydrophilic when the membrane is in liquid water. Therefore, the existence and origin of the interfacial resistance can be attributed to the polymer surface reorganization during swelling.

1.7. Thesis objectives

Water transport studies have largely focused on measuring the net water transport rates through an operating fuel cell (i.e., *in-situ*).[12,80,134-136] However, these net water transport rates are complicated by water fluxes from electro-osmotic drag and water fluxes via permeation. As a result, conditions that can offset the unbalanced water activity in the electrodes are not fully understood.[2] For this reason, studies on water permeation through polymer electrolyte membranes have drawn significant attention as part of general strategies for water management mitigations of fuel cells. In this thesis study, water fluxes were measured using *ex-situ* permeation setups, wherein experiments were conducted under controlled conditions.

As discussed in Section 1.6.1, the reported *ex-situ* water transport data are not consistent,[64,84,85,92-106] due to different experimental conditions used, which makes a fair comparison nearly impossible. Thus, in this thesis, a systematic ex-situ water permeation approach is conducted to mimic the conditions of water transport in an operating fuel cell.

Currently, the large body of studies of polymer electrolyte membranes were focused on Nafion® membranes, other promising polymer materials, such as short side chain (SSC) perfluorosulfonic acid (PFSA) membranes,[31,137] and anion exchange membranes[138,139] received much less attention. Furthermore, the impact of polymer architecture on the water transport is lacking, even though this knowledge is critical for the development of a new polymer electrolyte material, and consequently the performance of the fuel cell.

To this end, **the objective of this research is to gain a more complete understanding of the role of polymer structures on the water transport properties.**

A systematic analysis of *ex-situ* water transport was conducted on polymer electrolyte membranes under controlled conditions. Analysis obtained by electrochemical impedance spectroscopy (EIS) and contact angle Goniometer were coupled with water transport study for further investigation.

Chapter 1 is a literature review and introduction of this thesis project. Chapter 2 describes materials, water transport methods, and apparatus used in this research. In addition, complementary experimental methods, such as scanning electron microscopy and membrane density are included.

Chapter 3 is based on published work from this project which discusses the impact of free radical induced degradation on the water transport properties of proton exchange membranes (i.e. Nafion® 211). In this investigation, membranes were exposed in Fenton's reagent with a series of experimental time intervals. The water transport properties of degraded membranes were investigated. These data were compared with that of pristine Nafion® membrane.

The objective in Chapter 4 is to examine the impact of membrane thickness and temperature on the water transport properties of short side chain (SSC) perfluorosulfonic acid (PFSA) ionomer membranes. Membrane bulk and interfacial resistance were decoupled from the overall resistance to water transport and compared with long side chain PFSA- Nafion® membranes. Water permeations under different temperature conditions were performed. Comparisons of activation energy of water permeation were made between SSC PFSA and Nafion®.

In Chapter 5, the objective is to gain an understanding of the water transport through anion exchange membranes. An emerging class of anion exchange membrane, hexamethyl-*p*-terphenyl poly (dimethylbenzimidazolium) (HMT-PMBI) was used for water permeation study. The interfacial and internal water permeation resistance of HMT-PMBI membranes were decoupled from the overall water permeation resistance and compared against a commercialized anion exchange membrane (i.e., Fumapem® FAA-3) and a proton exchange membrane (Nafion®). In addition, the impact of a spray-coating catalyst layer on water permeation of the HMT-PMBI membranes was investigated.

Chapter 6 is a summary of this thesis work and a discussion of future work that may emerge from the understanding the relationship of structure and water transport properties of polymer membranes.

Chapter 2.

Sample characterization

2.1. Overview

This chapter introduces the characterization techniques used throughout this dissertation. Water permeation techniques were described in Section 2.2.1. Three types of water permeation methods including liquid-liquid (LLP), liquid-vapor (LVP) and vapor-vapor (VVP) water permeation, were employed to measure water permeation through membranes. Accordingly, differential chemical potentials of water permeation were calculated. Dynamic vapor sorption (DVS) analyzer was employed to measure water uptake of the polymer membranes. Titration was used for determining ion exchange capacity (IEC) of the baseline membrane (i.e., Nafion®). Electrochemical impedance spectroscopy (EIS) was employed to measure membrane proton conductivity. Density determination kit was applied to measure membrane dry density. Contact Angle Goniometer was employed to determine the water contact angle of the membrane.

2.2. Measurement of water permeation through membranes

2.2.1. Measurement of water permeation flux

Membranes were dried in a vacuum oven prior to use. Schematic diagrams of liquid-vapor (LVP), vapor-vapor (VVP) and liquid-liquid (LLP) water permeation setups are illustrated in Figure 2.1. Water permeation through the membrane was driven by controlling relative humidity gradient in the experiments of LVP and VVP, wherein water fluxes (J, mol m^{-2} s^{-1}) were measured based on gravimetric method. In the case of LLP experiment, water permeation through the membrane driven by a hydraulic pressure gradient, wherein water flux was measured using a mass flow meter. At least three replicates were performed for each measurement to obtain the standard deviation. The experimental procedures were performed according to published work,[13,71] and the details are described in the following Section.

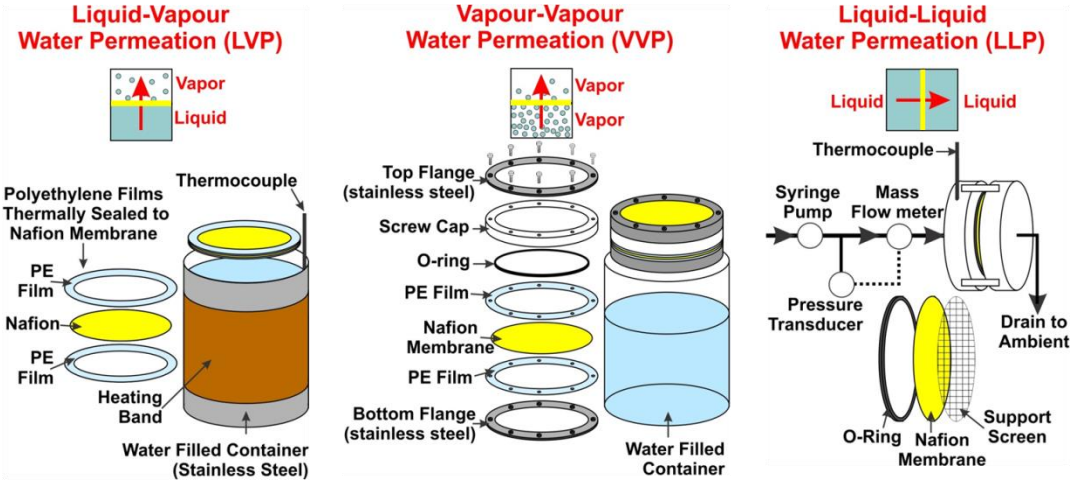

Figure 2.1 Schematic diagram of water permeation measurement setups using Nafion® as the membrane.

2.2.1.1. Measurement of LVP and VVP

As illustrated in Figure 2.1, in the experiments of liquid-vapor (LVP) and vapor-vapor (VVP) water permeation, membrane samples were cut into circular shape sandwiched between two polyethylene (PE) films using a laminator (Fusion™ 3100L, GBC). The PE films had a punched hole with a diameter of ~73 cm through which the membrane samples were exposed. The perimeter of the samples was sealed by the PE films to allow water permeation to occur only through the punched hole.

In the LVP measurement, there was a small gap between the perimeter of the PE/membrane/PE assembly and the wall of the container. Therefore, an identically-sized PE film (diameter of ~73 cm) without the punched hole was used to determine the background water flux $(k_{background})$ caused by the direct evaporation of water from this small gap (< 2 mm). This background water evaporation rate (< 20% of the evaporation rate of the overall membrane assembly) was subtracted from the overall evaporation rate of the container with the membrane assembly. For VVP measurements, the membrane was assembled into a leak-free sample container (< ~ 0.5% of the total rate of water permeation) filled with water.

To create a relative humidity (RH) gradient between both sides of the membrane, the LVP and VVP containers were placed in a computer-controlled environmental test chamber (SH-241, ESPEC North America Inc.). The RH gradient between both sides of

the membrane was controlled by varying the RH of the drier side. In liquid-vapor (LVP) water permeation, the membrane floated on the water surface and one side of the membrane directly contacted with liquid water, while the other exposed to water vapor. In the vapor-vapor (VVP) water permeation setup, one side of the membrane was exposed to nearly 100% relative humidity (RH), and the other side (i.e., drier side) was exposed to the chamber wherein RH can be controlled. Under such experimental condition, a stagnant layer of humidified air could form at the membrane/gas interface, due to the variation in gas convective velocities that may present in the environmental chamber. However, in the current LVP and VVP setups, the gas flow velocities at the evaporation interface of the membrane were sufficiently high to avoid this problem.[71,80]

Before performing experiments, the temperature and humidity of this chamber were calibrated with a dew point meter (HMT337, Vaisala Inc.) to confirm its controlling capability. Due to a large temperature drop (~ 10 °C) during fast water evaporation process occurred in the container, an external heating device was used in the LVP experiment. This external heating device included a thermocouple (K-type TC, Omega Engineering Inc.) which was sealed on the inside of LVP container, a 100 W flexible heater (Watlow Electric Mfg. Co) and an external temperature controller (Model 210, J-KEM Scientific Inc.) were applied to maintain a constant temperature. In the case of VVP, no external heating device was used, because a small temperature (~1 °C) drop was observed during the experiment.

At the beginning of experiment, the container with water and the PE/membrane/PE assembly was weighed to take the initial weight ($\mathrm{M_0}$) after the temperature was stabilized. The sample container was then removed from the humidity chamber at regular intervals to obtain the final weight ($\mathrm{M_F}$). The time interval (Δt) was recorded using a stopwatch (Traceable®, Fisher Scientific). The evaporation rate $(\mathrm{r_E})$ of water can be calculated using the following Equations:

$$\Delta M\ (g) = M_0 - M_F \qquad \text{Equation 2.1}$$

$$r_E(g\ s^{-1}) = \frac{\Delta M(g)}{\Delta t(s)} \qquad \text{Equation 2.2}$$

The water flux of LVP through the membrane is calculated using the following equations:

$$k_{background}(mol\ s^{-1}) = \left(\frac{r_E(g\ s^{-1})}{M_{H_2O}(g\ mol^{-1})}\right)_{background} \quad \text{Equation 2.3}$$

$$J_{LVP}(mol\ m^{-2}s^{-1}) = \frac{\left(\frac{r_E(g\ s^{-1})}{M_{H_2O(g\ mol^{-1})}}\right)_{Mem.} - k_{background}(mol\ s^{-1})}{A_{LVP}\ (cm^2)} \quad \text{Equation 2.4}$$

where $\mathrm{k_{background}}$ is the background water evaporation rate (depending on the RH, is < 20% of the evaporation rate of water through the membrane). $\mathrm{M_{H_2O}}$ is the molar mass of water (g mol^{-1}) and $\mathrm{A_{LVP}}$ $(\mathrm{cm^2})$ is the exposed area of the membrane.

Water flux for VVP is expressed below:

$$J_{VVP}\ (mol\ m^{-2}s^{-1}) = \frac{\left(\frac{r_E}{M_{H_2O}}\right)_{Mem.}(mol\ s^{-1})}{A_{VVP}\ (cm^2)} \quad \text{Equation 2.5}$$

where $\mathrm{M_{H_2O}}$ (g mol^{-1}) is the molar mass of water and $\mathrm{A_{VVP}}$ $(\mathrm{cm^2})$ is the exposed area of the membrane.

2.2.1.2. Measurement of liquid-liquid permeation (LLP)

A 25 mL syringe (Gastight # 1025, Hamilton Co. with PHD2000, Harvard Apparatus) filled with DI (18 MΩ) water from Millipore Gradient Milli-Q, a mass flow meter (20 µL min^{-1}, Bronkhorst HI-TEC) and a pressure transducer (PX302-100GV, Omega Engineering Inc.) were connected in series with 1/8" polytetrafluoroethylene (PTFE) tubing. The fully hydrated membrane was cut into ~ 3.28 cm^2 circles and installed in a cell made in-house, consisting of an O-ring and a PTFE coated stainless steel screen to prevent rupture of the membrane. Remove any air bubbles from the system before starting measurement. Labview software was used to control and monitor the whole system. For the experimental temperature higher than room temperature, the cell was heated on an external hot plate. Hydraulic pressure was applied to the membrane to drive water to permeate through. A constant flow of water throughout the system was maintained when the temperature and pressure (when the pressure deviation < 1%) were equilibrated. The water flux (J_{LLP}, mol m^{-2} s^{-1}) was calculated using the following equation:

$$J_{LLP}\ (mol\ m^{-2}s^{-1}) = \frac{j_v\ (m^3\ s^{-1}) \times \rho(g\ cm^{-3})}{M_{H_2O}\ (g\ mol^{-1}) \times A_{LLP}(cm^2)}$$ Equation 2.6

where $j_v\ (m^3\ s^{-1})$ is the volume water flux recorded by the mass flow meter. $\rho\ (g\ cm^{-3})$, $M_{H_2O}\ (g\ mol^{-1})$, and $A_{LLP}\ (cm^2)$ represent the density of water, molar mass of water, and the effective experimental area of the membrane, respectively.

2.2.2. Differential chemical potential of liquid and vapor water permeation through membranes

The chemical potential of water in liquid and in the vapor phase (1 atm) at various temperatures is given by [71]

$$\mu^o_{liq-\chi\ K}\ (kJ\ mol^{-1}) = \mu^o_{liq}\ + \gamma_{T\_liq}(T(\chi) - T_{STD})$$ Equation 2.7

$$\mu^o_{vap-\chi\ K}\ (kJ\ mol^{-1}) = \mu^o_{vap}\ + \gamma_{T\_vap}(T(\chi) - T_{STD})$$ Equation 2.8

where μ^o_{liq} and μ^o_{vap} are the chemical potentials of liquid water and water vapor (1 atm) at 298 K. Their values are -237.18 and -228.59 kJ mol^{-1}, respectively;[71] γ_T represents the temperature coefficient for the chemical potential of water in the liquid (γ_{T_liq}) and water vapor (γ_{T_vap}) phase:-69.85 and -188.74 J mol^{-1} K^{-1}, respectively.

From the standard chemical potential of water vapor ($\mu^o_{vap-\chi K}$), the chemical potential of water vapor at various relative humidity ($\mu_{vap\_RH(y)}$) were calculated according to Equation 2.9:

$$\mu_{vap\_RH(y)}(kJ\ mol^{-1}) = \mu^o_{vap-\chi\ K}\ + RT\ ln[\frac{y \times P_{sat-vap}}{P_{amb}}]$$ Equation 2.9

where $\mu^o_{vap-\chi K}$ was calculated according to Equation 2.8. R, T, and y are the universal gas constant, the temperature of the environment (K), and y is the relative humidity (%), respectively. $P_{sat-vap}$ (atm) and P_{amb} (atm) are the saturated vapor pressure at an experimental temperature and the ambient pressure, respectively.

The chemical potential of liquid water under pressure ($\mu_{\mathrm{liq\_p(z)}}$) was estimated using Equation (2.10),

$$\mu_{\mathrm{liq\_p(z)}}(kJ\ mol^{-1}) = \mu^{o}_{liq-\chi\,K} + \delta_P[p(z) - p_{STD}] \qquad \text{Equation 2.10}$$

where $\mu^{\mathrm{o}}_{\mathrm{liq}-\chi\,\mathrm{K}}$ was calculated using equation (2.7). $\mathrm{p(z)}$, $\mathrm{p_{STD}}$ and δ_P indicate the applied pressure, standard pressure and the pressure coefficient for water. Here, the standard pressure is 1 atm and δ_P is 1.807 J mol^{-1} bar^{-1}. [140]

The differential chemical potentials across the membrane generated by the LVP ($\Delta\mu_{\mathrm{LVP\_RH\,(y)}}$), VVP ($\Delta\mu_{\mathrm{VVP\_RH\,(y)}}$) and LLP ($\Delta\mu_{\mathrm{LLP\_P\,(Z)}}$) (kJ mol^{-1}) setups were calculated using equation (2.11), (2.12) and (2.13), respectively, according to the published work.[71,141]

$$\Delta\mu_{LVP\_RH\,(y)}(kJ\ mol^{-1}) = \mu^{o}_{liq-\chi\,K} - \mu_{vap\_RH\,(y)} \qquad \text{Equation 2.11}$$

$$\Delta\mu_{VVP\_RH\,(y)}(kJ\ mol^{-1}) = \mu_{vap\_RH\,(96\%)} - \mu_{vap\_RH\,(y)} \qquad \text{Equation 2.12}$$

where $\mu_{\mathrm{vap\_RH\,(96\%)}}$ and $\mu_{\mathrm{vap\_RH\,(y)}}$ are the chemical potentials at RH of 96% and y, respectively.

$$\Delta\mu_{LLP\_p\,(Z)}(kJ\ mol^{-1}) = \mu_{liq\_p(z)} - \mu^{o}_{liq-\chi\,K} \qquad \text{Equation 2.13}$$

where $\mu_{\mathrm{liq\_p(z)}}$ and $\mu^{\mathrm{o}}_{\mathrm{liq}-\chi\,\mathrm{K}}$ are the chemical potentials of liquid water under pressure $\mathrm{p(z)(atm)}$, and under the conditions of various temperature $\chi,(\mathrm{K})$ at the pressure of 1 atm, respectively.

2.2.3. Water permeability and resistance

2.2.3.1. Water permeability

Water permeation through polymer membranes is generally reported as a water flux. The problem with reporting data in fluxes is that these values are not only a function of the intrinsic properties of the membranes used but also depend on the operating

conditions of the experiments (e.g., water activity, pressure, and temperature): change the operating conditions, and all the permeation numbers change.[142] Thus, using flux causes the permeation data sets obtained under different operating conditions problematic. About 15 years ago, Wijmans J.G.[143] advocated that publications concerning permeation should report membrane performance data as intrinsic, driving force normalized properties: permeance and permeability.

In this study, water fluxes were converted to the water permeability ($mol^2\ m^{-1}\ s^{-1}\ kJ^{-1}$) using Equation 2.14:

$$Permeability\ (mol^2\ m^{-1}\ s^{-1}\ kJ^{-1}) = P\ (mol^2\ m^{-2}\ s^{-1}\ kJ^{-1}\ ) \times\ T_M\ (m) \qquad \text{Equation 2.14}$$

where permeance (P, $mol^2\ m^{-2}\ s^{-1}\ kJ^{-1}$) was estimated from the slope of a plot of water flux ($mol\ m^{-2}\ s^{-1}$) as a function of the differential chemical potential ($kJ\ mol^{-1}$). T_M is the membrane thickness under the given water permeation conditions, which was measured using a digital micrometer (± 0.001 mm, Mitutoyo).

2.2.3.2. Water permeation resistance (R)

Analogous to ohmic resistances in electrical networks, the resistance (R, $kJ\ m^2\ s\ mol^{-2}$ = 1.07 mΩ cm^2) to water permeation through membranes was calculated using differential chemical potential ($\Delta\mu$) divided by membrane water flux (J_w), as shown in Equation 1.7 (Chapter 1).

2.3. Water sorption

Liquid water sorption measurement was conducted using a gravimetric method. Membranes were soaked in liquid water and equilibrated in an environmental humidity test chamber (SH-241, ESPEC North America Inc.) at desired temperature for at least two days before taking the wet weight (W_{wet}). Dry weights (W_{dry}) were obtained after vacuum drying the membrane to a constant weight at 100 °C overnight and cooled in a desiccator.

A DVS-1000 instrument (shown in Figure 2.2, Surface Measurement Systems, London, UK) was used for the determining isothermal water sorption of membranes

equilibrated with water vapor of known relative humidity (RH). During operation, pre-set mixtures of water-saturated and dry nitrogen (pre-purified, Praxair Inc.) gases flowed across the membrane sample, and the weight change resulting from the absorption of the water that was recorded. The system consists of a microbalance; two matched weight quartz round bottom pans hung from a recording microbalance (± 0.1 µg) via two platinum wire hooks, water bottles, and the gas input lines. One of the quartz pans holds the membrane sample of interest and the other remains empty as a reference to subtract the possible error from the water condensation of the sample pan. The experimental temperature was controlled using a temperature controlled incubator (± 1 °C). Prior to use, the entire system was equilibrated at the temperature of interest. Membranes were loaded to the sample pan after carefully calibrated the microbalance with a platinum calibration weight. Experiments were fully automated by a programmed system. Water vapor of known relative humidity flowed across the sample at the desired rate, and weight recorded every 10 s. Relative humidity (RH) moved to the next step after constant sample weight was obtained. W_{dry} and W_{wet} were obtained when RH is 0% and any particular RH of interest (e.g., 40% RH).

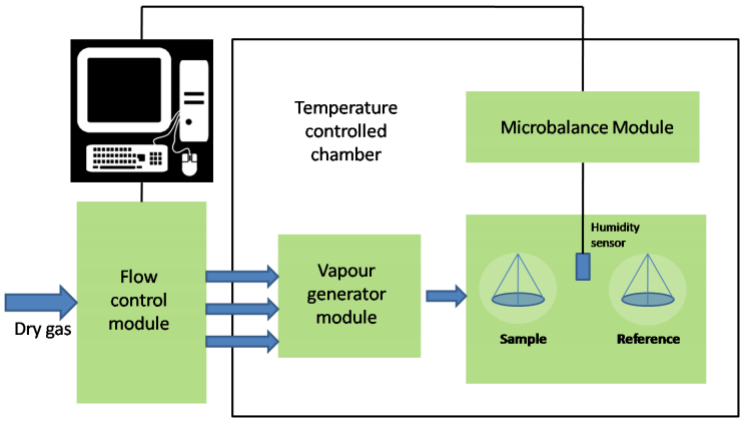

Figure 2.2 Schematic diagram of the dynamic gravimetric vapor sorption (DVS).

Volumes of dry membranes, V_{dry}, were calculated using Equation 2.15. [144]

$$V_{dry}(cm^{-3}) = \frac{W_{dry}\,(g)}{\rho_{dry}(g\,cm^{-3})} \qquad \text{Equation 2.15}$$

where W_{dry} is the dry weight of the membrane, obtained under 0% RH, and ρ_{dry} is the density of the dry membrane which is described in Section 2.5.

The volume of water (V_{H_2O}) in the membrane was determined by Equation 2.16.

$$V_{H_2O}(cm^{-3}) = \frac{(W_{wet} - W_{dry})(g)}{\rho_{H_2O}\ (g\ cm^{-3})} \quad \text{Equation 2.16}$$

where W_{wet} and W_{dry} are the wet and dry mass of the membrane, respectively. W_{wet} was obtained under a humidity of interest (e.g., 40% RH). ρ_{H_2O} is the density of water.

The volume of a hydrated membrane (V_{wet}) was calculated using the following equation:

$$V_{wet}(cm^{-3}) = V_{dry} + V_{H_2O} \quad \text{Equation 2.17}$$

The water uptake in the membrane was calculated using Equation 2.18.

$$Water\ uptake\ (\%) = \frac{(W_{wet} - W_{dry})(g)}{W_{dry}\ (g)} \times 100\%$$

Equation 2.18

The volume percentage of water in the membrane (X_v) was obtained by dividing the volume of water in the membrane by the volume of the wet membrane.

$$X_v = \frac{V_{H_2O}(cm^{-3})}{V_{wet}\ (cm^{-3})} \quad \text{Equation 2.19}$$

The hydration number (λ) which represents the number of water molecules that are contained in the membrane per functional group (e.g., -SO_3H in Nafion®). λ was calculated based on membrane water uptake and ion exchange capacity (IEC) using the following equation:

$$\lambda\ (\frac{mol\ SO_3^-}{mol\ H_2O}) = \frac{Water\ uptake\ (\%) \times 10}{18 \times IEC\ (mmol\ g^{-1})} \quad \text{Equation 2.20}$$

2.4. IEC of proton exchange membranes

Ion exchange capacity (IEC, mmol g^{-1}) of proton exchange membranes refers to the total number (in the unit of milli-equivalents) of ion exchange groups contained in one gram of dry polymer. IEC was obtained based on the acid-base titration method using a Metrohm 848 Titrino Plus Titrator. Membranes were soaked in 2 M NaCl overnight before being titrated with 0.01 M NaOH. Membranes were removed from sample vials after titration, washed with DI (18 MΩ) water and dried in a vacuum oven overnight. The dry weight of membranes (Na^+ form) was obtained after the samples were cooled in a desiccator. Three sample replicates were performed to obtain the standard deviation. IEC was calculated according to the following equation:

$$IEC\ (mmol\ g^{-1}) = \frac{(V_{NaOH,}\ (mL))\times(M_{NaOH,}(M))}{\left\{(W_{dry(Na+)} - 22\times(V_{NaOH,}(L))\times\left(M_{NaOH,}(M)\right)\right\}(g)} \qquad \text{Equation 2.21}$$

where V_{NaOH} and M_{NaOH} are the volume and concentration of NaOH, respectively, and $W_{dry(Na+)}$ is the dry sample mass in Na^+ form. 22 is the mole mass difference between Na and H.

The analytical acid concentration represents the overall free proton concentrations in the membrane, and was determined according to the following relationship:

$$[-SO_3H]\ (M) = \frac{W_{dry}\ (g)\times IEC(mmol\ g^{-1})}{V_{wet}\ (cm^{-3})} \qquad \text{Equation 2.22}$$

2.5. Membrane dry density (ρ_{dry})

Membrane dry density (ρ_{dry}) was calculated using an Ohaus density determination kit. Decane purchased from Fisher Scientific was used as the auxiliary solvent. Membranes were dried in a vacuum oven overnight before use. An Ohaus New Explorer® balance was used for obtaining the mass of the dry and wet sample. The experiments were performed at room temperature and ambient pressure based on three replicates for each sample. The sample dry density was calculated according to the following equation:[145]

$$\rho_{dry}(g\ cm^{-3}) = \frac{A\ (g)}{(A-B)(g)}\{(\rho_0, g\ cm^{-3}) - (\rho_L, g\ cm^{-3})\} + (\rho_L, g\ cm^{-3}) \qquad \text{Equation 2.23}$$

where ρ_{dry} is the dry density of sample. A and B are the sample weight in air and in the auxiliary liquid. ρ_0 and ρ_{L} are the density of air and the auxiliary liquid, respectively.

2.6. Proton conductivity and effective proton mobility

Proton conductivity defines the ability for a membrane to conduct protons. It was measured by electrochemical impedance spectroscopy (EIS) with a Solartron 1260 frequency response analyzer (FRA) within the frequency range 10 to 100 MHz using an in-plane, two-electrode configuration as illustrated in Figure 2.3. A strip of the membrane was sandwiched between two Pt electrodes and two Teflon blocks which have punched square shaped holes exposed to air. The entire conductivity apparatus was equilibrated with water vapor of known relative humidity (± 1.5% RH) at temperature of interest (± 0.1 °C) by placing it into a computer-controlled environmental test chamber (SH-241, ESPEC North America Inc.). To minimize experimental error, the temperature and RH were verified independently using a digital thermometer and a humidity sensor, respectively. Three samples were used for obtaining the standard deviation. A 100 mV sinusoidal AC voltage was passed along the plane of the sample.

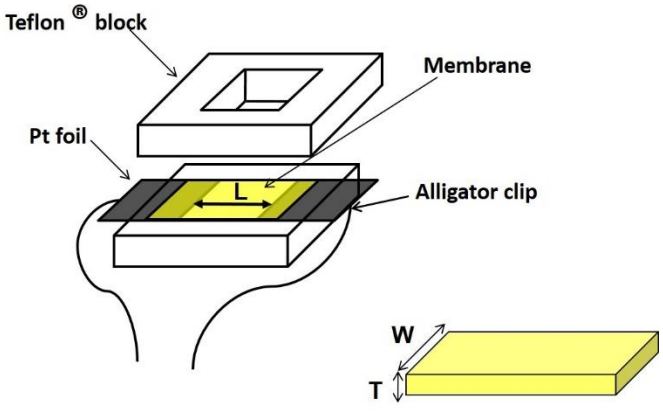

Figure 2.3 Schematic diagram of proton conductivity measurement and rectangular membrane sample dimensions.

Proton conductivity (σ_{H^+}, S cm^{-1}) was calculated using Equation 2.24:

$$\sigma_{H^+}\,(S\,cm^{-1}) = \frac{L\,(cm)}{R\,(\Omega)\times A(cm^2)}$$ Equation 2.24

where L (cm) is the distance between electrodes, R (Ω) is the ionic resistance of the membrane, and A (cm^2) is the cross-sectional area of the sample, which can be calculated using membrane thickness (T_M) and width (W).

The effective proton mobility (μ'_{H^+}) indicates how fast the protons move as a function of electric field strength, which was calculated according to the following equation:[66]

$$\mu'_{H^+}(cm^2\,s^{-1}\,V^{-1}) = \frac{\sigma_{H^+}\,(S\,cm^{-1})}{F\,(C\,V^{-1})\times[-SO_3H](M)}$$ Equation 2.25

where F is the Faraday constant, $\sigma_{H^+}$is the proton conductivity of the membrane, and [-SO_3H] is the analytical acid concentration of the membrane.

2.7. Membrane effective pore radius

Even though the calculation of membrane effective pore radius was based on incorrectly assuming the membrane is a porous, rigid medium filled with liquid water, the values of effective pore radius are useful for the purposes of comparison.

This parameter (γ) was estimated according to the following equation:[146]

$$\gamma\,(nm) = \left(\frac{8\eta\times P_{LLP}(m^2Pa^{-1}s^{-1})\times T_M(cm)}{A\,(cm^2)}\right)^{\frac{1}{2}}$$ Equation 2.26

where η is the coefficient of viscosity of water, P_{LLP} is the hydraulic permeability (LLP) of the membrane, A is the effective cross-sectional area of the membrane, and T_M is the membrane thickness.

2.8. Contact angle measurement

The contact angle (θ) of water on the surface of the polymer membrane was measured using an OCA 15 Contact Angle Goniometer (FDS, future digital scientific corp.). Membranes were dried in a vacuum oven and equilibrated in a desiccator prior to the dry measurement. In the case of wet-condition measurements, membranes were immersed in DI (18 MΩ) water for at least three days to reach a fully hydrated state before use. The experiments were performed at ambient temperature based on three replicates for each sample.

Chapter 3.

Effect of free radical-induced degradation on water permeation through PFSA ionomer membranes[1]

3.1. Introduction

3.1.1. Membrane degradation

One of the key challenges facing the commercialization of fuel cells is meeting their industry durability targets. Modern fuel cells require operating in 5000 h for transportation and 30,000 h for stationary applications to achieve their extended service life.[9,147] The failure models of the membranes in fuel cell systems have recently received much attention.[9,148] Chemical and mechanical degradation are the two primary membrane failure models in an operating fuel cell. Membrane mechanical degradation is caused by cyclic for fatigue stresses imposed on the membrane via humidity (see Figure 3.1) and thermal fluctuations in a constrained cell.[9] It is generally accepted that chemical degradation proceeds mechanical degradation.[149] The chemical degradation is triggered by direct attack of radical species generated as by- products or side reactions of the fuel cell electrochemical reactions, even though the precise details are not fully agreed upon.[150-153] Radicals including hydroxyl (HO·), hydroperoxyl (HOO·) and hydrogen (H·) have been detected by *in-situ* and *ex-situ* electron spin resonance (ESR) spectroscopy.[151,154] Fluoride ion emission[155] and loss of proton conductivity, leading to a decrease in performance of the proton exchange membrane fuel cell, are commonly observed.[9] It is also suggested that transition metal ion contaminants, namely iron species, exacerbate free radical formation and accelerate membrane degradation.[156]

[1] Sections of this work have been published in:

International Journal of Hydrogen Energy, Luo, X.; Ghassemzadeh, L.; Holdcroft, S., **2015**, *40*, 16714. Xiaoyan Luo performed all the experimental work and data analysis under the guidance of Professor Steven Holdcroft and Dr. Lida Ghassemzadeh. This work was financially supported by the funding from Automotive Partnership Canada (APC).

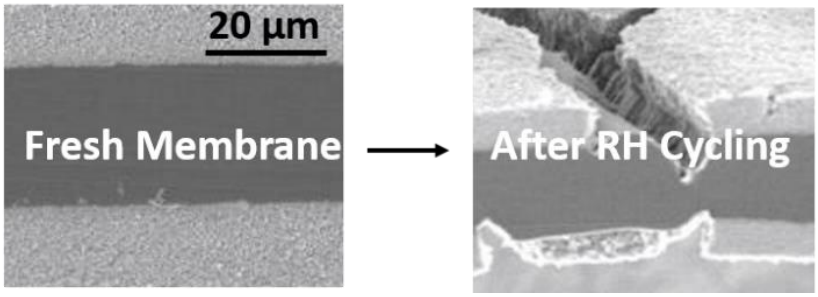

Figure 3.1 Cross section scanning electron microscopy (SEM) of Nafion® 211 after several thousands of relative humidity cycles. (Adapted from ref.[9], Copyright 2012 Elsevier)

The Fenton's reagent reaction is a commonly-used method to generate free radicals for *ex-situ* degradation tests.[147] Free radicals are generated by the following reactions:[151,152]

$$Fe^{2+} + H_2O_2 \rightarrow Fe^{3+} + OH^- + HO\cdot \qquad \text{Equation 3.1}$$

$$HO\cdot + H_2O_2 \rightarrow H_2O + HOO\cdot \qquad \text{Equation 3.2}$$

$$Fe^{3+} + HOO\cdot \rightarrow Fe^{2+} + H^+ + O_2 \qquad \text{Equation 3.3}$$

Healy et al. studied Nafion® membrane degradation by comparing *in-situ* vs. *ex-situ* (Fenton's reagent test) methods.[148] They found that similar fluoro-organic fragments were generated in both methods. Others have monitored chemical and compositional changes of membranes upon exposure to Fenton's reagent using X-ray photoelectron spectroscopy (XPS).[157] Fluoride emission rates were found to increase with the concentration of –COOH polymer termini for the earlier vision of Nafion® membranes.[158] However, new generations of Nafion® membranes have been chemically stabilized, i.e., the concentration of terminal –COOH groups has been decreased to some negligible level.[159,160] A recent NMR study by Ghassemzadeh et al. quantifiably identified structural changes of stabilized Nafion® NR211 membrane, finding fluorine loss, ion exchange capacity loss, and polymer side chain cleavage upon increasing exposure to Fenton's reagent.[153] In addition to Fenton's reagent reaction, other *ex-situ* methods have also used to generate free radicals to study the membrane degradation. These methods include gamma-ray,[161] X-ray radiation,[162] hydrothermal [163,164] and electron beam techniques.[165]

3.1.2. Motivation and approaches of this chapter

To date, *ex-situ* water transport measurements have been exclusively reported for pristine membranes, but it is well documented that membranes degrade during fuel cell operation.[147,166] It is reasonable to assume that water transport properties will change upon membrane degradation. Since the performance of PEMFCs largely depends on the stability of this core component, performance will also be affected.[153,157] Despite the growing body of literature that addresses the molecular processes of membrane degradation, reports on the effect of membrane degradation on water permeation are lacking. Qiao et al. and Hongssirikarn et al. observed a decrease in water uptake and proton conductivity of degraded PFSA ionomer membranes after the treatment in H_2O_2.[167,168] Collette et al. studied water uptake of hydrothermally-aged Nafion® 112, and Nafion® 212.[163,164] Water uptake was found to decrease with increasing aging time. A recent study from our group also found that water uptake of Nafion® NR211 decreased upon exposure to free radicals generated by electron beam irradiation.[165] Recently, Quiroga et al. proposed a new model to investigate the degraded ionomer side chains with the water uptake and the resulting microporous structure during fuel cell operation.[169]

Water transport and membrane degradation are two important factors governing fuel cell performance. However, these two factors have generally been studied separately. In practice, these two factors are closely related. Moreover, to date, water permeation studies have largely been restricted to pristine Nafion® membranes, and relatively few studies have attempted to measure the water uptake of degraded Nafion® membranes. The majority of studies of water uptake of degraded membranes that have been reported are carried out at ambient temperature[167,170,171], but such conditions are not reflective of fuel cell operating conditions (40–100% RH and 60–80 °C). In this chapter, the effect of membrane degradation on water permeation performed at 70 °C using *ex-situ* measurements was examined. Complementary studies including water sorption, ion exchange capacity (IEC), proton conductivity, and scanning electron microscopy (SEM) were also performed on membranes before and after Fenton's reagent reaction. Nafion® NR211 (stabilized) membranes were degraded by exposure to Fenton's reagent at 80 °C. Water vapor sorption of the degraded membrane was performed by using dynamic vapor sorption (DVS) analyzer at 70 °C.

3.2. Experiment

3.2.1. Materials

$FeSO_4 \cdot 7\ H_2O$, NaCl (99%, reagent grade) and 0.01 M NaOH were purchased from Sigma-Aldrich and used as-received. All these chemicals were reagent grade and used as-received. 30 vol% H_2O_2 (Caledon Laboratory Chemicals Ltd.) and 98% sulfuric acid (Anachemia) were diluted to 20 wt% and 1 M, respectively using De-ionized water (DI water,18 MΩ) from Millipore Gradient Milli-Q. Nafion® 211 (NR211) membranes were obtained from Sigma-Aldrich.

3.2.2. Chemical Degradation

Pieces of 10 × 16 cm as-received NR211 membrane were immersed in De-ionized water (DI water,18 MΩ) at 80 °C for at least 5 h to reach full hydration. 10 ppm Fe^{2+} and 20 wt% H_2O_2 were used for preparing Fenton's reagent solutions. This solution (1000 mL) was placed in a beaker, and NR211 membrane was immersed. A schematic diagram of the experimental setup is illustrated in Figure 3.2. A glass frame was used for holding the membrane below the level of the solution. A watch-glass was used to minimize evaporation. Gas pressure was released from the top side of the beaker. Solutions were heated to 80 °C for different times (i.e., 0, 6, 12, 36, and 48 h) in the dark. The Fenton's reagent solution was renewed after specific time intervals. After a set reaction time, the sample was soaked in 1 M H_2SO_4 (to convert the membrane to H^+ form before use) and rinsed with DI water (18 MΩ, from Millipore Gradient Milli-Q) thoroughly to remove the residual free acid.

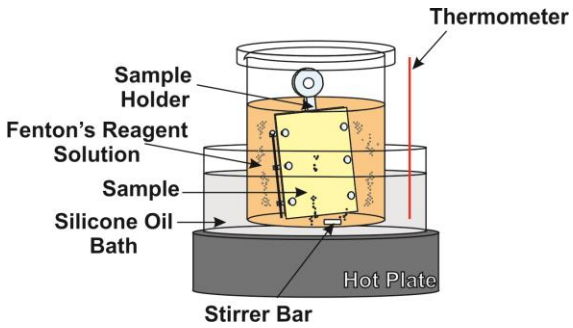

Figure 3.2 Schematic diagram of Fenton's reagent reaction setup.

3.2.3. Scanning electron microscopy (SEM)

Physical changes of the surface of Nafion® NR211 due to exposure to Fenton's reagent were investigated using scanning electron microscopy (SEM-Hitachi DB235) under vacuum. Membranes (H^+ form) were dried in a vacuum oven prior to measurement and cut into rectangles using a stainless-steel doctor blade. To enhance the electron conductivity of membranes, a piece of carbon tape was stick to the sample pan before loading membranes.[172] Measurements were taken at room temperature.

3.2.4. Other experimental techniques

Water sorption, liquid-liquid water permeation (LLP), liquid-vapor water permeation (LVP) and vapor-vapor water permeation (VVP) were performed on pristine and degraded Nafion® NR211 membranes at 70°C, based on three membrane replicates for each experimental method. The detail of experimental procedures can be found in Chapter 2. The following experimental methods were also described in Chapter 2: the calculation of chemical potential, permeability and the resistance of water transport through membranes, effective pore size, the membrane proton conductivity and effective proton mobility.

3.3. Results

3.3.1. Impact of degradation on membrane water permeation

Liquid water and water vapor permeation were investigated by applying a chemical potential on both sides of the membrane using the LVP, LLP and VVP measurement setups described in Chapter 2. The impact of membrane degradation on the liquid-liquid water permeation (LLP) water flux through the membrane is shown in Figure 3.3. In this setup, performed at 70 °C, both sides of the membrane are in direct contact with liquid water. LLP water fluxes for all membranes increase with applied hydraulic pressure, respectively. The permeance for each membrane is obtained from the slope of the plot. As summarized in Figure 3.3, membranes exhibited a permeance of 5.7, 6.8, 7.1, 30.3 and 38.4 × 10^{-12} m Pa^{-1} s^{-1} after exposure to Fenton's reagent for 0, 6, 12, 36 and 48 h, respectively. Water permeability is given by the water permeance normalized to

membrane thickness (see Table 3.1). For the pristine membrane, the measured permeability in this work lies in the same magnitude of previously reported data.[71] The variation between these two data arises from the different membrane pre-treatment procedures. Compared to the pristine membrane, the permeability of the degraded membranes increases with exposure time. Over a period of 48 h Fenton's reagent exposure, the permeability rises to ~ 15 times that of the pristine membrane. Moreover, much less pressure is required to achieve the desired flow rate with increasing exposure.

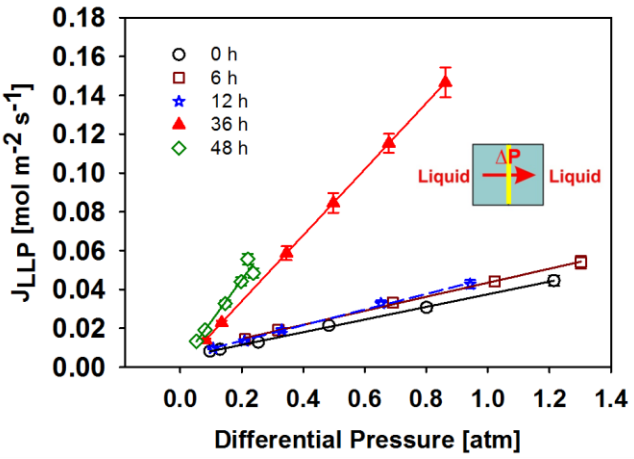

Figure 3.3 **Liquid-liquid water permeation (LLP) flux of degraded NR211 membranes (with Fenton's reagent exposure time of 0, 6, 12, 36 and 48 h) as a function of differential pressure at 70 °C.**

Table 3.1 **Data summary for Liquid-liquid water permeation (LLP) flux of degraded NR211 membranes at 70 °C.**

Fenton's reagent exposure time (h)	Permeance (m Pa^{-1} s^{-1}) × 10^{12}	Thickness (μm)	Permeability (m^2 Pa^{-1} s^{-1}) × 10^{16}
0 (Ref. [71])	8.19	31	2.54
0 (this work)	5.70±0.09	31±1	1.77±0.09
6	6.76±0.12	45±2	3.04±0.19
12	7.12±0.20	65±1	4.63±0.20
36	30.3±0.1	68±3	20.6±0.1
48	38.4±3.2	70±6	26.9±4.7

Figure 3.4 shows the water permeation flux as a function of relative humidity (RH) at 70 °C under the condition that at least one side of the membrane is exposed to water vapor. Water permeation flux is found to decrease with increasing RH for both liquid-vapor water permeation (LVP) and vapor-vapor permeation (VVP) measurements. Regarding the LVP measurement, the membrane exhibits a slightly lower water permeation flux after 6 and 12 h exposure to Fenton's reagent. J_{LVP} after 36 h and 48 h Fenton's reagent test, however, reveals a much higher water flux under high RH conditions (i.e., 60- 90% RH) vs. pristine membranes. VVP water permeation flux as a function of RH is shown in Figure 3.4(b). Compared to the pristine membranes, J_{VVP} of membranes following 6 and 12 h exposure to Fenton's reagent exhibits a slightly lower flux rate; whereas membranes exposed for 36 h and 48 h exhibit higher water fluxes.

The water permeance determined by LVP and VVP experiments are obtained by plotting water flux as a function of differential chemical potential (Figure 3.5). The water permeability was estimated from the permeance normalized to membrane thickness, as shown in Table 3.2. Membranes exhibited a LVP permeability of 1.54, 1.83, 2.64, 3.29 and 2.71×10^{-6} mol^2 m^{-1} s^{-1} kJ^{-1} for the membranes exposed for 0, 6, 12, 36 and 48 h, respectively. For VVP measurements, it is observed that degraded membranes exhibit 17, 35, 60, and 65% higher permeability after exposure for 6, 12, 36 and 48 h, respectively. Compared to VVP permeability data, the LVP permeability is ~ 10 times greater, due to the higher chemical potential in the LVP experiment.

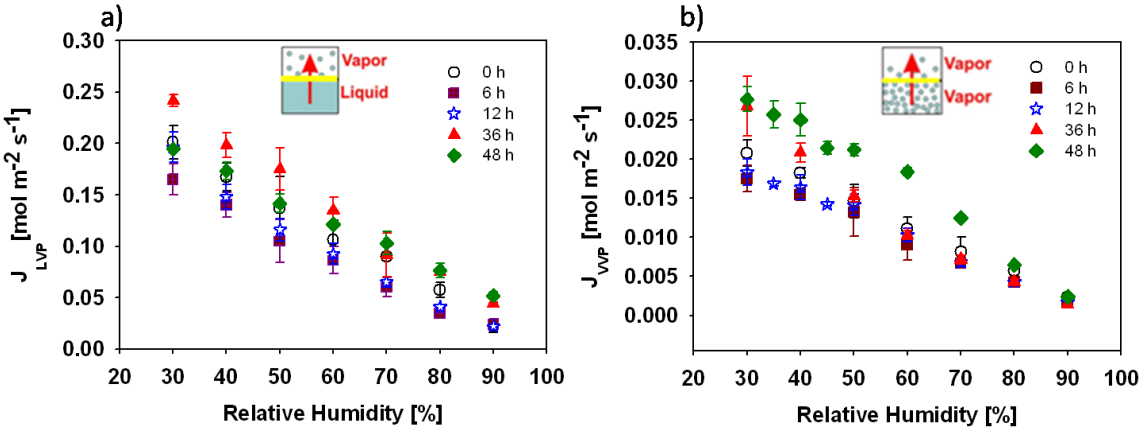

Figure 3.4 Water permeation flux as a function of relative humidity for degraded membranes after Fenton's reagent test for 0, 6, 12, 36 and 48 h at 70 °C. (a) LVP and (b) VVP.

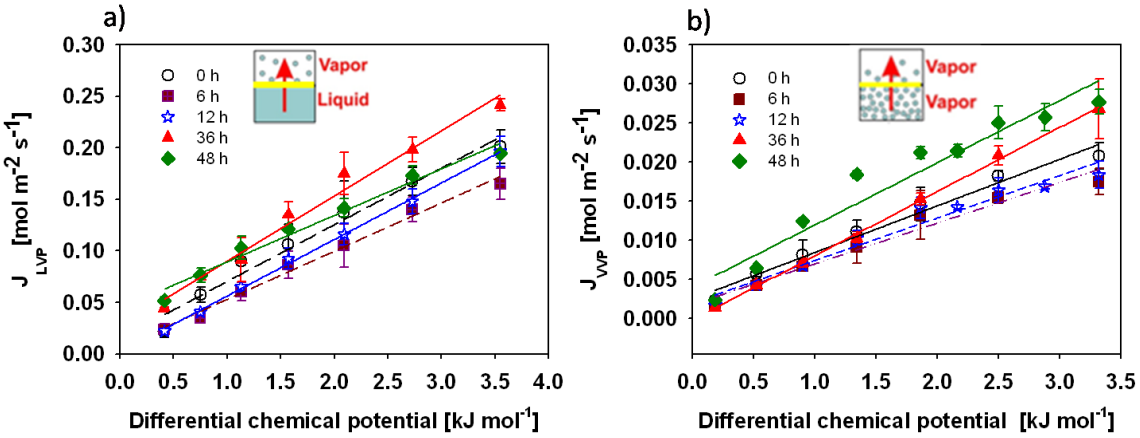

Figure 3.5 **Water permeation flux as a function of differential chemical potential for degraded membranes after Fenton's reagent test for 0, 6, 12, 36 and 48 h at 70 °C. (a) LVP water flux and, (b) VVP water flux.**

Table 3.2 **Data summary of water permeability for membranes with Fenton's reagent exposure time of 0, 6, 12, 36 and 48 h at 70 °C.**

	0 h	6 h	12 h	36 h	48 h
Wet thickness (μm)	28±2	39±2	48±3	52±6	60±8
LVP					
Permeance $\times 10^{2}$ ($mol^2\ m^{-2}\ s^{-1}\ kJ^{-1}$)	5.50±0.39	4.68±0.22	5.49±0.54	6.33±0.38	4.51±0.31
Permeability $\times 10^{6}$ ($mol^2\ m^{-1}\ s^{-1}\ kJ^{-1}$)	1.54±0.22	1.83±0.18	2.64±0.43	3.29±0.57	2.71±0.50
VVP					
Permeance $\times 10^{3}$ ($mol^2\ m^{-2}\ s^{-1}\ kJ^{-1}$)	6.00±0.40	5.20±0.40	5.40±0.40	8.10±0.10	8.00±0.80
Permeability $\times 10^{7}$ ($mol^2\ m^{-1}\ s^{-1}\ kJ^{-1}$)	1.68±0.23	2.03±0.26	2.59±0.35	4.21±0.54	4.80±0.80

3.3.2. Morphology

Scanning electron microscopy (SEM) was performed on the Nafion® NR211 membrane to examine physical changes to the membranes upon exposure to Fenton's reagent. As shown in Figure 3.6, SEM images indicate that significant changes to the membranes. The pristine membrane (i.e., 0 h, Figure 3.6-a) exhibits no large scale

distinguishing features and was translucent in appearance. In contrast, the surface of the degraded samples (12 h & 48 h) was visibly roughened by defects, and the appearance changed from transparent to opaque and milky. Upon closer examination (Figure 3.6), the defects appear to be bubble-like formations (< 50 micrometers diameter) within, and on top of, the membrane. Tears and bumps on the membrane surfaces can be observed, which are consistent with the reports by Hongsirikarn et al.[168] The numbers of defects increased with exposure time.

Images taken at a 45^{o} tilt (Figure 3.7 a-c) also indicate that the degree of degradation increases with increasing exposure time. Moreover, an increase in thickness is observed for the degraded membranes, which is consistent with the physical measurement of the membrane's wet thickness, as reported in Table 3.1.

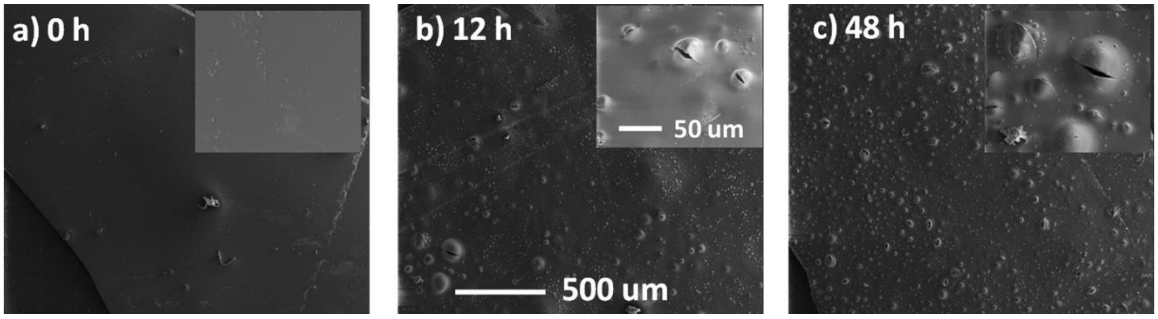

Figure 3.6 Comparison of surface morphologies of the degraded Nafion® NR211 membranes after exposure to Fenton's reagent for (a) 0 h, (b)12 h, and (c) 48 h

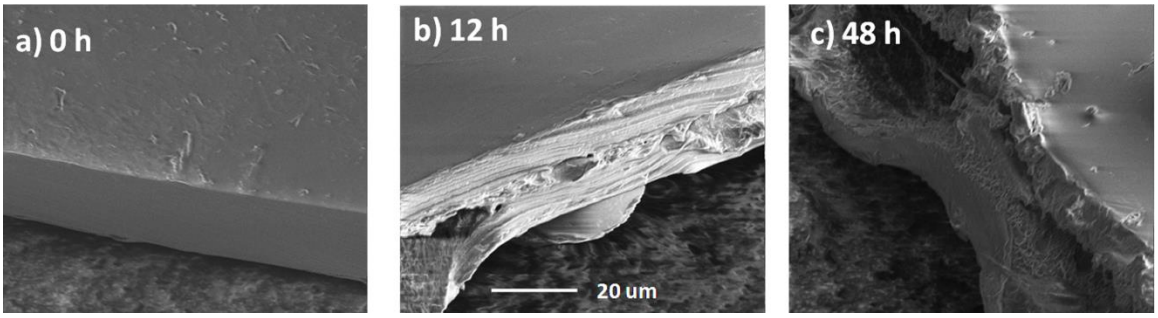

Figure 3.7 SEM images (45˚) of the degraded Nafion® NR211 membrane after exposure to Fenton's reagent for (a) 0 h, (b) 12 h, and (c) 48 h.

3.3.3. IEC, proton conductivity, and effective proton mobility

The degree of membrane degradation as a function of exposure time to Fenton's reagent was also investigated by examining the ion exchange capacity (IEC) (Figure 3.8) and proton conductivity (σ_{H^+})(Figure 3.10). Compared to the pristine Nafion® NR211 membrane, the IEC of degraded membranes decreased from 0.91 mmol g^{-1} to 0.82 mmol g^{-1} over exposure time 0 h to 48 h, suggesting the loss of sulfonic acid functionality. This result is in good agreement with our previous studies which indicate degradation is initiated by the attack on free radicals on the α-OCF_2 side chain of the polymer.[153] The in-plane σ_{H^+}, determined by AC impedance spectroscopy, was performed at 70 °C and 40% RH. As shown in Figure 3.10(b), proton conductivity decreases by 8% over a period of 48 h exposure time. From the measured $\sigma_{H^+}$and calculated values of [-SO_3H] (Table 3.3), the effective proton mobility of the membrane at 40% RH, 70 °C was calculated (Figure 3.10(b)). A slight increase in effective proton mobility (0.148× 10^{-3} to 0.159× 10^{-3} cm^2 s^{-1} V^{-1}) is observed for membranes exposed for 48 h.

Although IEC and $\sigma_{H^+}$are both found to decrease with increasing exposure time, water sorption (Figure 3.9) of degraded membranes exhibit significantly greater values both in terms of water volume fraction (X_v) and water content at room temperature under fully hydrated conditions. Compared to the pristine membrane (0 h), water content and X_v increased by a factor of 2.1 times and 1.6 times, respectively, after 48 h of exposure. Likewise, X_v and λ at 40% RH/70 °C exhibit the same increasing trends, as observed from Figure 3.10(a). The water vapor sorption as a function of relative humidity (RH) under partially hydrated conditions is plotted in Figure 3.11. At 25 °C, degraded membranes possess larger λ values compared to pristine membranes over the entire range of RH studied. Similarly, λ of degraded membranes at 70 °C show an increase with increasing exposure time.

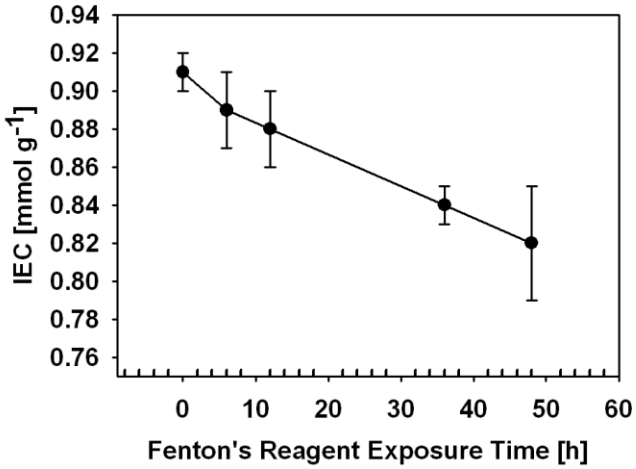

Figure 3.8 **IEC of degraded Nafion® NR211 membrane as a function of exposure to Fenton's reagent.**

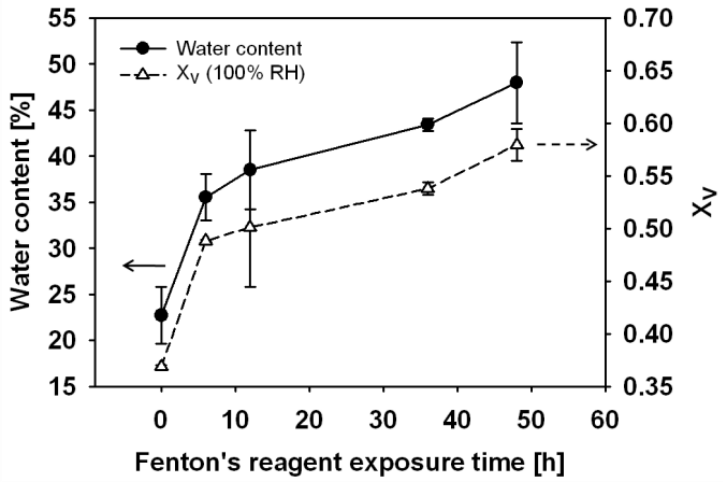

Figure 3.9 **Effect of exposure time to Fenton's reagent on membrane water volume fraction (X_v) and water content (water-saturated membranes, room temperature).**

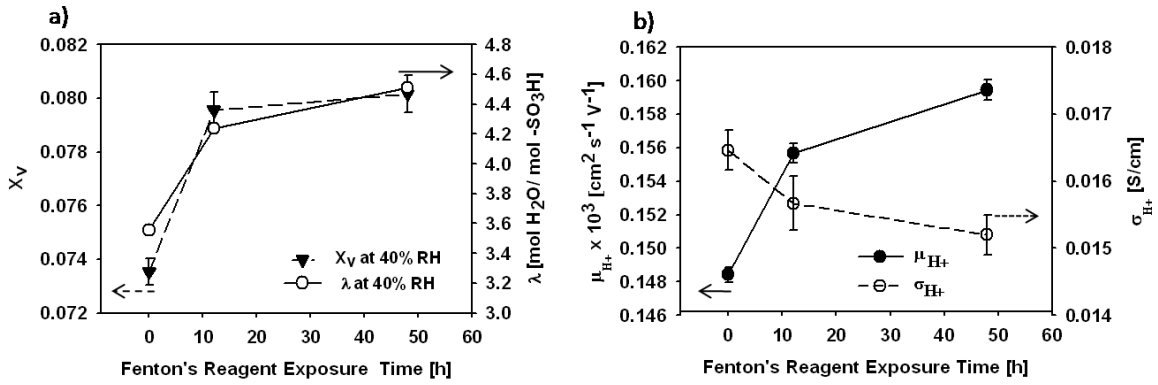

Figure 3.10 **(a) X_v and λ, (b) proton conductivity and effective proton mobility as a function of exposure time at 40% RH, 70 °C.**

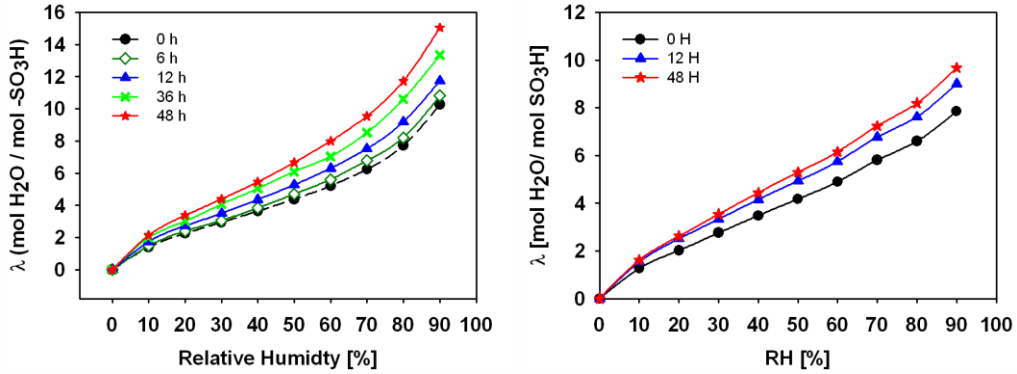

Figure 3.11 **Water sorption isotherm of degraded membranes, (left) at 25 °C; (right) at 70 °C**

Table 3.3 **Analytical sulfonic acid concentration, [-SO_3H], at 70 °C, 40% RH and dry density of membranes.**

Exposure time (h)	[-SO_3H] (M)	Dry density (g cm^{-3})
0	1.15 ± 0.05	1.99 ± 0.09
12	1.04 ± 0.07	1.61 ± 0.15
48	0.99 ± 0.06	1.35 ± 0.25

3.4. Discussion

Our recent published work quantified the structural changes of Nafion® NR211 using solid-state ^{19}F NMR spectroscopy upon Fenton's reagent reaction,[153] demonstrating that the side chain initially degrades. Consequently, ion exchange capacity (IEC) decreases. In this chapter, similar degradation acceleration procedures were used, and it is also found that Nafion® NR211 membranes possess reduced IEC values after being treated with Fenton's reagent. In addition, the membranes exhibit significant modifications in physical structure and transport properties as well.

To date, only a limited number of studies reported the impact of degradation on water content of Nafion® membranes,[163-165,167,168] and all showed lower water content in the degraded membranes. Therefore, it is expected that degraded membranes would possess reduced water permeability given that water permeation coefficient has been reported to decrease with decreasing water content (λ) for pristine Nafion® membranes.[94,173,174] In addition, degraded membranes in the current work also exhibit lower IEC value (i.e., less of hydrophilic sites available) but it is found that water permeability of liquid-liquid (LLP), vapor-vapor (VVP) and liquid-vapor (LVP) permeation all increased after being subjected to degradation. The reason is the increasing hydrophilic volume (X_v) available for water transport. Over 48 h exposure time, degraded membranes possess higher X_v under both partially (~ 1.08 times) and fully hydrated (~ 1.36 times) conditions compared to pristine membranes. Zhao et al.[113] have shown that water permeation in pristine Nafion® increases substantially with hydrophilic volume fraction (X_v). The hydration number (λ) derived from water sorption of degraded membranes were also observed to increase compared to pristine membranes, at both room temperature and 70 °C (Figure 3.11). This is consistent with the results of the study from Collette et al., wherein membranes were degraded by hydrothermal aging.[164] Even though the water content of the degraded membranes decreased with aging time, in that case, the IEC of the membranes also decreased from ~ 0.9 to ~ zero mmol g^{-1} after 450 days of hygrothermal aging. Consequently, λ for their aged membranes increased significantly. The discrepancy in changes of water content between Collette et al.[164] and current study may arise from the different degradation testing procedures (i.e., hydrothermal aging vs. Fenton's reagent). Also, based on the SEM results in the current study, there are large numbers of

bubbles and cracks that appear in the degraded membranes which may be a source of water uptake.

The hydrophilic domains in the membrane form a network through which water flows. It is generally accepted that the pore size of these water channel in the membrane affects the overall water transport.[123] Kreuer studied S-PEEK membranes and found that the membrane possesses narrower and less well-connected hydrophilic channels compared to Nafion®, which results manifests itself in reduced water permeation.[43] The effective pore radius for the membranes were calculated from water transport data. A plot of effective pore radius as a function of exposure time of Fenton's reagent reaction is shown in Figure 3.12. The pore radius of pristine membranes is calculated to be ~ 2.5 nm, which is similar to that reported for Nafion®.[123,175] The effective pore radius increases ~ 6 times upon 48 h exposure to Fenton's reaction time. It is also noted that large bubbles and cracks that appear in the degraded membranes which may be due to the heat and gases released from Fenton's reagent reaction,[176] and which may also lead to expansion of the water channels. This is illustrated, cartoon-fashion in Figure 3.13.

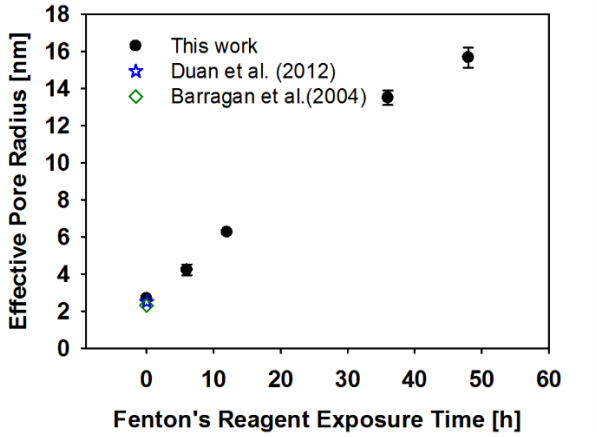

Figure 3.12 Calculated effective pore radius of degraded membranes as a function of exposure time to Fenton's reagent. The data of Duan et al.[123] and Barragán et al.[146] are presented for comparison.

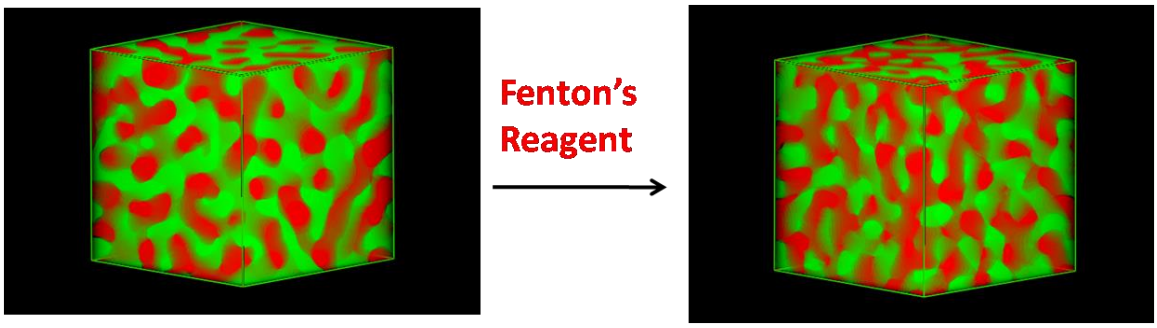

Figure 3.13 Schematic diagram illustrating the change in water channels of a membrane before and after exposure to Fenton's reagent (water channels are shown in red).

The tortuosity (here, refers to the ratio of the water permeability of free space to the permeability of a membrane[177]) and volume fractions of hydrophilic channels are major factors which influence the water transport through membranes[43] but is also a factor that determines proton transport.[144,178] Calculation of the effective proton mobility (μ'_{H^+}) from measured proton conductivity and the analytical proton concentration provides information on the combined influence of the tortuosity of the hydrophilic channels through which protons flow and dissociation of the proton from the pendent sulfonate anion. Both the tortuosity of the channels and proton dissociation are strongly influenced by water content,[34,179] due to water and protons were understood to be transport in the same pathway. Our previous works led to reports of water permeation through short side chain (SSC) PFSA ionomer membrane.[34] It was revealed that pristine SSC membranes possess more tortuous hydrophilic channels that reduces water permeation over long side chain Nafion®. Here, the effective proton mobility of membranes after degradation were found to marginally increase by 7% (after 48 h). It can be attributed to reduced tortuosity of the hydrophilic pathways as a result of the larger water uptake.

3.5. Conclusions

Fenton's reagent was used to degrade Nafion® NR211 membranes at 80 °C. *Ex-situ* water permeation experiments were conducted on membranes before and after exposed to Fenton's reagent. The impact of degradation on water permeation of membranes has been investigated. It is found that the time of exposure of Nafion® NR211

membranes to free radicals via Fenton's reagent has a strong correlation with water transport properties.

Compared to the pristine membrane, degraded membranes exhibit a significant higher permeability of liquid-liquid (LLP), liquid-vapor (LVP) and vapor-vapor water permeation (VVP) after 48 h Fenton's reagent exposure time. Degraded membranes possess lower ion exchange capacity (IEC) and proton conductivity, but a larger hydrophilic volume fraction, effective hydrophilic pore size, and higher proton mobility. The hydration number (λ) increases under partially hydrated conditions at both 25, and 70 °C. SEM analyses reveal significant physical degradation which may contribute to water uptake. Thus, despite a reduction in IEC and proton conductivity, the tortuosity of hydrophilic channels is reduced. Moreover, the higher rates of membrane water permeation revealed by this study should be considered in any consideration of aging of fuel cells that are suspected to involve membrane degradation as it may be a factor that changes the fuel cell performance and optimal parameters of operation.

Chapter 4.

Water transport through short side chain perfluorosulfonic acid (PFSA) ionomer membranes[2]

4.1. Introduction

Membrane thickness plays a role in water transport rates.[13] Significant attention has been paid to reducing the membrane thickness, in order to decrease the ionic resistance and to increase the rate of water transport.[11] It is reported that Nafion® membranes possess an interfacial morphology that is dissimilar to the bulk.[13,85,106] Moreover, Benziger et al.'s[85] study suggested that internal water permeation was the rate limiting factor for permeation at a low water activity (a_w) - when both sides are exposed to water vapor. However, the limiting transport resistance was changed into interfacial mass sorption/desorption at the gas/membrane interface when liquid water was present at one interface (a_w is ~ 1). In contrast, Holdcroft et al[13] and Weber et al[106] found that interfacial transport resistance is much reduced for membranes in contact with liquid.

The operating temperature is an important determining factor in the performance of proton exchange membrane fuel cells (PEMFCs). The increase in the operating temperature is beneficial to the fuel cell performance, as it improves the catalyst behavior at the electrodes, ionic conductivity of the membrane, water management and also gas diffusion rate in a fuel cell.[22,180] With respect to water management, since most water is in the vapor phase at high temperature, it alleviates the liquid water flooding on the electrodes as well as simplifies system water management.[181,182] However, if the temperature is too high, the membrane dehydrates. This will result in reduced proton conductivity and fuel cell performance. For the current PEMFCs, it is suggested that the operating temperature can be up to ~ 130 ˚C.[183]

[2] Sections of this work are modified from the publication:
Journal of Membrane Science, Luo, X. and Holdcroft, S., **2016**, 520, 155.
Xiaoyan Luo performed all the experimental work and data analysis under the supervision of Professor Steven Holdcroft.

Generally, a Nafion® membrane-based PEMFC has a working temperature from 60 ˚C to 80 ˚C. If Nafion® is used under elevated temperature, especially close to the glass transition temperature (T_g, the temperature where the polymer transitions form a hard, "glassy" material to a soft, "rubbery" material) of the polymer, the polymer chains in the membrane rearrange and cause morphological changes in the membrane. Therefore, raising T_g of the polymer is a strategy for developing new proton exchange membranes with improved thermal properties. In this chapter, a shorter side chain Nafion® analogue, so-called SSC PFSA ionomer membrane (the chemical structure is shown in Scheme 1) was examined, which was observed to possess a T_g of 127 ˚C.[183] This temperature is higher than T_g of 100 ˚C for Nafion® membranes (long side chain, LSC), which potentially confers better thermal stability of SSC membranes. In addition, SSC PFSA ionomer membranes possess several other inherent advantages over long side chain (LSC) PFSA analogues (Nafion®), which includes a higher degree of crystallinity and enhanced proton conductivity.[35,184]

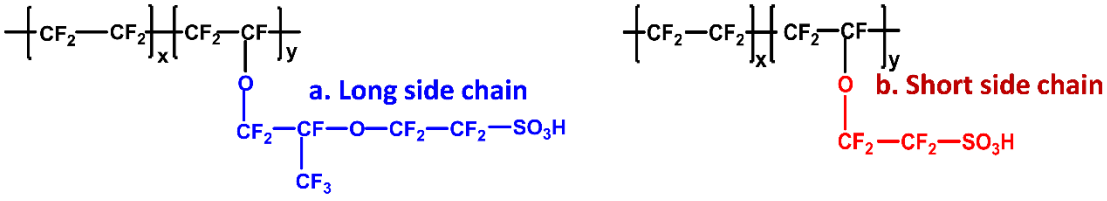

Scheme 4.1 Chemical structure of (a) long side chain- and (b) short side chain-PFSA ionomer membranes.

Based on published literature, SSC PFSA ionomer membranes were reported to possess better fuel cell performance over LSC analogues under elevated temperature and low humidity conditions.[185] However, there are few reports on the water transport properties of SSC PFSA ionomer membranes,[32,184-188] especially under low relative humidity conditions. In addition, due to varied testing methods used by different research groups, there are significant disagreements for the results of water sorption properties of SSC membranes as in comparison to Nafion® membrane. For example, it was found that SSC PFSA membranes exhibited similar water sorption and ionic diffusion properties compared to Nafion® membrane for a given ion exchange capacity.[52,189,190] However, Zawodzinski et al.[81] concluded that the water uptake of SSC membrane is higher than

Nafion® (LSC). Furthermore, De Angelis et al.[186] reported that SSC membranes absorb less water compared to Nafion® for a given RH.

The bulk of the literature on the subject focuses on water sorption in SSC membranes. Studies of water permeation, especially liquid-vapor water permeation (LVP) are rare, yet these conditions are highly pertinent to fuel cell operation.[71] To the best of our knowledge, there is little reported literature discussing water permeation properties of SSC PFSA membranes under low relative humidity conditions, and of interfacial water permeation resistance through SSC PFSA.[186,187] To this end, a systematic study was conducted to examine the effect of experimental temperature and membrane thickness on liquid water and water vapor transport through SSC PFSA ionomer membranes. The examined SSC PFSA ionomer membranes possessed an ion exchange capacity of 1.35 mmol g^{-1}, and the thickness ranging between 24 and 96 μm. Liquid-liquid water permeation (LLP), liquid-vapor (LVP) and vapor-vapor water permeation (VVP) are performed on membranes to study water permeation properties. At least three days equilibration time are allowed before taking permeation measurement for each temperature condition. Internal and interfacial water transport resistances are decoupled from overall resistance to water permeation and compared with that of Nafion® membranes.

4.2. Experiment

4.2.1. Materials

Short side chain (SSC) PFSA ionomer membranes (IEC= 1.35 mmol g^{-1}), provided by Shandong Dongyue Chemical Co. Ltd, were synthesized as previously described,[191] from $CF_2CF(OCF_2CF_2SO_2F)$ monomer. SSC membranes possessed dry thicknesses of 24, 50, and 96 μm, abbreviated as SSC-24, SSC-50, and SSC-96, respectively. Long side chain (LSC, Nafion®) membranes were obtained from Sigma-Aldrich and possessed equivalent weight (EW) = 1100 g mol^{-1} (IEC= 0.91 mmol g^{-1}) and dry thicknesses of 25 (NR211), 54 (NRE212), 131 (NF115) and 181 μm (N117). All membranes were used as-received.

4.2.2. Experimental techniques

Water sorption, liquid-liquid water permeation (LLP), liquid-vapor water permeation (LVP) and vapor-vapor water permeation (VVP) were performed on short side chain PFSA membranes at 25 to 85 °C, based on three membrane replicates for each permeation method. The detail of following experimental techniques can be found in Chapter 2: the calculation of chemical potential, permeability, the resistance of water transport through membranes; the effective hydrophilic pore size, proton conductivity, and effective proton mobility.

4.3. Results and discussion

4.3.1. The effect of membrane thickness on water transport

Liquid-liquid water permeation was determined for liquid-water equilibrated membranes wherein a pressure gradient of liquid water was applied across the permeation cell. Figure 4.1 (a) presents the steady-state liquid-liquid water permeation (LLP) fluxes (J_{LLP})through SSC membranes as a function of hydraulic pressure at 70 °C. LLP water fluxes are all observed to increase with increasing hydraulic pressure, which is consistent with observations with Nafion® membranes.[13,123] A plot of VVP water permeation flux (J_{VVP}) as a function of relative humidity(RH) - 96% RH on one side, variable RH on the other - is shown in Figure 4.1 (b). J_{VVP} increases with decreasing RH, consistent with the increased driving force for water permeation. As decreasing SSC membrane thickness, J_{VVP} slightly increases for the RH between 30 and 50%. For RH from 60 to 90%, similar J_{VVP} values are observed for all membrane thickness. The J_{VVP} data suggest that membrane thickness does not significantly affect water vapor flux through SSC membranes, which is consistent with reports for Nafion® membranes.[84,173]

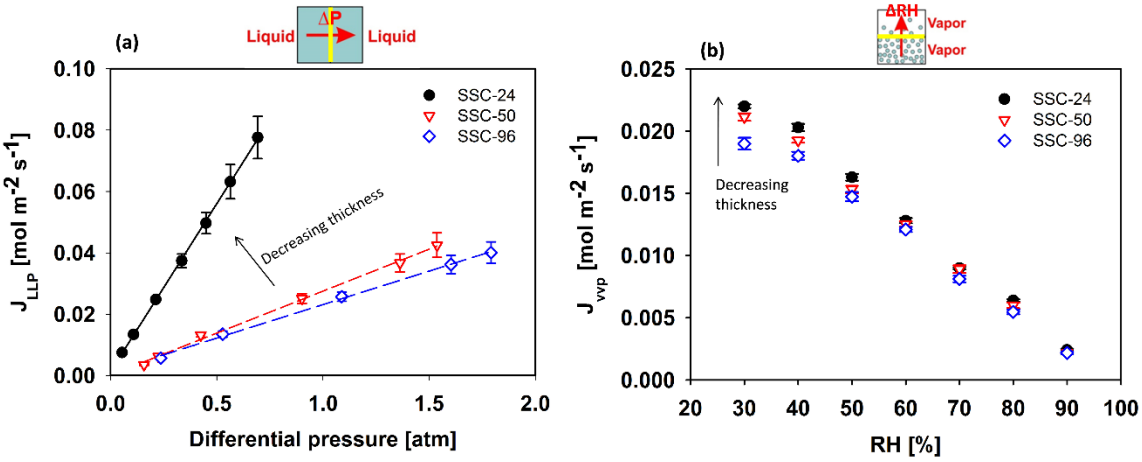

Figure 4.1 Water permeation fluxes of SSC membranes at 70 °C, (a) liquid-liquid water permeation (LLP), and (b) vapor-vapor water permeation.

Water permeance, calculated from the slope of a plot of water permeation as a function of differential chemical potential are shown in Figure 4.2 and summarized in Table 4.1. In the case of LLP, the water permeance of SSC-24 is > 4 times larger than SSC-50 and SSC-96 membranes. In contrast, membrane SSC-24 possesses a VVP permeance (6.4×10^{-3} mol^2 m^{-2} s^{-1} kJ^{-1}) which is similar as compared to SSC-50 and SSC-96 (6.1×10^{-3} and 5.5×10^{-3} mol^2 m^{-2} s^{-1} kJ^{-1}, respectively). The small difference in vapor permeance *vs.* large difference in liquid permeance indicates that the thickness dependence on VVP is weaker as compared to that of LLP permeance, and may be because there is no significant difference in the water volume fraction (X_V) as the membrane thickness is increased from 24 to 96 µm (see Figure 4.3) for partially hydrated conditions. In addition, the VVP permeance is ~ 4 orders of magnitude smaller as compared to LLP, which is consistent with the findings in Nafion®.[83,13,106] The reason for such small VVP permeance can be attributed to a significant larger interfacial water vapor transport resistance ($R_{VVP\_interfacial}$), which will be discussed later.

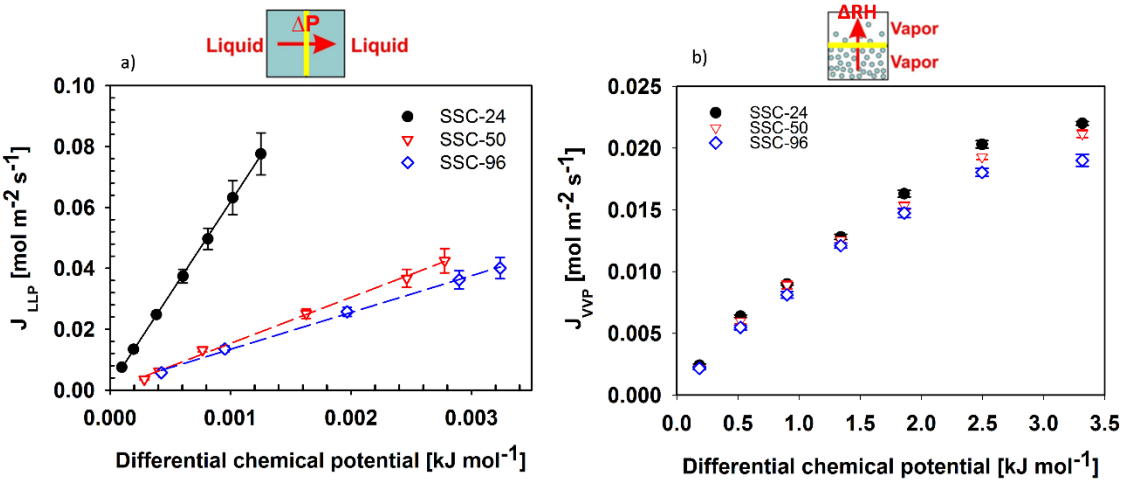

Figure 4.2 **Water permeation fluxes of SSC membranes as a function of differential chemical potential at 70°C for the permeation experiment of a) liquid-liquid, and b) vapor-vapor.**

Table 4.1 **Water permeation data for short side chain PFSA ionomer (SSC) membranes at 70 °C.**

	SSC-24	SSC-50	SSC-96
Wet thickness (μm)	35±3	72±4	115±6
LLP			
Permeance × 10^{-1} (mol^2 m^{-2} s^{-1} kJ^{-1})	6.05±0.05	1.51±0.04	1.21±0.03
VVP			
Permeance × 10^{3} (mol^2 m^{-2} s^{-1} kJ^{-1})	6.40±0.55	6.10±0.59	5.50±0.61

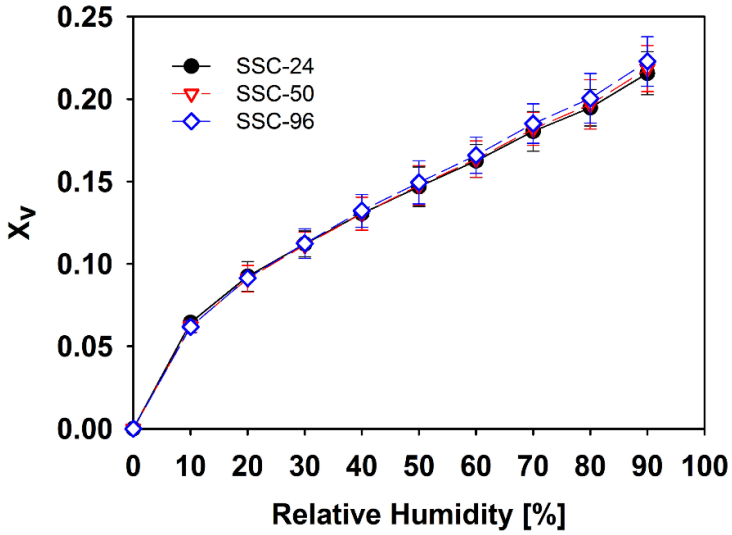

Figure 4.3 Water volume fraction (X_v) of SSC membranes as a function of membrane thickness under partially hydrated conditions.

Water permeation resistances (R, calculated according to Equation 1.7) of liquid-liquid permeation (LLP) and vapor-vapor permeation (VVP) are plotted as a function of membrane thickness in Figure 4.4. R_{LLP} and R_{VVP} both decrease with decreasing membrane thickness. R_{LLP} values of all membranes are below 0.1 kJ m^2 s mol^{-2}, which is several orders of magnitude smaller than that for VVP.

In order to examine the relative importance of the membrane *interfaces* to the membrane permeation to water, $R_{interfacial}$ and $R_{internal}$ are deconvoluted from the overall permeation resistance. $R_{interfacial}$ is calculated from the intercept of the plot of overall resistance as a function of membrane thickness (Figure 4.4) and $R_{internal}$ is estimated by subtracting $R_{interfacial}$ from the overall resistance to water transport (as shown in Equation 1.7). In the case of liquid- liquid water permeation (LLP), $R_{LLP\_interfacial}$ of SSC membranes show a negligible value (< 0.02 kJ m^{-2} s mol^{-2}), which makes a good agreement with Nafion® wherein the small interfacial resistance was attributed to that both of the membrane interfaces were exposed to liquid water.[13,106] Therefore, R_{LLP} is primarily the internal water permeation resistance.

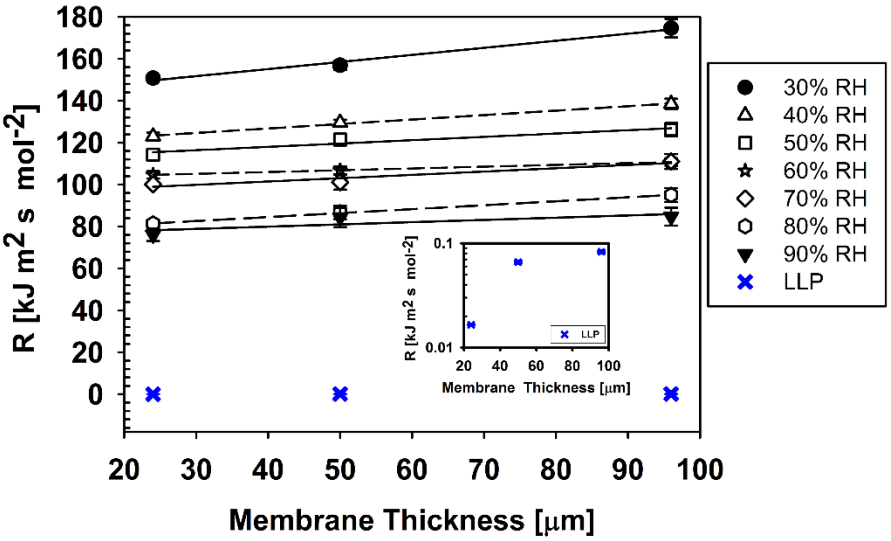

Figure 4.4 Water permeation resistances of liquid-liquid water permeation (LLP) and vapor-vapor water permeation (VVP) (RH ranged from 30 to 90%) through SSC membranes as a function of membrane dry thickness at 70 °C. (Insert plot: water permeation resistance of LLP)

In the case of vapor-vapor water permeation (VVP), however, both membrane surfaces are exposed to water vapor and the overall resistance for VVP (R_{VVP}) consists of two interfacial membrane/vapor permeation resistances ($R_{VVP\_interfacial}$) and an internal water permeation resistance ($R_{VVP\_internal}$). As plotted in Figure 4.5, $R_{VVP\_interfacial}$ decreases as the relative humidity (RH) is increased, which makes good agreement with the findings in Nafion® membranes,[41,132,133] wherein it was attributed to the increase of the fraction of the hydrophilic surface area.

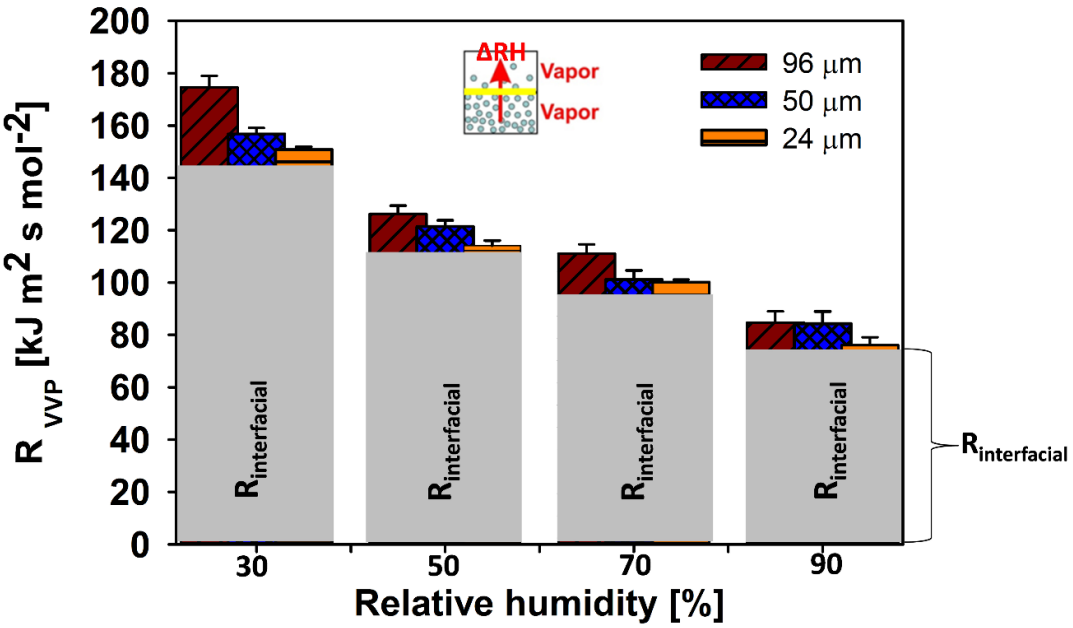

Figure 4.5 **Vapor-vapor (VVP) water permeation resistances of SSC membranes as a function of environmental relative humidity at 70 °C. The gray bars represent interfacial resistance ($R_{interfacial}$) and the colored bars represent internal resistance ($R_{internal}$) of SSC membranes.**

Although it has been shown that, for thin Nafion® membranes, the interfacial resistance is responsible for a significant portion of the overall water transport resistance.[64,84,97,104,113,131] However, for SSC PFSA membranes, $R_{VVP\_interfacial}$ is greater than 80% of the total water permeation resistance (R_{VVP}) for all SSC membranes even for thick membranes (data summarized in Table 4.2). Moreover, the ratio of $R_{interfacial}/R_{VVP}$ increases with decreasing membrane thickness, regardless of relative humidity (RH). A detailed discussion of $R_{interfacial}$ is presented in the following Section.

Table 4.2 The ratio of interfacial water permeation resistance to the total water permeation resistance ($R_{interfacial}/R_{VVP}$) for vapor-vapor water permeation (VVP) at 70 °C, relative humidity (RH) from 30 to 90%.

Membrane Thickness (μm)	30% RH	40% RH	50% RH	60% RH	70% RH	80% RH	90% RH
24	0.94±0.03	0.96±0.04	0.98±0.05	0.96±0.04	0.95±0.02	0.95±0.02	0.99±0.01
50	0.90±0.04	0.91±0.04	0.92±0.05	0.98±0.05	0.94±0.03	0.89±0.03	0.90±0.02
96	0.81±0.05	0.85±0.03	0.88±0.04	0.93±0.04	0.86±0.04	0.81±0.02	0.89±0.01

4.3.2. Interfacial water permeation resistance

Liquid-vapor permeation (LVP) was chosen for more in-depth study since this arrangement is believed responsible for regulating the water balance within an operating membrane electrode assembly according to Adachi et al.'s work.[71] Moreover, the overall LVP resistance (R_{LVP}) consists of only one interfacial membrane/vapor permeation resistance ($R_{LVP\_interfacial}$), which simplifies the study. Steady-state liquid-vapor water permeation (LVP) flux at 70 °C, 40% RH as a function of membrane thickness is shown in Figure 4.6. For both short side chain (SSC) and long side chain (LSC, Nafion®) membranes, LVP water fluxes are observed to decrease with increasing thickness. SSC membranes yield J_{LVP} values of 0.23, 0.22, 0.19 mol m^{-2} s^{-1} for thicknesses of 24, 50 and 96 μm, respectively, which are slightly greater than that of LSC membranes possessing water fluxes of 0.21, 0.19, 0.15 and 0.13 mol m^{-2} s^{-1} for thickness of 25, 54, 131 and 181 μm, respectively.

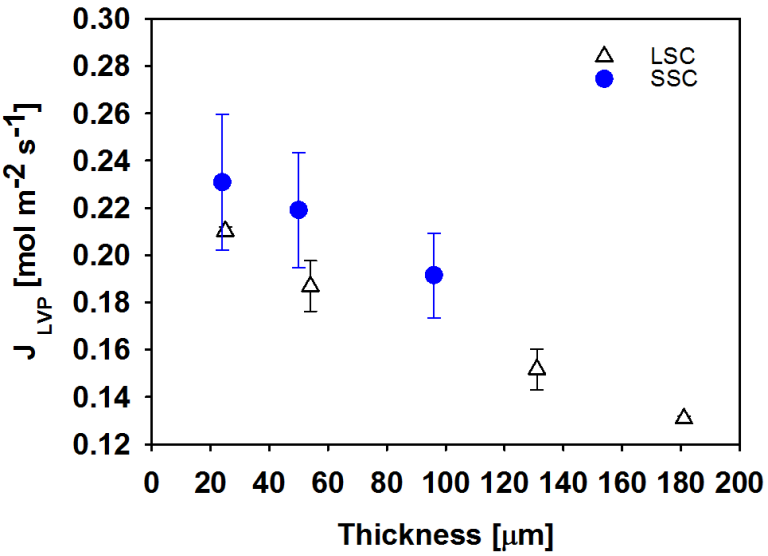

Figure 4.6 **Thickness dependence of liquid-vapor (LVP) water flux of short side chain (SSC) and LSC PFSA ionomer membranes at 70 °C, 40% RH.**

At 70 °C, 40% RH, the chemical potential of water vapor and liquid water are -237.08 kJ mol^{-1} and -240.32 kJ mol^{-1}, respectively, based on our previous reports.[71,86] The difference in chemical potential on both sides of the membrane is calculated to be 2.73 kJ mol^{-1}. Figure 4.7 shows the overall LVP resistance (R_{LVP}) as a function of membrane thickness. R_{LVP} values for SSC membranes are lower than for LSC membranes and decrease with decreasing membrane thickness. In other words, SSC membranes are more permeable than LSC analogues (Nafion®), and thinner membranes are more feasible for high water permeation. The gradient of slope shown in Figure 4.7 for SSC membranes (3.3×10^{-2} kJ m s mol^{-2}) is 35% lower than that of LSC (5.0×10^{-2} kJ m s mol^{-2}), which indicates $R_{LVP\_internal}$ of SSC membranes are significantly lower than for LSC membranes. The reason may be because SSC membranes possess larger wet λ values and significantly greater liquid-liquid water permeability (LLP) values (see Table 4.3) than LSC membranes.

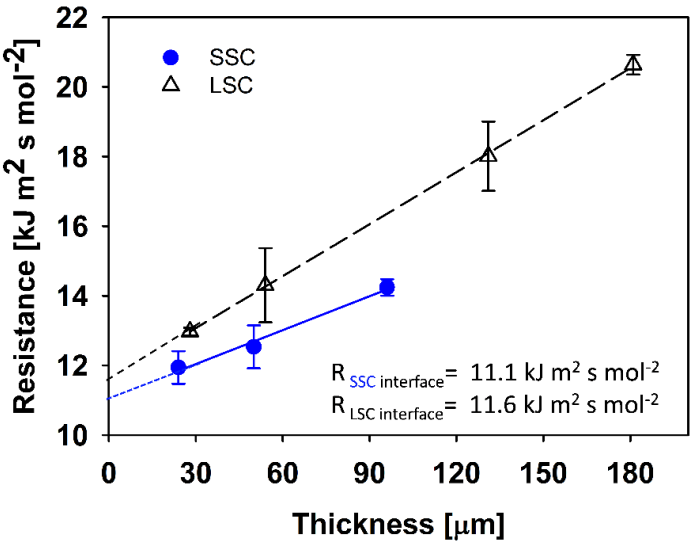

Figure 4.7 **Liquid-vapor water permeation resistance (R_{LVP}) as a function of membrane thickness of SSC and LSC PFSA ionomer membranes at 70 °C, 40% RH. R is calculated using Equation 1.7.**

Table 4.3 **Liquid-liquid water (LLP) permeability of SSC-24 and Nafion® NR 211 membranes at 70 °C.**

Membranes	IEC (mmol/g)	Wet λ at 70 °C (mol H_2O/mol $-SO_3H$)	Wet Thickness (μm)	Permeance (mol² m⁻² s⁻¹ kJ⁻¹) × 10^{-1}	Permeability (mol² m⁻¹ s⁻¹ kJ⁻¹) × 10^{3}
NR211	0.91 ± 0.02	24 ± 2	31±2	2.79±0.05	0.98±0.06
SSC-24	1.35 ± 0.01	34 ± 2	35±3	6.05±0.05	1.88±0.15

The smaller internal water permeation resistance ($R_{LVP\_internal}$) of SSC membranes is also consistent with the larger effective proton mobility (μ'_{H^+}) calculated using Equation 2.25. Calculation of μ'_{H^+} from measured proton conductivities and the analytical proton concentrations provide information on the combined influence of tortuosity of the hydrophilic channels through which protons flow, and the degree of dissociation of the proton from the pendent sulfonate anion; both are strongly influenced by water content.[34,179,192] Proton conductivity (σ_{H^+}) of SSC-24 and NR211 membranes were measured under the same conditions of the LVP experiment (i.e., 70 °C and 40% RH). As shown in Table 4.4, σ_{H^+} of SSC-24 membrane is greater than that of NR211

membrane, and, μ'_{H^+} of SSC-24 is found to be larger than NR211, which correlates well with the trend in internal water permeation resistance (i.e., SSC-24 yields a lower $R_{LVP\_internal}$ value than that of NR211).

Table 4.4 λ, proton conductivity, proton mobility and analytical acid concentration of SSC-24 and NR211 membranes under the condition of 70 °C, 40% RH.

Membranes	λ (mol H_2O/mol $-SO_3H$)	σ_{H^+} (mS/cm)	μ'_{H^+} × 10^3 (cm^2 s^{-1} V^{-1})	[$-SO_3H$] (M)
SSC-24	3.7 ± 0.01	26.2 ± 0.4	0.19 ± 0.01	1.45 ± 0.03
NR211	3.6 ± 0.02	16.9 ± 0.5	0.13 ± 0.01	1.15 ± 0.02

The collective evidence obtained from liquid water sorption, LLP permeability and proton mobility measurements support the conclusion that SSC PFSA membranes possess a lower internal water permeation resistance than LSC membranes. $R_{LVP\_interfacial}$ for SSCs is similar to LSC membranes, suggesting that LVP water permeates through SSC membranes interface and bulk at different rates, which is in good agreement with the observations in the current study of VVP water permeation of SSCs and as well as literature reports of Nafion®.[64,86,97,106] The difference in the rates of internal and interfacial water transport through membranes has been attributed to the different polymer surface reorganization during swelling.[125,193]

Water contact angle measurements were performed on SSC-24 and NR211 (LSC) membranes (shown in Figure 4.8). It was found that water contact angles of dry SSC and LSC membranes are similar (97.6° and 97.2°, respectively), suggesting that both membranes possess a hydrophobic surface, which is consistent with observations of Zawodzinski et al.[194] and Bass et al.[125,127] Other studies have revealed that the interfacial resistance correlates with membrane's water content.[132] As summarized in Table 4.4, SSC membranes possess similar λ values compared to Nafion® membrane at 70 °C, 40% RH.

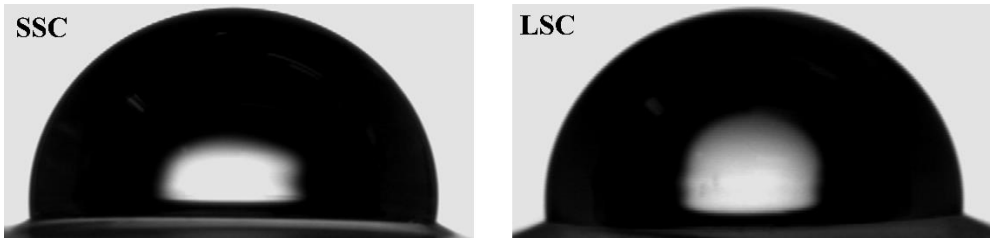

Figure 4.8 Water contact angle of the short side chain (SSC-24) and NR211 membranes, room temperature and 1 atm.

The ionically conductive surface area has been previously observed to have a strong correlation with interfacial mass-transport resistance:[132,195,196] the larger the conductive surface area, the lower interfacial mass-transport resistance is. Compared to Nafion® membranes, SSC membranes possess 33% higher ion exchange capacity (IEC) values (shown in Table 4.3) and 21% greater analytical acid concentration (see Table 4.4), which could reasonably assumed to translate to a higher percentage of active hydrophilic surface area than Nafion® 212.[197] However, since the interfacial water permeation resistance ($R_{LVP\_interfacial}$) for SSC is similar to LSC membranes; this suggests that a larger fraction of hydrophilic sites of SSCs do not necessarily lead to lower $R_{LVP\_interfacial}$ values (or higher water permeation). The discrepancy may well lie in the morphology of the membrane's surface. For example, angle-resolved X-ray photoelectron spectroscopy (XPS) has revealed that SSC membranes possess a less-ordered membrane surface and reduced surface phase segregation.[198]

The ratio of the interfacial water permeation resistance ($R_{LVP\_interfacial}$) to the overall water transport resistance ($R_{LVP\_interfacial}/R_{LVP}$) for SSCs and LSC membranes is calculated to be 0.93, 0.88, and 0.78 for 24, 50 and 96 μm thick SSC membranes and 0.89, 0.81, 0.64 and 0.56 for of 25, 54, 131 and 181 μm thick LSC membranes, respectively, indicating that interfacial resistance plays significant role in controlling the overall water permeation. Also, $R_{LVP\_interfacial}/R_{LVP}$ increases with decreasing membrane thickness, suggesting that the interfacial resistance plays more important role in thinner membranes.

Since water and protons are understood to transport in the same hydrophilic channels,[34,199] useful information can also be extracted from proton conductivity measurements reported in the literature study. For example, Jiang et al.[200] plotted proton

resistance as a function of membrane thickness and found a non-zero intercept when extrapolated to zero thickness, and that the intercept increased with decreasing relative humidity (RH). They attributed the non-zero intercept to the contact resistance. Also, Cheah et al. studied the effect of interfacial water transport resistance on coupled proton and water transport across Nafion® membrane. They found that the interfacial water transport at the membrane/vapor interface controls both the proton and water transport across the membrane.[201]

It is suggested that Nafion® membranes possess a hydrophobic surface skin layer with a thickness of ~ 1-10 nm.[127,129,193,194,202] Weber et al. using X-ray microtomography to examine the water distribution within a Nafion®117 membrane (175 µm thick), report the thickness of a dehydrated membrane layer to be ~ 17 µm under liquid/dry conditions.[203] In addition, Thomas et al. report a sharp decrease of water content when a membrane is exposed to water vapor side, reporting the thickness of dehydration layer to be ~ 40 µm thick.[204] Therefore, it is reasonable to suggest the cause of the interfacial resistance layer is a dehydration region where the membrane is exposed to vapor. A schematic illustration of water profile across exposed to liquid on one side and vapor on the other is shown in Figure 4.9.

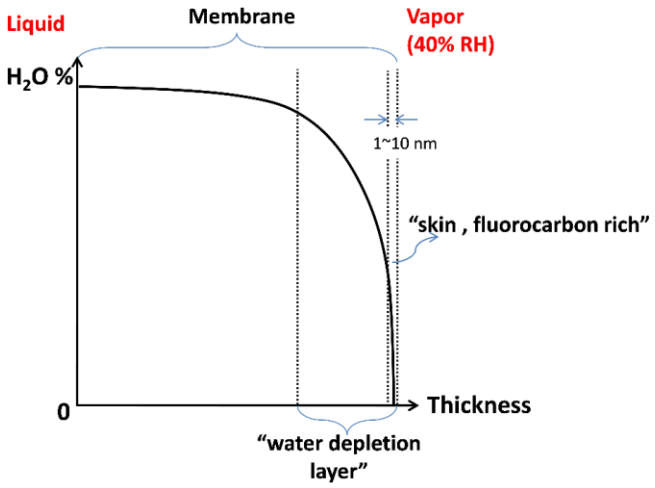

Figure 4.9 Water profile through a membrane exposed to liquid on one side and vapor on the other.

4.3.3. The impact of temperature on water transport

Figure 4.10 (a) displays the water sorption of SSC-24 membrane (i.e., short side chain PFSA membrane with a dry thickness of 24 μm) under fully hydrated conditions. The increase in λ with temperature is consistent with the reports of Jalali et al.,[27] which was attributed to the relaxation of the polymeric matrix with increasing temperature. When reducing the experimental hydration condition to partially hydrated (Figure 4.10 b), SSC-24 membrane absorbs slightly more water at higher temperature, which is consistent with the previous reports, wherein the actual water content in the membrane was found to be only slightly affected by the temperature at fixed water activity.[52,186,205]

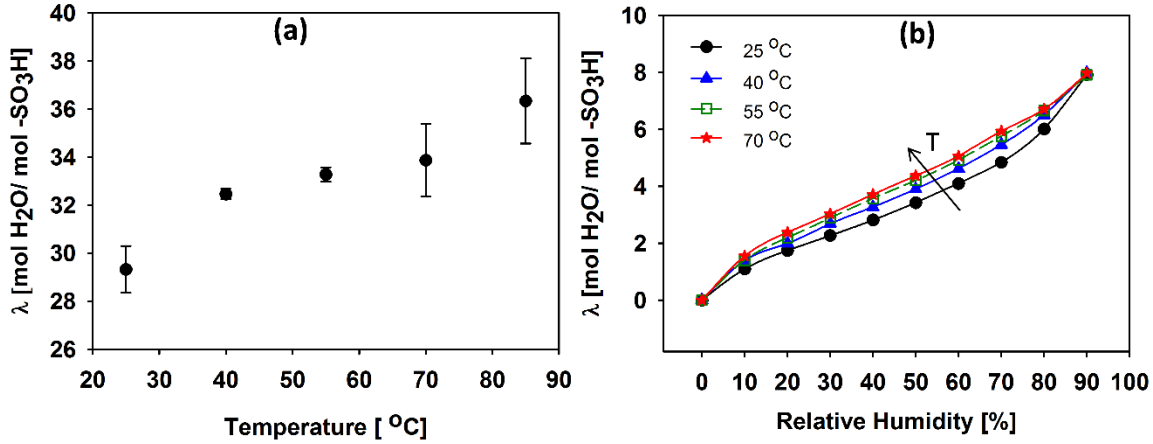

Figure 4.10 Temperature dependence on water sorption of SSC-24 membrane of (a) fully hydrated and (b) controlled RH.

The plot of the effect of temperature on water permeation of SSC-24 membrane is shown in Figure 4.11 and 4.12. For each specific studied temperature condition, the liquid-liquid water permeation flux (J_{LLP}) increases linearly with increasing applied hydraulic pressure (see Figure 4.11 (a)). As shown in Table 4.5, the LLP permeance of SSC-24 (the slope of the plots in Figure 4.12 a) is 25.4, 30.3, 38.9, 60.5 and 71.7 $mol^2\ m^{-2}\ s^{-1}\ kJ^{-1}$ for 25 °C, 40 °C, 55 °C, 70 °C and 85 °C, respectively. Compared to the permeance at 25 °C, the SSC-24 membrane possesses twice as great a permeance at 85 °C, which is in good agreement with Duan et al.'s results for Nafion® 115 membrane.[123] Their value for Nafion® 115 at 80 °C is ~ 2 times as compared to 23 °C, and they attributed this increase to a lower water viscosity and increased water volume fraction (X_v) at high temperature. In addition, Zhao et al. suggests that water permeation in Nafion® membrane increases

substantially with hydrophilic volume fraction (X_v).[113] Similarly, as shown in Figure 4.13(a), X_v changes by ~ 6% when increasing the temperature from 25 °C to 85 °C. However, in comparison to the changes in permeance values (~ 65%) at the same temperature, the increase in X_v is not as significant. The effective pore radius of the hydrophilic channels in the membrane generally correlates with the rates of water transport,[43,123] and is shown in Figure 4.14. As X_v increases, the calculated effective pore radius increases by 1.5× for an increase in temperature from 25 to 85 °C. This is consistent with Gierke et al. findings where the water channel dimensions increased linearly with the water volume fraction.[44]

The further experimental investigation has been carried out to elucidate the effect of relative humidity (RH) on membrane water permeation (Figure 4.11 b and c), where membranes have been equilibrated for at least 3 days before taking measurements at each temperature condition. As can be seen, vapor-vapor (VVP) and liquid-vapor(LVP) water permeation fluxes (J_{VVP} and J_{LVP}) increase significantly but nonmonotonically with increasing temperature, consistent with the report for Nafion® in ref.[206]. For example, at 90% RH, J_{VVP} through SSC-24 at 85 °C is ~ 3 times larger than J_{VVP} at 25 °C. At 30% RH, J_{VVP} at 85 °C is ~ 20 times larger than J_{VVP} of 25 °C. As summarized in Table 4.5, the permeance of VVP and LVP increases by ~94% and 92%, respectively, as temperature increased from 25 to 85 °C. However, the permeance first increasing with increasing temperature up to 70 °C and then decreasing with increasing temperature. X_v, under partially hydrated conditions, shown in Figure 4.13(b), is found to be greater at a higher temperature (> 25 °C), which may result in greater water sorption/permeation in SSC membranes at a higher temperature.

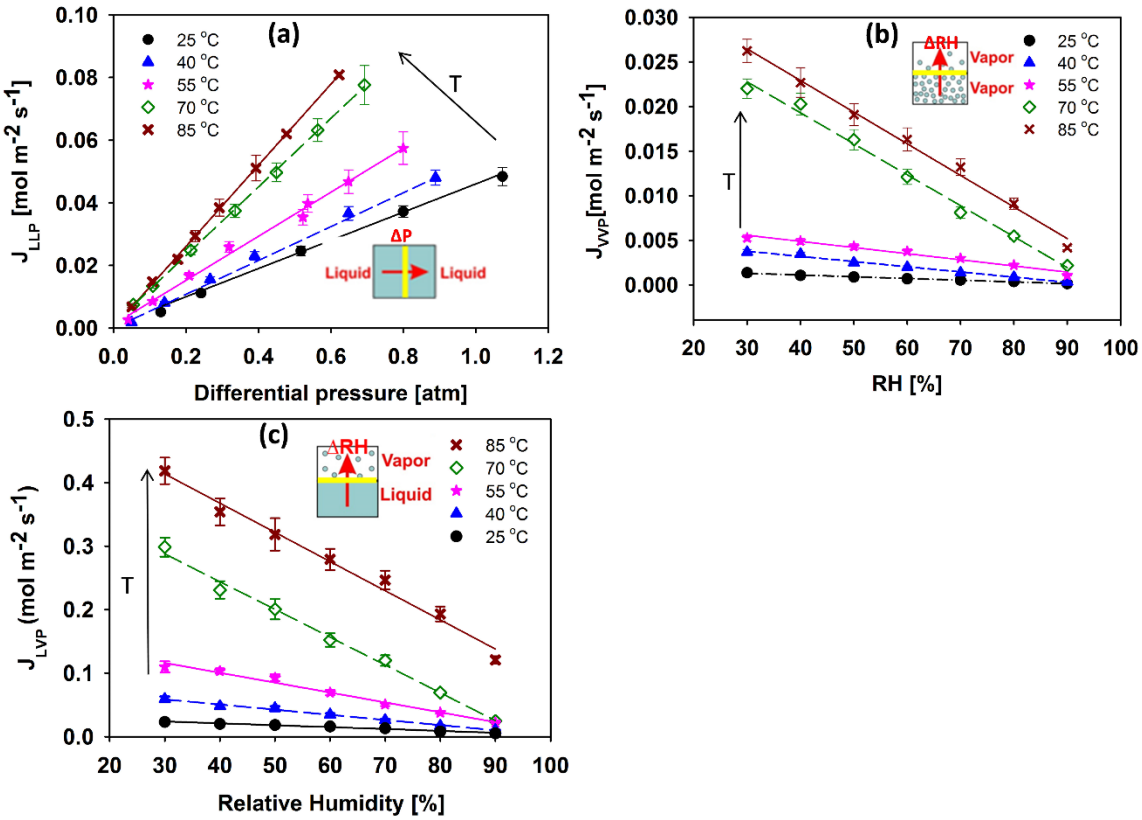

Figure 4.11 **Temperature dependence on water permeation fluxes of SSC-24 membrane as a function of (a) hydraulic pressure (∆P) of liquid-liquid water permeation, (b) relative humidity of vapor-vapor water permeation (VVP), and (c) relative humidity of liquid-vapor water permeation (LVP)**

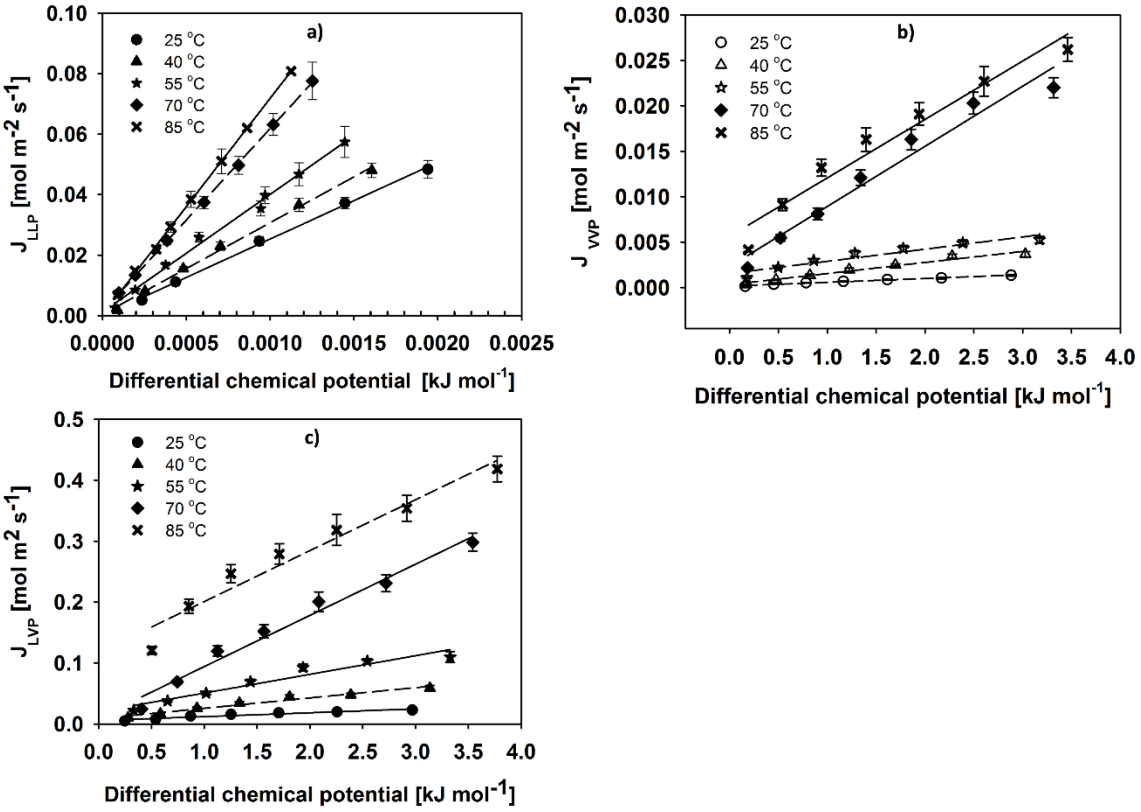

Figure 4.12 The temperature dependence of water flux of SSC-24 membrane as a function of differential chemical potential, a) LLP, b) VVP and c) LVP.

Table 4.5 Permeance of water through SSC-24 membrane for experiments of LLP, LVP, and VVP at the temperature ranged from 25 to 85 °C.

	25 °C	40 °C	55 °C	70 °C	85 °C
Permeance_LLP × 10^{-1} (mol^2 m^{-2} s^{-1} kJ^{-1})	2.54±0.01	3.03±0.01	3.89±0.01	6.05±0.05	7.17±0.07
Permeance_LVP × 10^{2} (mol^2 m^{-2} s^{-1} kJ^{-1})	0.64±0.08	1.69±0.14	3.06±0.36	8.39±0.55	8.36±0.84
Permeance_VVP × 10^{3} (mol^2 m^{-2} s^{-1} kJ^{-1})	0.40±0.02	1.20±0.09	1.30±0.20	6.60±0.60	6.40±0.60

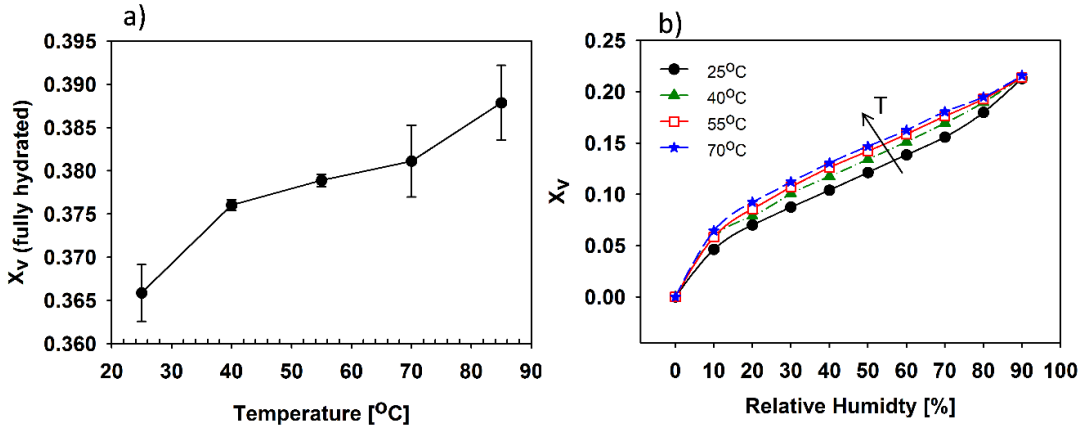

Figure 4.13 **Membrane water volume fraction (X_v), (a) as a function of experimental temperature under fully hydrated conditions, and (b) as a function of relative humidity (RH), i.e., partially hydrated conditions.**

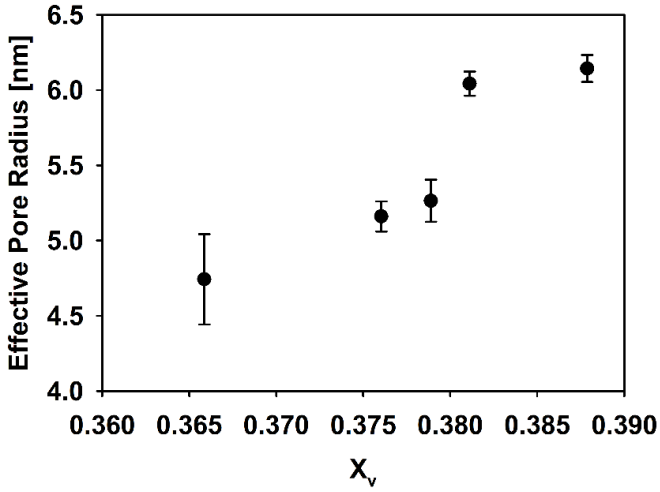

Figure 4.14 **Effective pore radius of SSC-24 membrane (based on LLP permeability data calculated from Table 4.5) as a function of X_v at specific temperature of fully hydrated condition (the temperature ranged from 25 to 85 °C).**

In comparison to liquid-liquid water permeation (LLP), the permeance of vapor-vapor (VVP) and liquid-vapor (LVP) is 3 and 4 orders of magnitude smaller, respectively, which can be ascribed to the effect of membrane interfacial resistance as discussed in Section 4.3.2. Permeance was also reported as an effective permeation coefficient (k_{eff}) in previous literature.[80] Figure 4.15 displays the $\mathrm{Ln}\, k_{eff}$ as a function of temperature for water permeation of LLP, LVP, and VVP. $\mathrm{Ln}\, k_{eff}$ increases with increasing temperature

for LLP, LVP and VVP experiments. A fit of this plot with an Arrhenius function form k_{eff} = k° exp(-E/RT) yields activation energy (E) for water permeation through SSC membranes. LLP for SSC membranes provides E_{LLP} equal to 16.3 kJ mol^{-1}, which is slightly smaller than the E_{LLP} of 16.7 kJ mol^{-1} calculated from the molecular dynamics simulations of Nafion®.[207,208] For the case of VVP and LVP, the activation energy (E_{VVP} and E_{LVP}) are estimated to be 43.1 and 40.2 kJ mol^{-1}, respectively, which is slightly smaller to NR211 under vapor/dry conditions (E= 44.4 kJ mol^{-1}).[80] In comparison to E_{LLP}, the activation energy of VVP and LVP is ~ 2.5 times greater, which correlates well with SSC membranes possessing lower VVP and LVP permeation rates than that measured for LLP. In addition, the results of lower permeation rate in vapor than in liquid, are in good agreement with that of Nafion® membranes,[97,125,126] which was attributed to reduced degree of tortuosity of water channel in the membrane when exposed to liquid water[113] and due to changes in the microstructure of the membrane.[125,127]

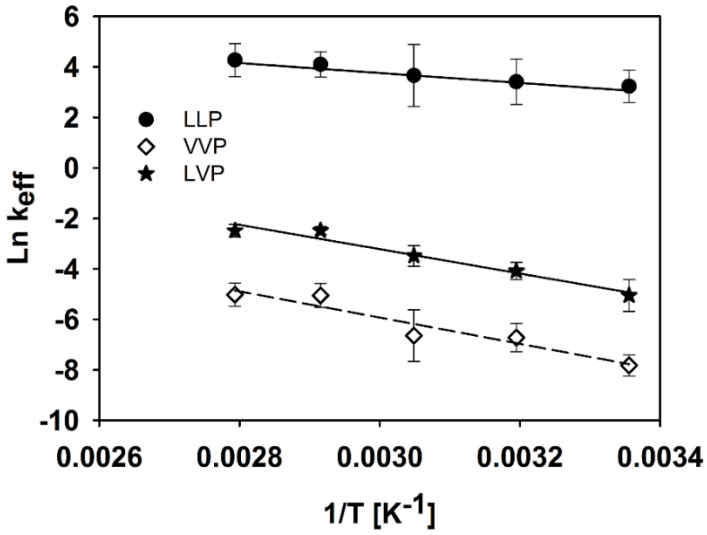

Figure 4.15 Arrhenius plot of the effective water permeation coefficients, k_{eff} (mol^2 m^{-2} s^{-1} kJ^{-1}) of LLP, LVP, and VVP for the SSC-24 membrane, where k_{eff} are taken from permeance at a specific temperature at Table 4.5.

4.4. Conclusions

The impact of thickness (24- 96 μm) and temperature (25- 85 °C) on water transport of short side chain (SSC) perfluorosulfonic acid (PFSA) ionomer membranes

were investigated using water sorption and permeation methods. Increasing the membrane thickness from 24 to 96 μm results in modest increases vapor-vapor (VVP) water permeance compared to liquid-liquid (LLP) water permeance, which can be explained by the significant larger interfacial resistance in VVP. The resistances of liquid-vapor water permeation (LVP) and VVP indicate that the interfacial permeation resistance is responsible for a large percentage of the total water transport, even for thick SSC membranes. In light of the interfacial resistance study, as well as other reports,[203,204] it is speculated that the interfacial layer of the membrane is the result of depletion layer due to membrane dehydration. Compared to long side chain (LSC, i.e., Nafion®), SSC membranes possess lower internal permeation resistance. However, the interfacial resistance of SSCs and LSCs is observed to be similar, despite the fact that the SSC membranes possessed a larger ion exchange capacity (IEC) and larger water content. This could be as a consequence of a poorly-connected surface membrane morphology in SSCs, which suggests that surface morphology is a limiting factor in the overall membrane water permeation.

Temperature is found to have a profound impact on water transport through SSC membranes. Under fully and partially hydrated conditions, the water transport rate increases with temperature. The activation energy of liquid-liquid (LLP), liquid-vapor (LVP) and vapor-vapor (VVP) water permeation of SSCs were calculated to be 16.3, 40.2 and 43.1 kJ mol^{-1}, respectively, which is slightly smaller value than that of Nafion® membranes. In addition, the activation energy of water permeation in SSC membranes correlates well with water permeation resistance that is observed to increase in the order of LLP < LVP < VVP. The data set and analyses provide insight into understanding the role of membrane thickness and temperature on water transport properties, and it may be implemented into any strategy aiming at utilizing thinner membranes and higher temperature operation in proton exchange membrane fuel cell applications.

Chapter 5.

Water permeation through anion exchange membranes[3]

5.1. Introduction

5.1.1. Alkaline fuel cells

Although proton exchange membrane fuel cells (PEMFCs) are regarded as good power conversion devices due to their low emissions and high efficiency,[75,159,209] the high cost of the PEMFCs system prevents their large-scale commercialization. The costliest parts in PEMFCs are the proton exchange membrane and the catalyst (i.e., platinum). Therefore, developing platinum-free fuel cells is necessary for the widespread application. Unfortunately, platinum-free catalysts generally do not work well under an acidic condition of PEMFCs.[6,38,39] One alternative is to run fuel cells in an alkaline environment. Under alkaline conditions, some transition metals and their oxides can serve as a stable catalyst for fuel cell reactions.[210]

Alkaline fuel cells were first developed in the 1930s by Francis Thomas Bacon.[211] They represent one of the oldest fuel cell types, which have been developed 30 years earlier than proton exchange membrane fuel cells. Early alkaline fuel cells were built with liquid electrolytes (e.g., an aqueous solution of KOH) and operated with hydrogen as the fuel at a temperature between 50 and 200 ˚C. NASA used such fuel cells in the 1960s as a power source for the Apollo space missions.[211] This technology, however, was abandoned mainly due to liquid (aqueous) electrolytes poisoning by carbon dioxide. The KOH solution is very sensitive to the presence of carbon dioxide. When air is used instead

[3] Part of work in this Section has been published in:

Journal of Power Sources, Luo, X. Wright, A., Weissbach, T. and Holdcroft, S.
Dr. Andrew Wright synthesized all the HMT-PMBI polymers, Mr. Thomas Weissbach cast all the HMT-PMBI membranes and Mr. Benjamin Britton spray-coated HMT-PMBI membranes with catalyst ink. Xiaoyan Luo performed the rest of experimental work and all the data analysis in this chapter.

of oxygen, the hydroxyl ions react with CO_2 contained in air and form K_2CO_3 precipitates, according to the following reaction:

$$2OH^- + CO_2 \rightarrow CO_3^{2-} + H_2O \qquad \text{Equation 5.1}$$

And/or

$$2\,KOH + CO_2 \rightarrow K_2CO_3 + H_2O \qquad \text{Equation 5.2}$$

The formation of these carbonate precipitates causes significantly decreased cell performance. First of all, the reaction shown above decreases the number of hydroxyl ions available for reaction at the electrodes, which in turn eventually reduces the conductivity of the electrolyte. As a result, highly pure hydrogen and oxygen must be used as the fuel and oxidant feeds which significantly increases the system cost. On the other hand, as the mobile nature of K^+ ions in the liquid electrolyte, these formed insoluble species (e.g., carbonate precipitates) may block the transport pathways of gas reactants and cause corrosion. Moreover, liquid electrolyte also causes leakage and flooding problems, which increases the system manufacturing and managing cost.[212] Due to the above disadvantages of using liquid electrolyte in the alkaline fuel cells, a solid polymer electrolyte was introduced to replace the liquid electrolyte.[213] Since then, research on alkaline fuel cell moved to polymeric anion exchange membranes as the hydroxide transport medium, and anion exchange membrane fuel cells (AEMFCs) is garnering renewed attention.

5.1.2. Anion exchange membrane fuel cells

For traditional AEMFCs using hydrogen fuel and air/oxygen as the oxidant, the cell reactions are akin to proton exchange membrane fuel cells (PEMFCs), both of which are based on hydrogen oxidized at the anode and oxygen reduced at the cathode. As illustrated in Figure 5.1, in an operating anion exchange membrane fuel cell, hydrogen and OH^- are oxidized to produce water and electrons at the anode:

$$H_2 + 2OH^- \rightarrow 2\,H_2O + 2\,e^- \qquad \text{Equation 5.3}$$

At the cathode side, OH^- is formed and transported through anion exchange membrane to the anode:

$$\frac{1}{2}\,O_2 + H_2O + 2e^- \rightarrow 2\,OH^-$$ Equation 5.4

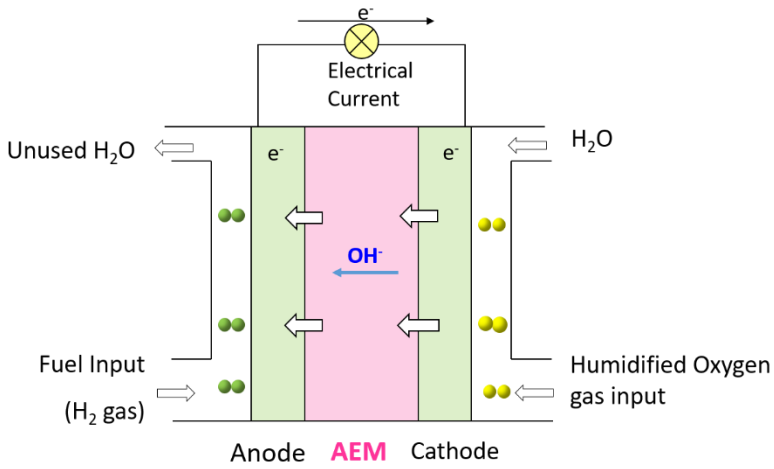

Figure 5.1 Schematic diagram of an operating anion exchange membrane fuel cell.

The overall cell reaction of AMEFCs is the same to the PEMFCs:

$$H_2 + \frac{1}{2}\,O_2 \rightarrow H_2O$$ Equation 5.5

However, there are also some differences between these two types of fuel cells:[214]

(a) Water is generated at the anode side in AEMFCs, while it is generated at the cathode side in PEMFCs.

(b) Compared to PEMFCs, water is a reactant in AEMFCs as it is consumed in the cathode reaction.

Although non-precious metal catalyst can be used in AEMFCs, there are still challenges in the commercialization of them. Currently, a significant challenge in AEMFCs technology lies in the anion exchange membranes (AEMs).[215] The AEMs require to exhibit chemical stability to highly basic conditions, possess high ion conductivity to minimize Ohmic losses[1] and demonstrate adequate water transport in order to offset critical issues of water management.

5.1.3. Anion exchange membranes

Anion exchange membranes (AEMs) conduct anions such as OH^- and Cl^-, as they contain positively (cationic) charged groups bound covalently to polymer backbones. These positively charged functional groups usually involving N-based groups, including quaternary ammoniums[216-218] and polybenzimidazole (PBI) systems where the cationic groups are on the backbone.[139,219,220] Other functional groups have been reported as well.[221-223] These functional groups can be bound to backbone either directly or indirectly (i.e., via extended side chains); or they can even be an integral part of the backbone.[214]

AEMs have drawn large attention in the last two decades.[1,215] To date, there is no such now-commonly used anion exchange membrane as compared to Nafion®, which may be due to the early stage of material development. A linear, quaternary ammonium group based anion exchange membrane, FAA3 supplied by FuMa-Tech, is commercially available. However, the detailed chemical structure of this polymer is not revealed so far. The reported hydroxide conductivity of AEMs is generally lower than proton conductivity of Nafion® (~ 100 mS cm^{-1}). Depending on the polymer structure and operation conditions, the hydroxide conductivity usually ranges from 1 to 70 mS cm^{-1}.[1,215]

One of the challenges in the operating anion exchange membrane (AEM) is the mitigation of the effects of CO_2 when exposed to air. Even for very short periods of exposure time to air, membrane ionic conductivity drops significantly. This is due to the OH^- ions in the membranes quickly convert to the less conductive CO_3^{2-} and even less conductive HCO_3^- form (see Equations 5.6 and 5.7). For example, the change in the conductivity of an AEM upon exposure to CO_2 is shown in Figure 5.2, 82% of its ionic conductivity was lost after exposure to the atmosphere after 3 h.

$$OH^- + CO_2 \leftrightharpoons HCO_3^- \qquad \text{Equation 5.6}$$

$$OH^- + HCO_3^- \leftrightharpoons CO_3^{2-} + H_2O \qquad \text{Equation 5.7}$$

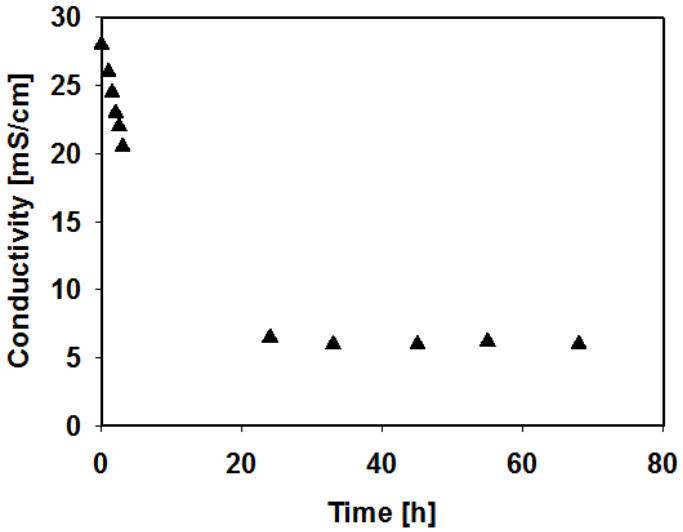

Figure 5.2 Decline in conductivity of a hydroxide form an ion exchange membrane during conductivity measurement. (the conductivities were measured with samples immersed in liquid water at 30 °C. Data are from ref.[223], Copyright 2012 American Chemical Society)

Anion exchange membranes (AEMs) require water to facilitate ion transport. In addition, water is a reactant for the electrochemical reactions. However, if an excessive amount of liquid water is present on the electrodes, the reaction sites could be blocked and lead to significant fuel cell performance losses. Similar to proton exchange membrane fuel cells (PEMFCs), as shown in Figure 5.3, finding a subtle equilibrium between membrane dehydration and liquid water flooding is critical in guaranteeing the high performance of anion exchange membrane fuel cells (AEMFCs). Back water permeation from the anode to the cathode may be able to regulate the imbalance of water within operating fuel cells.[71] Therefore, research on back water permeation is of particular interest for the application of AEMFCs.[100,224]

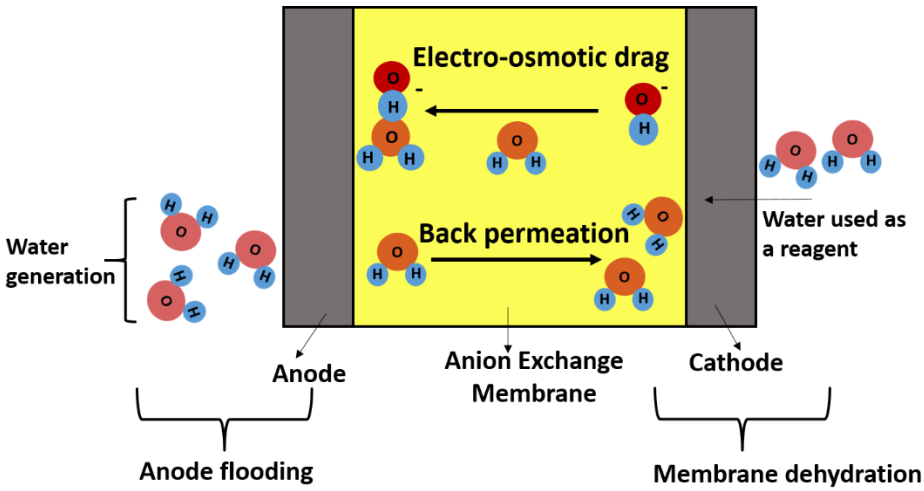

Figure 5.3 Schematic diagram of water transport in an operating anion exchange membrane fuel cell.

5.1.3.1. Morphology of anion exchange membranes

The morphology of anion exchange membranes (AEMs) has not been extensively explored, compared to that of proton exchange membranes, such as Nafion®. Few attempts have been made on AEMs until recent years. Zhao et al.[225] investigated the morphology of an anion exchange membrane by using small angle neutron scattering (SANS) technique. Their results revealed an ordered lamellar morphology that contains three phases in a water equilibrated membrane. As is shown in Figure 5.4, the three phases include: phase (1) crystalline ethylene tetrafluoroethylene (ETFE) domains, which offer good mechanical properties; phase (2) hydrophobic amorphous domains, which are made up of amorphous ETFE chains and offer a matrix to create conducting regions; phase (3) interconnected hydrated domains, which are composed of the entire graft chains and water and play a key role in promoting the conductivity.[225] Moreover, from (a) to (b) in Figure 5.4, the lamellar d-spacing (related to the repeating distances between planes of atoms in the structure) and the inter-grain distance both increased, which was attributed to water being presented in the membrane. Similarly, a small angle X-ray scattering (SAXS) study suggested that the AEM consists an ordered lamellar morphology which containing hydrophilic and hydrophobic phase separations.[226] As the hydration of the membrane changed from dry to wet state; the d-spacing increased from 45 to 97 nm. In addition, transmission electron microscopy (TEM) was also used to study the AEM morphology. The results showed distinct hydrophilic and hydrophobic phase-separated,

bicontinuous structures in the membrane,[227] as illustrated in Figure 5.5. In summary, the studies of AEMs suggested that the membranes have hydrophilic-hydrophobic phase separated morphology. Compared to fluoro-carbon based proton exchange membranes, however, the AEMs usually have less degree of phase separation, due to most AEMs are based on hydrocarbon backbones with lower hydrophobicities.[1]

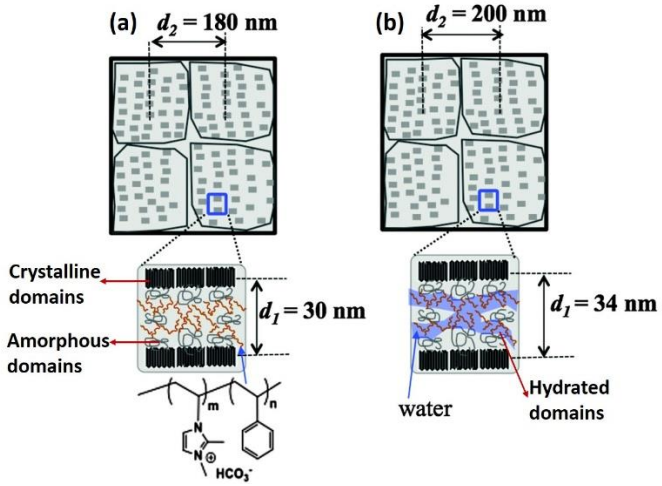

Figure 5.4 **Schematic illustrations of the morphology of (a) dry grafted ETFE membranes or AEMs; and (b) AEMs equilibrated in water. d_1 represents the d-spacing of lamellar and d_2 represents the inter-grain distance.(Adapted from ref.[225] Royal Society of Chemistry, Copyright 2016)**

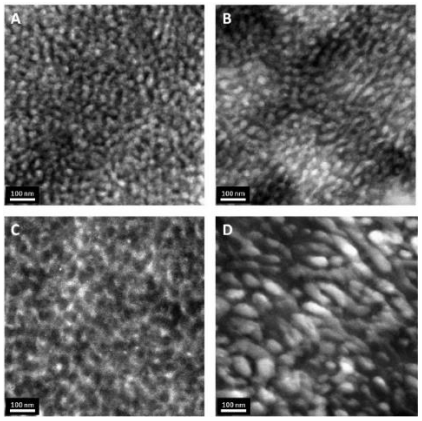

Figure 5.5 **STEM micrographs of a model block copolymer membranes. The bright regions are hydrophilic domains, while the dark regions are the hydrophobic domains. The IEC of the membrane increased from 1.17 to 1.92 mmol g^{-1} for membrane A to D. (Reprinted from ref.[227] with the permission of American Chemical Society, copyright 2015)**

5.1.3.2. Ion transport in anion exchange membranes

The fundamental understanding of hydroxide ion transport along with water through anion exchange membranes (AEMs) is not abundant in the literature. There are continued debates on the exact transport mechanism of hydroxide through the AEMs. Nevertheless, it was found that the hydroxide transport mechanisms in the AEMs could be comparable to that of the transport of protons in proton exchange membranes (PEMs).[228-230] For example, Figure 5.6 illustrates Grotthuss mechanism for hydroxide transport in water based on structure diffusion, which is similar to that of proton transport. However, recently, Chen et al.[231] suggested that the vehicular mechanism contributes considerably more than the Grotthuss mechanism for hydroxide transport in the AEMs. To date, no unanimous agreement on the exact mechanism and the relative importance of the different transport mechanisms for hydroxide transport occurring in AEMs, it can be any combination of the mechanisms described above.

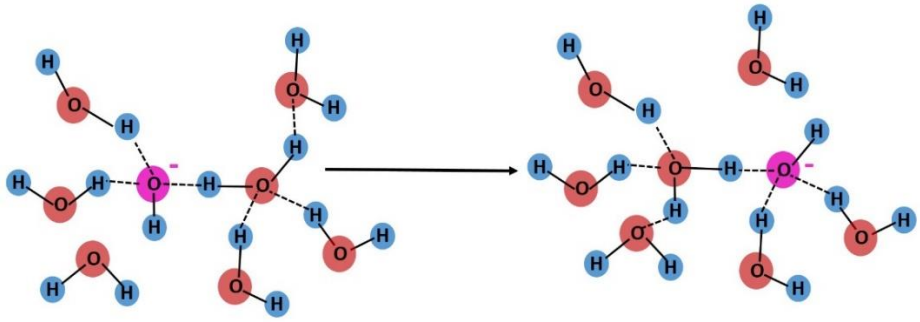

Figure 5.6 Schematic illustration showing Grotthuss mechanism for hydroxide transport in water. (Adapted from ref.[232] with the permission of Nature, Copyright 2002)

5.1.4. Motivation and approaches of this chapter

To date, anion exchange membranes (AEMs) stability and ion conductivity receive the most attention, with water transport receiving relatively little, even though it is widely accepted that the operation of fuel cells requires water management.[217,233-235] In order to achieve optimal water management in the cell, a highly water-permeable membrane is required to facilitate the anode water removal towards the cathode in AEMFCs.[68] Of particular interest to our group are the polybenzimidazolium anion exchange membranes (AEMs), which possess heterocyclic rings to delocalize positive charges.[219] A sterically,

C2-protected poly(benzimidazolium) AEM, HMT-PMBI (Figure 5.7), was chosen for this work due to its exceptional *in-situ* and *ex-situ* properties, its ease of synthetic scale-up, and its readily controllable ion exchange capacity (IEC).[138] HMT-PMBI is prepared by methylation of poly[2,2'-(2,2",4,4",6,6"-hexamethyl-p-terphenyl-3,3"-diyl)-5,5'-bibenzimidazole] (HMT-PBI). Through control of the degree of methylation (dm), between two and four methyl groups per repeat unit (50% to 100% dm), the resulting IEC may be precisely controlled between zero and 2.33 mmol g^{-1}(iodide form).[139]

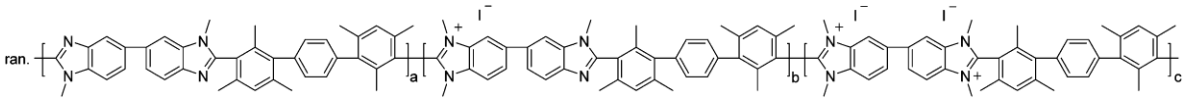

Figure 5.7. The molecular structure of 50-100% dm HMT-PMBI (I^- form), where dm represents the degree of methylation.

The objective of this chapter is to investigate water permeation through HMT-PMBI membranes. This is the first study on water permeation through benzimidazolium-containing AEMs. In addition, it is the first report of interfacial and internal water permeation resistances of AEMs in which these two permeation resistances are decoupled from the overall water permeation resistance. Liquid-liquid water permeation (LLP) experiments were performed on HMT-PMBI AEMs exchanged with various counter ions at 25 °C to obtain insight into water transport through fully-hydrated membranes. It is should be noted that, although the OH^- form of the AEMs are most pertinent to AEMFCs operation, the CO_3^{2-} form of HMT-PMBI was chosen in-depth investigation of liquid-vapor water permeation (LVP) due to the rapid conversion of the OH^- form to mixed carbonates upon expose to CO_2.[235,223,236] LVP measurements were performed at 70 °C under low relative humidity (RH) on the vapor side, in order to mimic fuel cell operating conditions. Thickness dependences on rates of liquid-liquid permeation (LLP) and liquid-vapor permeation (LVP) through HMT-PMBI enabled the internal and interfacial water transport resistances to be deconvoluted from the total water transport resistance. Water transport through two series of commercial solid polymer electrolyte membranes: anion exchange membrane - Fumapem® FAA-3, and proton exchange membrane - Nafion®, were also investigated for comparative purposes. At the end of this chapter, the impact of membrane degree of methylation (ion exchange capacity, IEC) on water permeation was studied. In addition, the impact of membrane surface modification on water permeation was

investigated, herein a catalyst containing ionomer solution was spray-coated on the surface of membranes.

5.2. Experiment

5.2.1. Materials

K_2CO_3 and KCl were purchased from ACP chemicals. KI was purchased from Caledon Laboratory Chemicals. K_2SO_4, KBr, and dimethylsulfoxide (DMSO) were purchased from BDH chemicals. KOH was purchased from Macron fine chemicals, $KHCO_3$ was purchased from Fisher Science Education. Decane was purchased from Fisher Scientific. All these chemicals were reagent grade and used as-received. DI water (18 MΩ) was used from Millipore Gradient Milli-Q.

Commercial Nafion® membranes, possessing an equivalent weight (EW) of 1100 g mol^{-1} (IEC 0.91 mmol g^{-1}) and dry thicknesses of 25 (NR211), 54 (NRE212), 131 (NF115) and 181 μm (N117), were used as-received (Sigma-Aldrich). Non-crosslinked Fumapem® FAA3 membranes (abbreviated as Fumapem®) were supplied by Fumapem®-Tech and possessed dry thicknesses of 19, 24, 31, 40 and 50 μm. The synthesis of HMT-PMBI was reported previously.[139] HMT-PMBI membranes are reported with the respective degree of methylation rather than ion exchange capacity (IEC) as the IEC is dependent on the nature of the anion.

5.2.2. Membrane preparation

5.2.2.1. HMT-PMBI membrane casting

HMT-PMBI membranes with three degrees of methylation (dm) were prepared using the following method. HMT-PMBI (I^-) form polymer was dissolved in DMSO by stirring and gently heating for 12 h to obtain solutions with a concentration of 7 or 10% (wt/wt) polymer, respectively. After vacuum filtering through a glass fiber filter, the solution was cast on a levelled glass plate using a K202 Control Coater casting table and an adjustable doctor blade (RK Print Coat Instruments Ltd). The polymer film was dried in an

oven at 85 °C for at least 12 h, peeled off the glass plate upon immersion in Milli-pore water, soaked in Milli-pore water for 24 h, and dried under vacuum at 80 °C for 24 h. The obtained HMT-PMBI membranes (I^-, 89.3% degree of methylation) possessed dry thicknesses of 12, 23, 30, and 70 µm. HMT-PMBI (I^-, 85.9% dm) possessed dry thicknesses of 18, 38, 53 and 65 µm. HMT-PMBI (I^-, 82.5%) membranes have dry thicknesses of 18, 35, 54 and 69 µm.

5.2.2.2. Anion exchange process

As-received Fumapem® FAA3 membranes (Br^- form) were submerged in 1 M K_2CO_3 and KCl solution to convert the membrane to the CO_3^{2-} and Cl^- form (exchanged twice). HMT-PMBI membranes were ion-exchanged according to our previously reported procedure.[13] HMT-PMBI membranes (I^-, 89.3% dm) were twice soaked in 1 M KOH, $KHCO_3$, K_2CO_3, K_2SO_4, KBr, or KCl aqueous solutions for at least 2 days each to obtain the OH^-, HCO_3^-, CO_3^{2-}, SO_4^{2-}, Br^-, or Cl^- form of the membranes followed with washing with Milli-pore water to remove residual ions. Membranes were stored in Milli-pore water prior to use. (note: OH^- form were operated under Ar purged conditions).

5.2.2.3. Catalyst-coated HMT-PMBI membranes

Catalyst ink was prepared using the following procedure: MeOH/ water in a 3:1 wt/wt ratio was added to carbon supported platinum catalyst (TKK TEC10E50E, 44.6 wt% Pt on graphitized carbon) and stirred, wherein water was added to the Pt/C powder, and then methanol was added. The ionomer (iodide-form HMT-PMBI) was dissolved in the methanol to form 5 wt% ionomer dispersion. Catalyst ink was stirred continuously as the ionomer dispersion was added at a rate of 1 drop/second. The resultant catalyst ink (1.0 wt% solids) was stirred for 1 h and sonicated in a low-power sonication bath for 30 min after formulation. The solids were comprised of 85 wt% Pt/C and 15 wt% HMT-PMBI ionomer. Prior to use, the ink was stirred for 1 h and sonicated for 15 min.

Catalyst ink was applied to HMT-PMBI membranes (I^-, 82.5% dm) by using sonicating-head spray-coater (Sono-Tek Exacta coat®), with the membranes immobilized on a heated vacuum table (110 °C). (Note: 82.5% dm was randomly chosen for this case study). Electrodes were formed to the desired loading, 0.6 mg Pt/cm^2.

5.2.3. Ion exchange capacity (IEC)

5.2.3.1. IEC of HMT-PMBI membranes

Ion exchange capacity of HMT-PMBI membranes were calculated according to Equation 5.8:[139]

$$IEC_H(mmol\ g^{-1}) = \frac{1000\times\left(\frac{2[2(dm-0.5)]eq.OH^-}{1\ repeat\ unit}\right)}{MR_{100}[2(dm-0.5)]+MR_{50}[1-2(dm-0.5)]} \qquad \text{Equation 5.8}$$

where dm is the degree of methylation ($\frac{\text{dm }\%}{100}$), $\mathrm{MR_{100}}$ and $\mathrm{MR_{50}}$ are the mass of one repeating unit in 100% dm of HMT-PMBI-OH^- ($\frac{636.8244\ \text{g}}{\text{repeat unit}}$) and in 50% dm of HMT-PMBI-OH^- ($\frac{572.7406\ \text{g}}{\text{repeat unit}}$), respectively.

5.2.3.2. IEC of Fumapem® FAA-3 membrane

The ion exchange capacity (IEC) of Fumapem® FAA3 membranes was determined using the titration method on the membrane in its Cl^- form. The IECs of other anionic forms were calculated based on the IEC of the Cl^- form, noting the different atomic/molecular masses of the anions incorporated. Three pieces of as-received membranes (Br^- form, ~ 0.1 g) were soaked in 1 M KCl solution for 48 h to obtain the Cl^- form, soaked in Milli-pore water and washed with Milli-pore water to remove residual ions. The membranes (Cl^- form) were submerged in 0.5 M $NaNO_3$ for 48 h, the fresh $NaNO_3$ solution was used every 12 h. and the membranes were then washed with Milli-pore water for 48 h. All $NaNO_3$ solutions were combined and titrated with 0.0100 M $AgNO_3$, using 10 drops of K_2CrO_4 (5 wt%) as a colorimetric indicator. The membranes were exchanged back to the Cl^- form after titration and dried at 80 °C under vacuum for 12 h to obtain the dry weight (W_{dry}). A Milli-pore water solution was also titrated as the control. The measured IEC value was calculated using the following equation:

$$IEC\,(mmol\,g^{-1}) = \frac{\left(V_{t,AgNO_3},mL \times C_{AgNO_3},M\right) - \left(V_{b,\,AgNO_3},mL \times C_{AgNO_3},M\right)}{W_{dry}\,(g)} \qquad \text{Equation 5.9}$$

where $V_{t,AgNO_3}(mL)$ and $V_{b,AgNO_3}(mL)$ are the volumes of $AgNO_3$(aq.) obtained in the titration of the membrane and the control solution, respectively; $C_{AgNO_3}(M)$ is the molar concentration of $AgNO_3$(aq.); and W_{dry} (g) is the dry weight of the membrane.

5.2.4. Effective water diffusion coefficient and mass transfer coefficient

Effective water diffusion coefficient (D') and effective mass transfer coefficient (k') were estimated according to the following equations:

$$C_w^{wet}\ (M) = \frac{\frac{(W_{wet}-W_{dry})(g)}{\rho_{H_2O}\,(g\,cm^3)\times M_{H_2O}\,(mol\,g^{-1})}}{V_{wet}\,(cm^3)} \quad \text{Equation 5.10}$$

$$\Delta C_w^{interface}\ (M) = \frac{\frac{(W_{wet'}-W_{dry})\,(g)}{\rho_{H_2O}\,(g\,cm^3)\times M_{H_2O}(mol\,g^{-1})}}{V'_{wet}(cm^3)} \quad \text{Equation 5.11}$$

$$\Delta C_w^{internal} = C_w^{wet} - \Delta C_w^{interface} \quad \text{Equation 5.12}$$

$$D'(cm^2\,s^{-1}) = \frac{J\,(mol\,m^{-2}s^{-1})\times T(m)}{\Delta C_w^{internal}(mol\,L^{-1})} \quad \text{Equation 5.13}$$

$$k'(cm\,s^{-1}) = \frac{J\,(mol\,m^{-2}s^{-1})}{\Delta C_w^{interface}(M)} \quad \text{Equation 5.14}$$

where $\Delta C_w^{internal}$ and $\Delta C_w^{interface}$ are the differential water concentration within and at the surface of the membrane, respectively. W_{wet} and V_{wet} are the weight and volume of the membrane at fully hydrated conditions, respectively. W_{wet}' and V_{wet}' are the wet weight and volume of the membrane in contact with water vapor (i.e., 40% relative humidity), respectively. W_{dry} is the membrane dry weight. ρ_{H_2O} is water density. M_{H_2O} is the molar mass of water. J is water permeation flux, and T is the effective wet thickness of the membrane.

5.2.5. Other techniques

The detailed experimental procedures of water permeation, water sorption, dry density, surface water contact angle (θ) were introduced in Chapter 2. The calculation of effective pore size, the permeability and resistance of water transport through membranes can be found in Chapter 2.

5.3. Results

5.3.1. Water sorption

Liquid water sorption measurements were performed on HMT-PMBI (89.3% dm) membranes in various anionic forms (i.e., OH^-, HCO_3^-, CO_3^{2-}, SO_4^{2-}, Cl^-, Br^- and I^-) at 25 °C for membranes completely immersed in water. Fumapem® and Nafion®211 were used as baselines for comparison. Membrane sorption data is summarized in Table 5.1. HMT-PMBI (CO_3^{2-}) possessed a λ value of 21 mol H_2O per mol $CO_3^{2-}$and water volume fraction (X_v) of 0.51. λ value of HMT-PMBI decreases in the order HCO_3^- > Cl^-> CO_3^{2-} > OH^-> SO_4^2 > Br^- > I^-. X_v decreases in the order of HCO_3^- > Cl^- = CO_3^{2-} = OH^- >SO_4^2 > Br^- > I^-. Fumapem® (CO_3^{2-}) exhibited a λ value of 13 H_2O per CO_3^{2-} and a water volume fraction of 0.37. Nafion® NR211, for comparison, possessed λ of 12 and X_v of 0.28 at 25 ˚C, which are consistent with previous reports.[11,34]

HMT-PMBI consistently exhibited larger λ and higher water volume fractions (X_v) values than Fumapem® for a given anion. For instance, HMT-PMBI (CO_3^{2-}) was found to possess a 44% larger λ and a 25% higher X_v than Fumapem® (CO_3^{2-}). In comparison to water sorption of other AEMs structures reported in the literature, significant differences exist due to the variations in the polymer structures and IEC values reported.[237-240] For instance, a poly(2,6- dimethyl-1,4-phenylene oxide)-based AEM with IEC of 3.35 mmol g^{-1} is reported to possess a λ value of 51 in its OH^- form,[240] which is > 2 times higher than HMT-PMBI (OH^-) (IEC 2.52 mmolg^{-1}); whereas another type of quaternary ammonium functional poly(phenylene oxide) in its OH^- form[241] exhibited significant lower λ values (4 - 15) for IECs between 1.3-1.5 mmol g^{-1}. Also of note, HMT-PMBI (OH^-) membranes possessed a 37% larger λ and 45% higher water volume fraction (X_v) than Nafion®

211(H^+), which may reflect the significant higher ion exchange capacity of these particular HMT-PMBI membranes.

Table 5.1 Liquid-Liquid water permeation (LLP) data for HMT-PMBI membranes (89.3% dm, various anionic forms), Fumapem® (I^- and CO_3^{2-} forms), and Nafion® 211 (H^+ form) at 25 °C.

Membranes	IEC (mmol g^{-1})	λ[a]	X_v[b]	T[c] (μm)	P_{LLP}[d] $\times 10^{17}$ ($m^2 Pa^{-1} s^{-1}$)	r[e] (nm)
HMT-PMBI[f]						
OH^-	2.52	19±1	0.51±0.01	61±2	7.3±0.3	3.8±0.1
Cl^-	2.41	22±2	0.51±0.01	33±1	2.5±0.1	1.6±0.1
Br^-	2.18	10±1	0.33±0.01	27±1	0.82±0.05	0.84±0.05
I^-	1.98	6±1	0.23±0.01	25±1	0.18±0.04	0.38±0.01
HCO_3^-	2.27	25±2	0.54±0.01	36±2	3.5±0.2	2.0±0.1
CO_3^{2-}	2.44	21±1	0.51±0.02	28±2	4.1±0.4	1.9±0.2
SO_4^{2-}	2.34	17±1	0.46±0.01	33±2	3.0±0.1	1.8±0.1
Fumapem® (I^-)	1.68±0.02	2±1	0.08±0.03	17±2	0.025±0.03	0.11±0.02
Fumapem® (CO_3^{2-})	1.89±0.03	13±1	0.37±0.01	33±1	0.76±0.05	0.9±0.1
Nafion® 211 (H^+)	0.91±0.02	12±2	0.28±0.03	31±2	6.5±0.4	2.5±0.1

[a.] Hydration number (immersed). HMT-PMBI and Fumapem®: mol H_2O per mol counter anion; Nafion®: mol H_2O per mol $-SO_3H$; [b.] Water volume fraction (immersed); [c.] Membrane wet thickness; [d.] Liquid-liquid water permeability; [e.] effective pore radius. [f.] IEC of HMT-PMBI membranes was determined using NMR spectroscopy.

5.3.2. Liquid-liquid water permeation (LLP)

The liquid-liquid water permeation flux (J_{LLP}) through HMT-PMBI membranes in various counter anion forms (i.e., OH^-, HCO_3^-, CO_3^{2-}, SO_4^{2-}, Cl^-, Br^- and I^-) was measured at 25 °C. This temperature was chosen because certain anion-forms swelled extensively at higher temperature (see Figure 5.8), e.g., Cl^- and HCO_3^- form, which rendered LLP measurements difficult.

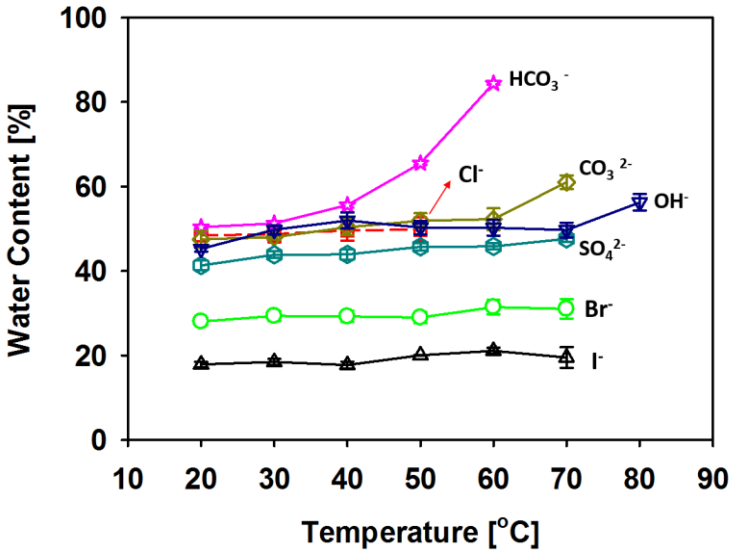

Figure 5.8 Water content as a function of temperature for HMT-PMBI (89.3% dm) membranes comprising different counter ions.

Liquid-liquid water permeation flux (J_{LLP}) as a function of differential pressure is plotted in Figure 5.9 and compared with Fumapem® and Nafion® 211 membranes. J_{LLP} was observed to increase linearly with increasing differential pressure for all membranes, which is consistent with data previously reported for Nafion® membranes.[13,71,123] The permeance (P), calculated from the slope of each plot in Figure 5.9, was normalized to the membrane wet thickness (T) to obtain the respective liquid-liquid water permeability value (P_{LLP}), which is listed in Table 5.1. The water permeability of HMT-PMBI membranes decreases in the order of $OH^- > CO_3^{2-} > HCO_3^- > SO_4^{2} > Cl^- > Br^- > I^-$.

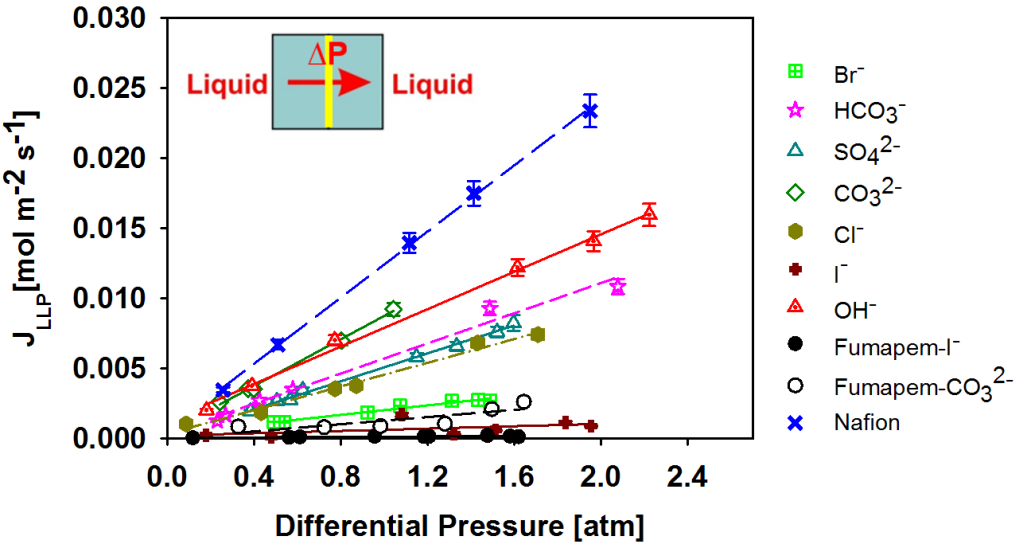

Figure 5.9 **Liquid-liquid water permeation flux as a function of differential pressure for HMT-PMBI (89.3% dm, various counter-anions), Fumapem® (I^- and CO_3^{2-}), and Nafion® 211 (H^+) membranes at 25 °C. HMT-PMBI (OH^-) sample performed in an Ar-purged atmosphere. Film thickness are listed in Table 5.1.**

Based on the measured LLP permeability (P_{LLP}) values,[146,175] the effective hydrophilic pore radius (r) for the transport of water through the membranes were calculated, and shown in Table 5.1. The effective hydrophilic pore radius of HMT-PMBI (OH^-) was calculated to be 3.8 nm, which is the largest of the HMT-PMBI series investigated. For the other anions of HMT-PMBI, the effective hydrophilic pore radius follows the trend HCO_3^- > CO_3^{2-} > SO_4^2 > Cl^- >Br^- > I^-. Nafion® 211 is calculated to have an effective hydrophilic pore radius of 2.5 nm, which agrees well with that of literature data,[146,175,199] whereas the effective hydrophilic pore radius of Fumapem® (CO_3^{2-}) was calculated to be much lower, 0.9 nm.

5.3.3. Liquid-vapor water permeation (LVP)

The dependence of relative humidity (RH) on liquid-vapor water permeation flux (J_{LVP}) for HMT-PMBI (CO_3^{2-}), Fumapem® (CO_3^{2-}) and Nafion® at 70°C is plotted in Figure 5.10 (a). J_{LVP} increased as the relative humidity, and hence water activity, on the vapor side decreased, which serves to develop a larger activity (chemical potential) gradient across the membranes. Liquid-vapor permeability (P_{LVP}) at 70 ˚C, obtained by normalizing

the permeance (slope of plots in Figure 5.10 (b)) to membrane thickness (T_M), is summarized in Table 5.2. The liquid-vapor water permeability (P_{LVP}) of Nafion® is calculated to be 1.71×10^{-6} mol^2 m^{-1} s^{-1} kJ^{-1}, similar to reported data.[71,199] The liquid-vapor water permeability (P_{LVP}) decreases across the series in the order Nafion® (H^+) > HMT-PMBI (CO_3^{2-}) > Fumapem® (CO_3^{2-}), consistent with the order that observed in the liquid-liquid water permeability (P_{LLP}).

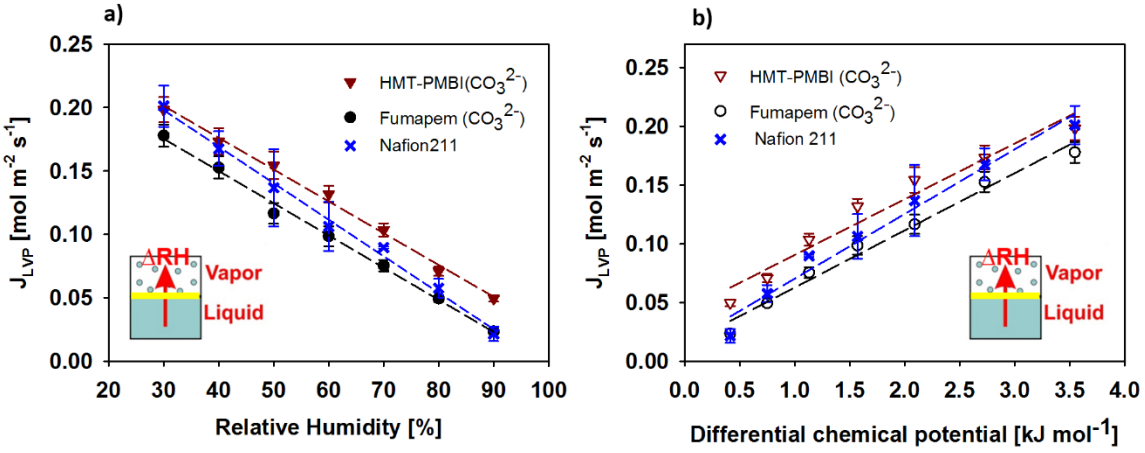

Figure 5.10 **Liquid-vapor water permeation flux (J_{LVP}) of HMT-PMBI (CO_3^{2-}), Fumapem® (CO_3^{2-}) and Nafion® membranes as a function of (a) relative humidity; and (b) differential chemical potential ($\Delta\mu$) at 70 °C.**

Table 5.2 **Liquid-vapor water permeability (P_{LVP}) of HMT-PMBI (CO_3^{2-}), Fumapem® (CO_3^{2-}), and Nafion® membranes at 70 °C.**

Membranes	IEC (mmol g^{-1})	X_v[a]	T_M[b] (μm)	$P_{LVP}\times10^6$ (mol^2 m^{-1} s^{-1} kJ^{-1})
HMT-PMBI (CO_3^{2-})	2.44	0.60±0.02	35±2	1.66±0.05
Fumapem® (CO_3^{2-})	1.89±0.03	0.45±0.02	33±2	1.61±0.04
Nafion® 211(H^+)	0.91±0.02	0.44±0.02	31±1	1.71±0.02

[a] Water volume fraction (X_v) was measured at 70˚C, under fully hydrated condition. [b] Effective wet thickness of the membrane.

5.3.4. Resistance to water permeation

From the measured water permeation flux (J) and calculated values of differential chemical potential ($\Delta\mu$), the overall resistance to water permeation (R) was estimated using Equation 1.7 in Chapter 1, as described in the Experimental Section. For liquid-liquid water permeation (LLP) at 25 °C, the permeation flux (J_{LLP}) as a function of differential chemical potential is shown in Figure 5.11. In the case of liquid-vapor water permeation (LVP), at 70 °C and 40% RH, the chemical potential (μ) of water vapor and liquid water were calculated to be -237.08 kJ mol^{-1} and -240.32 kJ mol^{-1}, respectively.[71,86] The difference in chemical potential ($\Delta\mu_{LVP}$) between both sides of the membrane was calculated to be 2.73 kJ mol^{-1}.

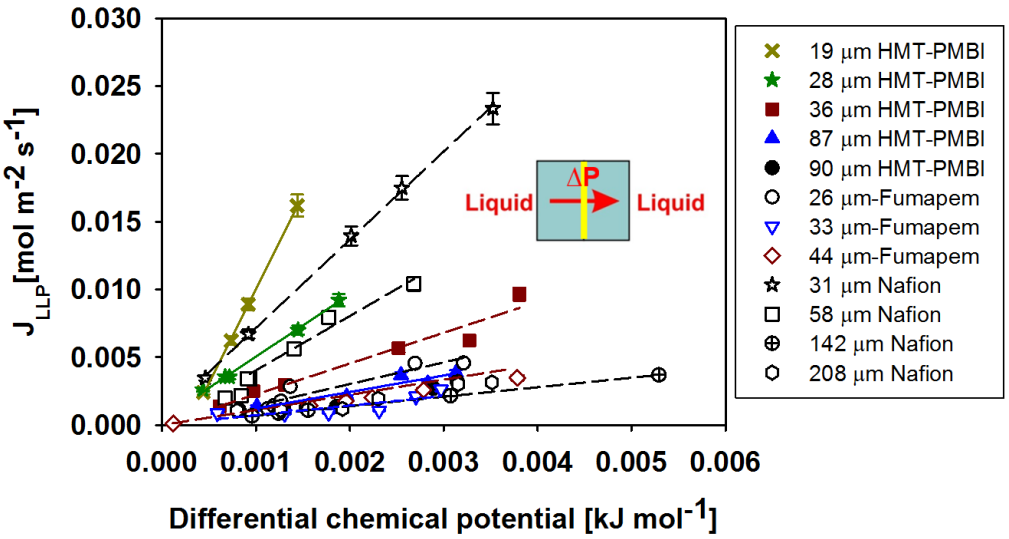

Figure 5.11 Liquid-liquid water permeation flux of membranes possessing different thicknesses as a function of differential chemical potential at 25 °C. HMT-PMBI (CO_3^{2-}) - closed symbols, Fumapem® (CO_3^{2-}) and Nafion® (H^+) -open symbols.

The thickness dependence on permeation flux (J_{LVP}) at 70 °C and 40% RH is plotted in Figure 5.12. The overall water permeation resistance (R) of liquid-liquid water permeation (LLP) and liquid-vapor water permeation (LVP) are plotted as a function of membrane thickness in Figure 5.13. R_{LLP} and R_{LVP} both decrease with decreasing membrane thickness, as water permeates faster through thinner membranes. For liquid-liquid water permeation, HMT-PMBI membranes exhibited R_{LLP} resistances of 0.20, 0.22,

0.42, 0.74 and 0.97 kJ m^2 s mol^{-2} for wet thickness of 19, 28, 36, 87 and 90 µm, respectively. These values are significantly smaller than those observed for Fumapem®(CO_3^{2-}) which exhibited R_{LLP} resistances of 0.56, 0.71 and 0.89 kJ m^2 s mol^{-2} for the thickness of 26, 33 and 44 µm, respectively. The resistance liquid-vapor water permeation (R_{LVP}) was found to be more than one order of magnitude greater than liquid-liquid water permeation (R_{LLP}), despite the measurements being performed at a much higher temperature (70 °C vs. 25 °C).

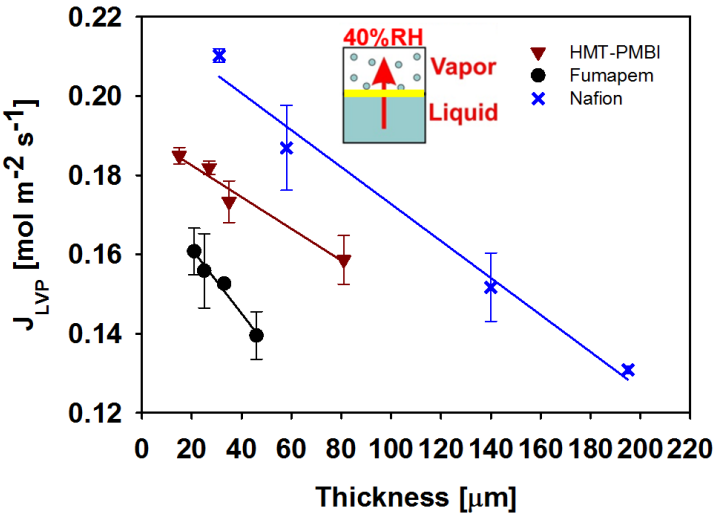

Figure 5.12 Effective wet thickness dependence of liquid-vapor water permeation (LVP) fluxes of HMT-PMBI (CO_3^{2-}), Fumapem® (CO_3^{2-}), and Nafion® at 70°C and 40% RH.

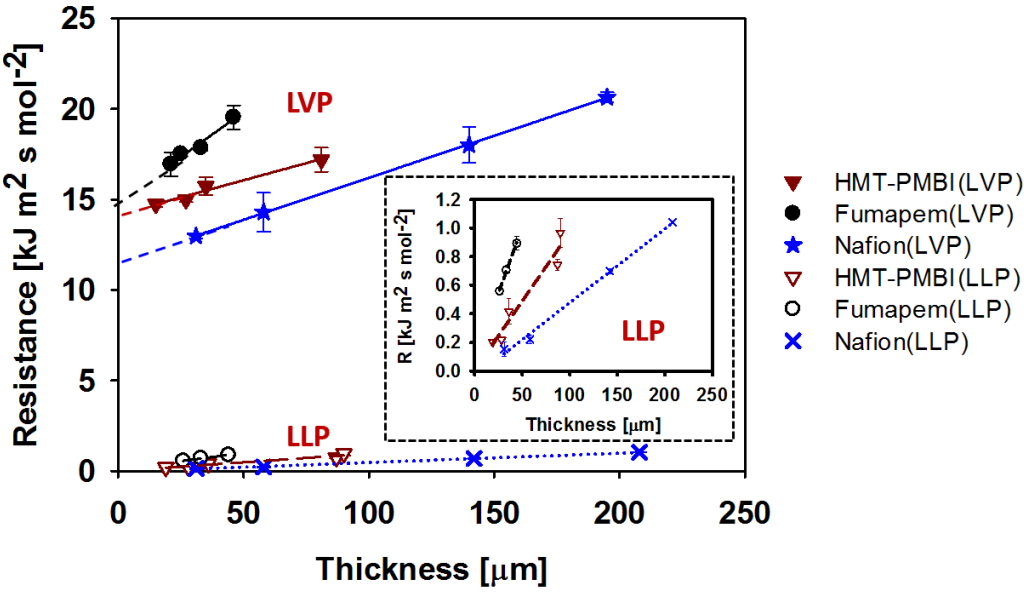

Figure 5.13 Water permeation resistance of liquid-liquid (LLP) and liquid-vapor permeation (LVP) as a function of effective wet membrane thickness for HMT-PMBI (CO_3^{2-}), Fumapem® (CO_3^{2-}) and Nafion® (H^+). Inset: expanded, 0-1 kJ m^2 s mol^{-2}, region. LLP was performed at 25 ˚C, fully hydrated conditions. LVP was performed at 70 ˚C, 40% RH, where resistance is calculated from Equation 1.7, described in Chapter 1.

5.3.5. Interfacial water permeation resistance

In order to examine the relative importance of the membrane/water interface on permeation to water, the overall water permeation resistance (R) is deconvoluted into $R_{interfacial}$ (obtained from the intercept on plot in Figure 5.13 extrapolated to zero thickness) and $R_{internal}$ ($R_{internal} = R - R_{interfacial}$). As shown in Figure 5.13, both AEM types (i.e., HMT-PMBI and Fumapem®) exhibit non-zero intercepts for liquid-vapor water permeation (LVP), indicating the existence of an interfacial resistance. $R_{interfacial}$ of liquid-liquid water permeation (LLP) for both HMT-PMBI and Fumapem® membranes yielded negligible value, which is consistent with the findings of proton exchange membranes from past studies.[13,86,106]

The effective internal liquid-vapor water permeation coefficient ($k'_{LVP\_internal}$) was estimated from the slope ($k'_{LVP\_internal} = \frac{1}{slope}$) of the plot for liquid-vapor water permeation

(LVP) resistance vs. membrane thickness shown in Figure 5.13. The intercept of plot for LVP in Figure 5.13 yields the effective interfacial water permeation coefficient ($k'_{LVP\_interfacial} = \frac{1}{intercept}$). As summarized in Table 5.3, water permeation through the membrane interface ($k'_{LVP\_interfacial}$) is ~ 2 orders of magnitude lower than through the bulk of the membrane ($k'_{LVP\_internal}$), in agreement with studies for Nafion®-based membranes.[85,106,173,242,243]

Table 5.3 Liquid-vapor water permeation coefficient ($k'_{LVP\_internal}$) and interfacial water permeation coefficient ($k'_{LVP\_interfacial}$) of HMT-PMBI (CO_3^{2-}), Fumapem® (CO_3^{2-}) and Nafion® (H^+) membranes.

Membranes	$k'_{LVP\_internal}$[a] (mol² m⁻¹ s⁻¹ kJ⁻¹)	$k'_{LVP\_interfacial}$ [a]×10² (mol² m⁻² s⁻¹ kJ⁻¹)
HMT-PMBI(CO_3^{2-})	26.5±3.1	7.1±0.1
Fumapem®(CO_3^{2-})	10.1±1.3	6.7±0.2
Nafion®	21.6±0.3	8.7±0.1

[a.] Data was calculated from the LVP experiment at 70˚C, where one side of the membrane was exposed liquid and the other to water vapor (40% RH).

The effective internal liquid-vapor water permeation coefficient ($k'_{LVP\_internal}$) of HMT-PMBI (CO_3^{2-}) membranes exhibited was calculated to be 26.5 mol² kJ⁻¹ m⁻¹ s⁻¹, which is ~60% larger than that found for Fumapem® (CO_3^{2-}) and 18% larger than for Nafion®. This is explained on the basis that HMT-PMBI (CO_3^{2-}) membrane possesses ~ 25% greater water volume content than Nafion® 211 (Table 5.2). With respect to the interfacial water permeation coefficient ($k'_{LVP\_interfacial}$), found for HMT-PMBI was ~ 5% larger than for Fumapem® and 18% smaller than for Nafion®(H^+).

In order to validate our measurements and data analysis, the effective internal permeation coefficient ($k'_{LVP\_internal}$) and interfacial permeation coefficient ($k'_{LVP\_interfacial}$) were converted to the effective water diffusion coefficient (D') and effective mass transfer coefficient, respectively, and compared to reported data (see Table 5.4). Nafion®211 was calculated to possess an effective water diffusion coefficient of 3.8 ×10⁻⁶ cm² s⁻¹, which is in good agreement with reported literature using various techniques under similar conditions.[64,80,104,105] Similarly, the calculated effective mass transfer coefficient (k') of Nafion® determined this work (see Table 5.4) is of the same magnitude as compared to

literature work.[64,80,113] Compared to pure water ($D' = 5.6\times10^{-5}$ cm^2 s^{-1}) at 70 ˚C,[244] the effective water diffusion coefficient (D') of the membranes studied is approximately one magnitude lower. The effective water diffusion coefficient was found to decrease in the order of HMT-PMBI > Nafion® > Fumapem®.

Table 5.4 Literature comparison of effective water diffusion coefficient and mass transfer coefficient for membranes.

Membranes	D' ×10^6 (cm^2 s^{-1})	k' ×10^3 (cm s^{-1})
HMT-PMBI (CO_3^{2-}, 70˚C)[a]	4.9±0.3	2.6±0.3
Fumapem® (CO_3^{2-}, 70˚C)[a]	2.0±0.5	3.0±0.3
Nafion®(70˚C)[a]	3.8±0.3	3.2±0.2
Nafion®(70˚C)	3-7 [ref.80]	~1.5 [ref.80]
H_2O (70˚C)	56 [ref.244]	-

[a.] Data was calculated from the LVP experiment at 70˚C in this work, where one side of the membrane was exposed liquid water and the other side to water vapor (40% RH).

Of the three classes of membranes studied, HMT-PMBI exhibits the largest ratio of interfacial resistance to the overall resistance ($R_{LVP\_interfacial}/R_{LVP}$) (see Table 5.5), indicating that the HMT-PMBI membrane interface plays a more dominant role in the overall resistance than the other two membrane series. It has been intimated in literature that $R_{interfacial}$ is controlled by a highly anisotropic dehydrated surface.[13,106] In order to investigate this assertion, surface water contact angle measurements were undertaken, the data for which are summarized in Table 5.5. HMT-PMBI exhibits a smaller surface contact angle (θ) for both dry and fully hydrated conditions, indicating that HMT-PMBI membrane possesses a rather hydrophilic surface compared to Fumapem® membrane. Both HMT-PMBI and Fumapem® membranes possess significantly smaller contact angles than Nafion®, which is explained on the basis that latter possess hydrophobic perfluorous species at the surface and lower water content.[194]

Table 5.5 Ratio of interfacial resistance to the overall resistance for liquid-vapor water permeation and contact angle data for HMT-PMBI (CO_3^{2}), Fumapem® (CO_3^{2-}), and Nafion® membranes.

Membranes	Thickness (μm)[a]	$\frac{R_{LVP\_interfacial_a}}{R}$	X_v[a]	ΔX_V (%)[b]	Dry θ (°)[c]	Wet θ (°)[c]
HMT-PMBI(CO_3^{2-})	27±2	0.95±0.05	0.12±0.02	80±6	67±2	54±1
Fumapem®(CO_3^{2-})	25±2	0.85±0.06	0.07±0.01	84±3	71±3	63±2
Nafion®(H^+)	31±2	0.89±0.04	0.10±0.01	77±2	97±3	69±2

[a] Measured at 40% RH, 70 ˚C. [b] The difference in water volume fraction (X_v) between wet and 40% RH condition. [c] Measured at room temperature.

As shown in Table 5.5, the ratios of $R_{LVP\_interfacial}/R_{LVP}$ for two anion exchange membranes (AEMs) with similar membrane thickness are both larger than 80%, indicating that $R_{LVP\_interfacial}$ is the dominant resistance in the transport of water through AEMs and which is consistent with that found for proton exchange membranes.[13,106] In addition, as plotted in Figure 5.14, the ratio of $R_{LVP\_interfacial}/R_{LVP}$ increases with decreasing membrane thickness, meaning that the membrane interface plays an increasing role. As reported previously for proton exchange membranes, a "water depletion layer" is proposed to exist in the membrane at the vapor/membrane surface,[137] which gives rise to a larger interfacial water permeation resistance. This is supported by the observation that the water volume fraction (X_v) of the membranes decreases significantly (~80%) (Table 5.5) when the membrane is exposed to vapor on both sides, as opposed to contact with liquid water on both sides (Table 5.2).

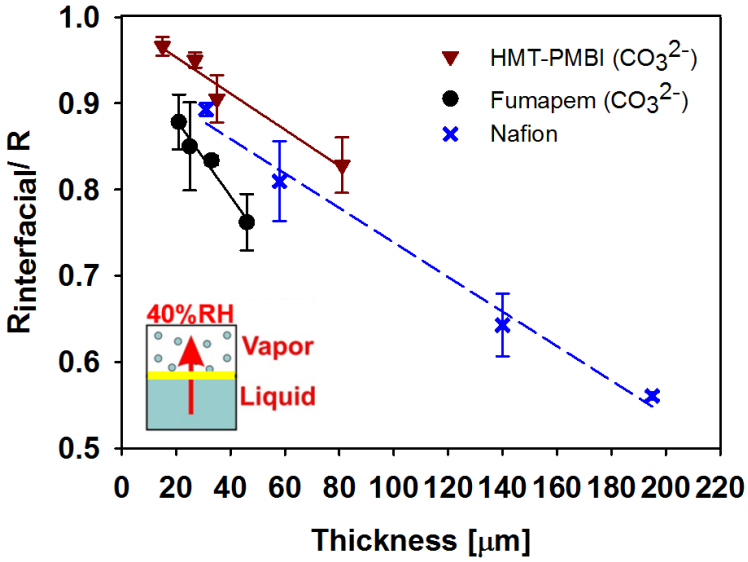

Figure 5.14 **Effective wet thickness dependence on the ratio of interfacial water permeation resistance to total resistance for HMT-PMBI, Fumapem® and Nafion® (H^+) at 70 °C under LVP conditions.**

5.3.6. The impact of degree of methylation (dm) on water permeation of HMT-PMBI (I^-) membranes

Liquid-vapor water permeation (LVP) was performed on HMT-PMBI (I^-) membranes with three varied degrees of methylation at 70 ˚C, 40% RH. Figure 5.15 shows the dependence on the degree of methylation (dm) upon LVP resistance of HMT-PMBI (I^-) membranes. As the dm increases, both of the slope and intercept of the plots in Figure 5.15 decrease. This result indicates that internal and interfacial (i.e., intercept of the plots) resistances to water transport decrease as increasing the degree of methylation of the polymer. The calculated corresponding effective water permeation coefficient on membrane internal and interface are summarized in Table 5.6. As the dm increases from 82.5% to 89.3%, the membrane ion exchange capacity (IEC) increases ~13%, the internal effective water permeation coefficient ($k'_{LVP\_internal}$) and interfacial effective water permeation coefficient ($k'_{LVP\_interfacial}$) increase 42% and 14%, respectively. The impact of dm on the ratio of interfacial resistance to total resistance of water permeation ($\frac{R_{interfacial}}{R}$) is plotted in Figure 5.16. For a normalized membrane thickness, $\frac{R_{interfacial}}{R}$ increases with

increasing dm (i.e., IEC), indicating that interfacial resistance plays more dominant role in the total resistance to water permeation as increasing dm of the membranes.

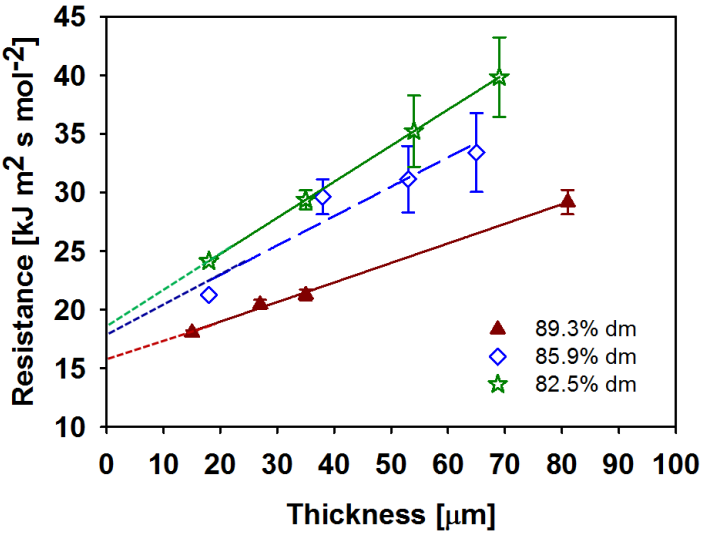

Figure 5.15 **Liquid-vapor water permeation resistance (R_{LVP}) as a function of effective membrane thickness of HMT-PMBI (I^-) at 70 °C, 40% RH, where resistance is calculated from Equation 1.7 in Chapter 1.**

Table 5.6 **Data summary of HMT-PMBI (I^-) membranes at varying degrees of methylation (dm).**

	dm (%)[d]	IEC (mmol g^{-1})[d]	X_v[a]	$k'_{LVP\_interfacial}$ $\times 10^2$ (mol^2 m^{-2} s^{-1} kJ^{-1})[b]	$k'_{LVP\_internal}$ (mol^2 m^{-1} s^{-1} kJ^{-1})[b]	Dry θ (°)[c]	Wet θ (°)[c]
HMT-PMBI (I^-)	89.3	1.98	0.24±0.01	6.3±0.3	5.6±0.2	71±1	58±3
	85.9	1.85	0.23±0.02	5.6±0.2	4.0±0.1	72±1	63±2
	82.5	1.72	0.22±0.01	5.4±0.2	3.2±0.2	78±1	64±3

[a.] Measured at 70 °C and wet condition. [b.] Measured at 70 °C and 40% RH. [c.] Measured at 25 °C. [d.] Determined by NMR spectroscopy.

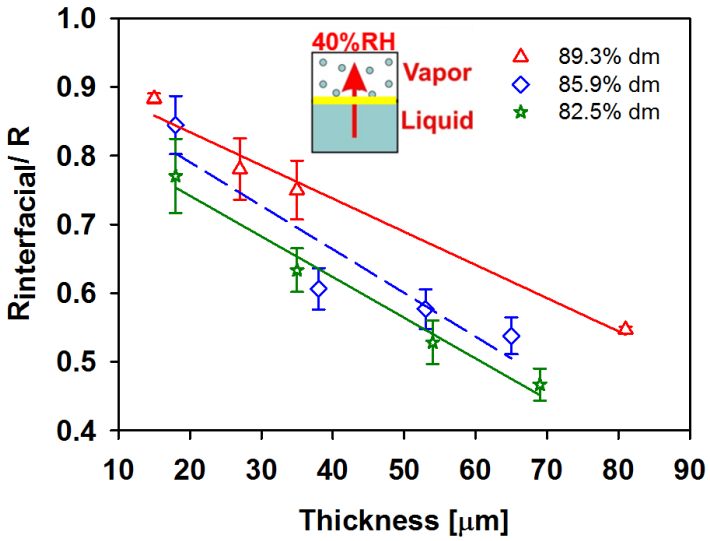

Figure 5.16 Interfacial water permeation resistance ratio to total resistance of HMT-PMBI (I^-) membranes at 40% RH and 70 °C. (dm = degree of methylation)

5.3.7. Catalyst-coated membranes

The membrane interfaces are found to play significant roles in the overall water permeation through HMT-PMBI membranes. Therefore, the surface of HMT-PMBI membranes was modified by spray-coating an ionomer containing catalyst ink layer. A liquid-vapor water permeation (LVP) study was conducted on HMT-PMBI (I^-, 82.5% dm) membranes before and after being spray-coated. Surprisingly, as shown in Figure 5.17, compared to the pristine HMT-PMBI membranes, the catalyst-coated membranes (CCM) exhibit almost identical values for both of the internal and interfacial water permeation resistance (summarized in Table 5.7) regardless of the membrane thickness.

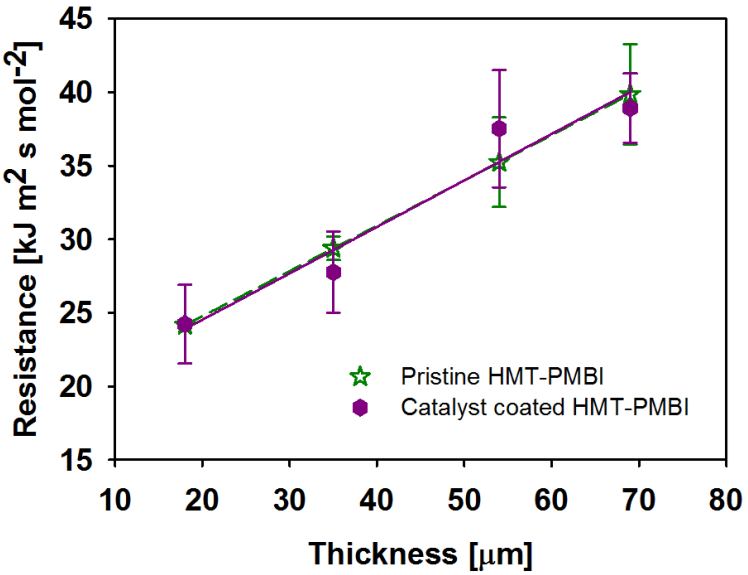

Figure 5.17 **LVP water permeation resistance as a function of the membrane thickness for catalyst coated – and pristine– HMT-PMBI (I^-, 82.5% dm) membranes at 70 °C and 40% RH.**

Table 5.7 **LVP resistances of pristine and catalyst coated HMT-PMBI (I^-, 82.5% dm) membranes (CCM) at 70 °C and 40% RH.**

Membranes	$R_{interfacial}$ (kJ m^2 s mol^{-2})	Slope of Figure 5.17
CCM	18.2±2.6	0.32±0.05
Pristine	18.6±0.1	0.31±0.01

5.4. Discussion

5.4.1. Liquid water sorption and liquid-liquid water permeation

Water sorption is theoretically suggested to be regulated by the balance of liquid, osmotic and elastic pressures, which are related to properties including the dielectric constant of water, charge density and the shear modulus of polymer walls.[2] In this work, water sorption was performed on HMT-PMBI (dm= 89.3%) membranes in various counter anion forms (i.e., HCO_3^-, OH^-, SO_4^{2-}, CO_3^{2-}, Cl^-, Br^- and I^-) at 25 °C (data is summarized in

Table 5.1). The dielectric constant of water is the same for all anion forms at the current water sorption experiment condition. Therefore, the differences in water content of these anion forms in this work is attributed to the different ion charge densities[245,246] and different moduli of polymer walls which were found to be inversely proportional to the effective pore size[2] (as shown in Table 5.1).

Water sorption properties were found to strongly affect water and ion transport through membranes.[113,137,199,246,247] However, no single correlation was observed between water content and liquid-liquid water permeability in HMT-PMBI membrane series. For example, the Cl^-, CO_3^{2-} and OH^- forms of HMT-PMBI exhibited different liquid-liquid permeability behaviour (Table 5.1), even though almost identical water content was observed. Likewise, HMT-PMBI (CO_3^{2-}) and Fumapem® (CO_3^{2-}) membranes, both possessing higher water content compared to Nafion®211 (H^+), exhibited lower liquid-liquid water permeability. This is not an entirely unexpected behaviour, given that hydrocarbon membranes generally possess less developed hydrophilic-hydrophobic phase separation,[247] and consequently less well-formed water/charge transport pathways in the membranes. On the other hand, even though these two anion exchange membranes (AEMs) possess significantly higher ion exchange capacity (IEC) than Nafion®211 (H^+), it is found that AEMs, in general, have a lower degree of charge dissociation,[230,247] which counterbalances higher IEC, resulting in less free charge concentration and constricted transport pathways compared to Nafion®.

5.4.2. Liquid-vapor water permeation

Liquid-vapor water permeation (LVP) measurements revealed that the thickness-normalized liquid-vapor water permeability (Table 5.2) showed the same trend with liquid-liquid water permeability (Table 5.1), namely, Nafion® (H^+)> HMT-PMBI (CO_3^{2-})> Fumapem® (CO_3^{2-}). Compared to Fumapem® (CO_3^{2-}), even though HMT-PMBI (CO_3^{2-}) possessed 5% greater liquid-vapor permeability, 80% larger liquid-liquid permeability was observed in HMT-PMBI (CO_3^{2-}). Permeation resistance to water (Figure 5.13) for all membranes were calculated for further investigation. A significantly smaller interfacial mass transport resistance was observed in liquid-liquid water permeation (LLP) than that

for liquid-vapor water permeation (LVP), due to the negligible interfacial water permeation resistance in LLP.

Internal and interfacial liquid-vapor water permeation resistances of membranes were quantified by thickness-dependent measurements at 70 °C and 40% RH, the effective permeation coefficient on membrane bulk and interface were determined (Table 5.3). HMT-PMBI (CO_3^{2-}) possessed a higher effective internal water permeation coefficient than both Fumapem® FAA-3 and Nafion® membranes (60 and 18% larger, respectively), presumably a result of the higher water volume fraction (X_v) of HMT-PMBI (CO_3^{2-}).

Compared to Fumapem® (CO_3^{2-}), HMT-PMBI (CO_3^{2-}) possessed 23% higher IEC and 6% lower water surface contact angle (Table 5.5), indicating HMT-PMBI (CO_3^{2-}) may possess a higher fraction of water transport sites on the membrane's surface. Moreover, HMT-PMBI(CO_3^{2-}) was found to possess a higher effective pore radius (53%, see Table 5.1) and much greater water volume fraction in both fully hydrated (Table 5.2) and 40% RH conditions (Table 5.5). Surprisingly, $k'_{LVP\_interfacial}$ for HMT-PMBI(CO_3^{2-}) is similar to Fumapem® (CO_3^{2-}), which can be explained by the fact that HMT-PMBI(CO_3^{2-}) possesses a larger ratio of interfacial resistance to the overall membrane permeation resistance (Table 5.5), because of a less well-structured water transport pathway at the membrane interface.[137,248]

5.4.3. The impact of degree of methylation on water permeation

The relationship between the degree of methylation (dm) of the membrane and water permeation was investigated using liquid-vapor (LVP) water permeation experiment. Both the effective internal and interfacial water permeation coefficient were found to increase significantly with increasing dm, as a result of the higher IEC and higher water content (X_v) (summarized in Table 5.6). This result indicates that varying the degree of methylation has an impact on membrane water permeation. Despite a decreasing surface water contact angle, the ratio of the interfacial water permeation resistance to the total resistance ($R_{LVP\_interfacial}/R_{LVP}$) was found to increase with dm, which can be attributed to less-ordered water permeation pathways on the membrane surface (illustrated in Figure 5.18). However, further experiments are needed to confirm this assertion.

Figure 5.18 Schematically diagram of water permeation pathway on membrane interface (white = aqueous domains), where the pathways of B are less-ordered than in A.

5.4.4. The impact of catalyst coated layer on water permeation

Catalyst ink layer was spray-coated on HMT-PMBI membranes (I^-, 82.5% dm). Surprisingly, no correlation was found between this surface spray-coating and the LVP water permeation resistance of HMT-PMBI membranes (I^-, 82.5% dm). This result agrees well with the findings in Adachi et al.'s work,[249] wherein the catalyst ink layer was coated on the Nafion® membranes. The reason of catalyst layer had no impact on LVP water permeation of membranes can be attributed to the large pore size of the catalyst layer.[69] As a consequence, water permeation through the membrane was not hindered. Moreover, it could be due to the water concentration, which drops sharply on the "depletion layer" region of the membrane (as discussed in Chapter 4, shown in Figure 4.9),[204,250,251] and that the membrane appears to be the bottleneck for LVP water permeation.

5.5. Conclusions

HMT-PMBI (CO_3^{2-}) membranes showed significantly higher liquid-liquid (LLP) and moderate liquid-vapor (LVP) water permeability than the commercial anion exchange membrane- Fumapem® (CO_3^{2-}), and only 5% less of LVP permeability compared to proton exchange membrane benchmark material, Nafion® (H^+).

For the first time, internal and interfacial water permeation resistances of anion exchange membranes are quantified by thickness-dependent permeation measurements. These analyses provide insight into the behaviour of water permeation through anion exchange membranes (AEMs). Liquid-liquid water permeation (LLP) through AEMs exhibits negligible permeation resistance at the membrane interface compared to liquid-vapor permeation (LVP) - similar to what is found for proton exchange membranes.[13,137] The overall resistance to LVP of water through membranes is an order of magnitude greater than for LLP. The effective internal liquid-vapor water permeation coefficient of HMT-PMBI (CO_3^{2-}) was calculated to be significantly larger than that of Fumapem® (CO_3^{2-}) and Nafion® (H^+) membranes. However, the effective interfacial water permeation coefficient of HMT-PMBI (CO_3^{2-}) was found to be similar to Fumapem® (CO_3^{2-}) but 14% smaller than Nafion® (H^+), even though HMT-PMBI (CO_3^{2-}) is found to possess a lower water surface contact angle and much higher water content.

The degree of methylation had a strong impact on the HMT-PMBI (I^-) membrane water permeation resistance. Internal and interfacial water permeation resistances of HMT-PMBI membranes decreased with increasing degrees of methylation, which is a consequence of increasing water content values. Catalyst layers were coated on HMT-PMBI membranes to modify the membrane surface. However, it appears that the catalyst layer had almost no influence on membrane water permeation. The reason could be due to the large pore size of the catalyst layer, which did not hinder the water transport through the membrane.

The observations of interfacial water permeation through membranes suggest that the membrane interface plays a crucial role in determining water permeation through *anion exchange membranes*. The results from this study can be beneficial to a fundamental understanding of multiple disciplines such as membrane/catalyst layer interfaces, thin films, as well as anion transport in anion exchange membranes.[252,253]

Chapter 6.

Conclusion and future work

6.1. Summary

An understanding of water permeation through polymer electrolyte membranes is crucial to offset the unbalanced water transport within fuel cells. This research work investigated the fundamental relationships between the polymer structure and water permeation of the membranes. Three types of water permeation experiments were performed in this thesis work and were based on applying the chemical potential gradients across the membrane. Three distinct membrane systems were investigated systematically under varied experimental conditions, each system comprising several membrane series. Correlations between the series were drawn and compared to the commercialized materials at each membrane system.

System one: degraded Nafion® membranes

The effects of chemical degradation, induced by Fenton's reagent reaction, upon water transport properties of Nafion® NR211 membranes were investigated in Chapter 3. Exposure to free radicals generated using Fenton's reagent caused morphological and structural changes to the membrane that exert a strong effect on transport properties. Liquid-liquid permeation (LLP), liquid-vapor permeation (LVP) and vapor-vapor permeation (VVP) measurements at 70 ˚C indicated that water permeability increased for degraded membranes as a result of larger water volume fraction and greater effective pore size, due to enhanced water sorption (under both partially and fully hydrated conditions). Similarly, a higher water content was responsible for an increase in proton mobility; despite the observation that ion exchange capacity (IEC) and proton conductivity decreased.

From the fuel cell performance point of view, the membrane degradation caused the reducing of membrane function, such as the loss of IEC and proton conductivity. The higher water permeation rates of degraded membranes revealed from this work, however,

may lead to better water management and consequently better fuel cell performance. Therefore, this may compensate the loss of fuel cell performance due to the membrane degradation. In addition, this interpretation of the water transport data of degraded membranes provides some insight into what membrane structures could be desirable for improving water permeation. For instance, to achieve high rates of water permeation, the polymer membranes should possess large water volume fraction (X_v) and more well-structured hydrophilic channels.

System two: shorter side chain version Nafion® membranes

Short side chain (SSC) perfluorosulfonic acid (PFSA) ionomer membrane is a shorter side chain analogue of Nafion®. It was found to exhibit improved fuel cell performance than Nafion® at the condition of reduced relative humidity and elevated operating temperature.[31,141] In Chapter 4, liquid and water vapor transport through a series of SSC PFSA membranes were measured as a function of membrane thickness (24-96 μm) and temperature (25- 85 °C). Water permeation fluxes of liquid-liquid (LLP), liquid-vapor (LVP) and vapor-vapor (VVP) exhibit larger values with thinner SSC membranes. Furthermore, SSC membranes were found to be more permeable than that of Nafion® membranes at 70 °C, 40% relative humidity (RH), which may provide an explanation to the better fuel cell performance that observed in SSC membranes at elevated temperature and low RH conditions.[31,141]

Internal ($R_{internal}$) and interfacial ($R_{interfacial}$) water permeation resistances were decoupled from the overall resistance. The importance of membrane interface was drawn. Within the SSC series, the increase in permeance for VVP upon decreasing membrane thickness was not as significant as compared to LLP, due to the larger interfacial water transport resistance ($R_{interfacial}$) at membrane/vapor interface. The study of LVP and VVP transport resistances indicated that $R_{interfacial}$ played a dominant role in determining the overall membrane resistance, even for a thick SSC membrane.

A depletion layer on the membrane surface was introduced. It is speculated that $R_{interfacial}$ was the result of water depletion layer caused by the dehydration at the membrane interface. The LVP interfacial resistance for SSC membranes was similar to that found for Nafion®, even though SSC membranes possessed significantly lower

internal LVP permeation resistance. In addition, SSC membranes possessed a greater ratio of $R_{LVP\_interfacial}$ to the overall LVP resistance than the Nafion® membranes for a normalized membrane thickness.

Water permeation was conducted under varied temperature conditions. The temperature was found to have a strong impact on water transport through SSC membranes. Water permeance values as determined by liquid-liquid (LLP), liquid-vapor (LVP) and vapor-vapor (VVP) measurements were all found to increase with temperature, due to the increase in water volume fraction (X_v) and effective hydrophilic pore size. The activation energy of LLP, LVP and VVP were calculated to be 16.3, 40.2 and 43.1 kJ $mol^{-1,}$ respectively, which was lower than that of Nafion® under similar conditions. These results could be beneficial for designing future materials for the application of higher operating temperature to optimizing fuel cell performance.[22,32,254]

System three: anion exchange membranes (AEMs)

Water permeation of an emerging class of anion exchange membranes, hexamethyl-*p*-terphenyl poly (dimethylbenzimidazolium) (HMT-PMBI) was examined. This type of AEM has good *in-situ* and *ex-situ* properties, and it is easy to synthetically scale-up.[138] A series of commercialized anion exchange membranes (AEMs) (i.e., Fumapem® FAA-3) and a series of proton exchange membranes (i.e., Nafion®) were used for comparison. As summarized in Chapter 5, for the same ion form, HMT-PMBI membrane showed significant higher LLP permeability (see Table 5.1) and moderate LVP permeability (summarized in Table 5.2) than Fumapem®. Compared to Nafion® in the H^+ form, HMT-PMBI in CO_3^{2-} form showed only 5% less of LVP permeability. In contrast, HMT-PMBI in OH^- form exhibited greater liquid-liquid (LLP) water permeability than Nafion® (H^+).

By measuring water permeation through membranes of different thicknesses, internal and interfacial water permeation resistances through *anion exchange membranes* were decoupled, for the first time. Interfacial permeation resistances for liquid-liquid water permeation (LLP) was found to be negligible compared to that for liquid-vapor water permeation (LVP) for both series of AEMs. Correspondingly, the resistance of LLP was one order of magnitude smaller compared to that of LVP.

HMT-PMBI (CO_3^{2-}) possessed larger effective internal water permeation coefficient than both Fumapem® FAA-3 (CO_3^{2-}) and Nafion® membranes (60 and 18% larger, respectively), by virtue of HMT-PMBI (CO_3^{2-}) possessing a higher water volume fraction (X_v). In contrast, the effective interfacial permeation coefficient of HMT-PMBI(CO_3^{2-}) was found to be similar to Fumapem® ((CO_3^{2-}), ± 5%) but smaller than Nafion®(H^+) (by 14%), despiting HMT-PMBI possessing lower surface water contact angle than Fumapem® or Nafion®.

Changing the degree of methylation of the polymers had a significant impact on internal and interfacial water permeation through HMT-PMBI membranes. However, spray-coating a catalyst layer on the membrane surface had a negligible impact on water permeation through the membrane internal and interface.

6.2. Further discussion and future work

Presented in this thesis were three main contributions that provide insight into the impact of membrane structure to water permeation property on the internal and interfacial of the membranes, as well as insight into future membrane designing to enhance water management. In this section, further discussions are made based on different experimental variables used in the three discussed membrane systems. The variables include experimental conditions (e.g., temperature, relative humidity, and hydraulic pressure) and membrane properties (e.g., membrane thickness and ion exchange capacity).

- For all the membranes studied, the water permeability of liquid-liquid, liquid-vapor and vapor-vapor permeation showed greater values at a higher temperature, as well as at the condition of larger gradients both in hydraulic pressure and relative humidity. These results were attributed to the greater transport driving force caused by increased chemical potential gradients at such conditions.

- Liquid water permeability was found to be greater than water vapor permeability for all the membranes studied in this thesis, which is consistent with reported results of

Nafion® membranes.[71,80] In addition, liquid water possessed a smaller permeation activation energy than that for water vapor.

- Higher water permeation rates were observed in short side chain (SSC) PFSA membranes (c.f., Nafion®) and HMT-PMBI membranes (c.f., Fumapem®) than their analogues, suggesting these two studied membranes are good candidates regarding efficient water management in fuel cells.

  An *in-situ* modeling study from Huo et al.[134] investigated water management in the anode of an anion exchange membrane fuel cell. Under the condition of 30 °C, 100% relative humidity (RH) at both electrodes, back water permeation flux (from the anode to the cathode) was found to be 2.25×10^{-3} mol m^{-2} s^{-1}. In fact, HMT-PMBI possessed liquid permeation flux of 8.7×10^{-3} mol m^{-2} s^{-1} under similar conditions, which is larger than Huo et al. reported for *in-situ* back-permeation flux, and is sufficient to permeate liquid water from the anode to the cathode.

  Ex-situ liquid-vapor water permeation (LVP) (comparable to the dry anode and the wet cathode in *in-situ*) was found to be more accurately reflects the internal water transport conditions occurring in an operating proton exchange membrane (i.e., Nafion®) fuel cell. Therefore, in the future, it will be very beneficial to perform *in-situ* water transport experiments in fuel cells containing these studied membranes and make comparisons with the current *ex-situ* study.

- Membrane thickness was found to play a significant role in water permeation. Water permeation flux was found to increase with decreasing thickness for all the membranes (i.e., PEMs and AEMs) studied in this work. These results suggest that better water management in thinner membranes than that of the thick membranes, which matches the concept of using of thinner membranes to optimizing fuel cell performance.[255]

- Internal and interfacial water permeation resistance were decoupled from the overall permeation resistance. The impact of interfacial resistance on water permeation was quantified in this thesis study. At membrane/liquid interface, both SSC PFSAs and AEMs exhibit the negligible interfacial water permeation resistance ($\mathrm{R_{interfacial}}$). In contrast, $\mathrm{R_{interfacial}}$ on membrane/vapor interface was found to dominate the overall

resistance, suggesting that membrane/vapor interface is the rate-limiting step for the overall water permeation.

The ratio of interfacial resistance to the overall permeation resistance ($R_{interfacial}/R$) for the two studied membrane systems under similar experimental condition were in the following order: system 1) short side chain (SSC) PFSA > long side chain PFSA (Nafion®), and system 2) HMT-PMBI > Fumapem® > Nafion®. Combining the results of these two membrane systems, it appears that the membranes with shorter side chain length showed larger values of $R_{interfacial}/R$. A possible reason could be attributed to the less-ordered water permeation pathway on the interface of the membranes with shorter side chain length.[198] However, more sophisticated techniques (e.g., conductive AFM) could be applied on the membrane interfaces to further understanding the current *ex-situ* water permeation results.

In conclusion, this thesis indicates that membranes with a smaller thickness, greater water volume fraction, and higher ion exchange capacity results in a higher overall water permeability. These parameters, however, do not dominate the interfacial water permeation of the membrane. In contrast, the side chain length of the polymer is found to influence these parameters. The membranes with longer side chain length appear to be more water permeable through the membrane interface. These results provide more understanding of the role of polymer structure on water permeation properties of ion exchange membranes.

6.2.1. Future work

Future work on the membrane interface can be done by quantifying the differences of structural and chemical properties, such as the amount of hydrophilic surface moieties as a function of relative humidity, some of which has been done in literature, but not under all relevant conditions.[41] For example, very recently, Hara et al. investigated surface ionic conductivity of anion exchange membranes using AFM under purified air at various relative humidities.[253] The distribution of the anion-conducting spots on the membrane surface was found to directly affect the performance of an anion exchange membrane (AEM) fuel cell. Therefore, further understanding of the membrane interface can be very

beneficial for studying the water permeation through membranes, and consequently better fuel cell performance. Furthermore, a negligible influence on water permeation was found after spray-coating a catalyst layer on HMT-PMBI membranes. In the future, it is useful to further study the impact of the interfacial layer upon the water permeation through the catalyst layer/membrane interface. For example, spray-coating a much thicker catalyst layer on the membrane and then investigating if this much thicker spray-coated layer would lead to any difference in water permeation.

Since the interfacial layer of the membrane has been found to play a critical role in water permeation through membranes in this study. Future work on modifying the membrane interface and consequently on interfacial water permeation will be performed from the perspective of the membrane casting process, such as changing the casting solvents, annealing temperature, and post-fabrication processes.[256,257]

In addition, efforts can be made in designing new polymer electrolyte materials aiming for the efficient water management of fuel cells. For instance, the polymer structures that have better nanophase segregation, such as graft copolymers with more hydrophilic grafts on the polymer chain,[258,259] block copolymers,[260-262] and polymer chains that contain multiple cations on single aromatic rings.[217]

Future areas to explore with the permeation of water through membranes can be extended to other promising polymer systems, such as quaternary ammonium based anion exchange membranes.[263] Additionally, measuring permeation of solvents other than water, such as ethanol and methanol, will be useful.

The results from this thesis work can be applied to decouple the water flux of electro-osmotic drag from the reported net *in-situ* water fluxes ($\mathrm{J_{net}}$). $\mathrm{J_{net}}$ was determined from the amount of water collected at each electrode.[71,80]. For instance, in the case of the anode of the proton exchange membrane (e.g., Nafion®) fuel cell, where water is consumed by electro-osmotic drag flux ($\mathrm{J_{EOD}}$) and compensated by back water permeation flux ($\mathrm{J_{WP}}$). Therefore, electro-osmotic drag flux ($\mathrm{J_{EOD}}$) can be separated from the measured net water flux of the anode ($\mathrm{J^{a}_{net}}$) using the following expressions:

$$J_{EOD}(mol\ cm^{-2}s^{-1}) = J^{a}_{net} - J_{WP} \qquad \text{Equation 6.1}$$

The electro-osmotic drag flux (J_{EOD}) can be calculated using Equation 6.2:

$$J_{EOD}(mol\ cm^{-2}s^{-1}) = \frac{j\ (A\ cm^{-2})\ N_d}{F\ (C\ mol^{-1})} \qquad \text{Equation 6.2}$$

where j, N_d and F represent current density, electro-osmotic drag coefficient and Faraday's constant, respectively.

Combining Equations 6.1 and 6.2, the values of electro-osmotic drag coefficient (N_d) can be extracted. Therefore, an in-depth understanding on the water transport behaviours in an operating fuel cell (*in-situ)* can be approached.

6.3. Limitations

The body of this thesis work focused on water transport through membranes based on macroscale experiments. However, these experiments were unable to capture the nanoscale effects. There are some techniques suited to studying nanoscale phenomena, such as small-angle X-ray and neutron scattering. These techniques determine the change in the spacing between water domains as a function of time during water uptake. However, it is questionable whether Fickian diffusion can be used for the growth of hydrophilic domain, as it involves processes like absorption of water molecules and accommodation of domains in the deformed polymer matrix. Even though more studies are needed to fully understand water transport at smaller length scales, there is evidence to suggest that microscopic diffusion processes are generally faster than the macroscopic ones.[41]

Water transport studies in this thesis work were based on free (moveable) water and did not able to capture the properties of the bound water. However, other techniques such as differential scanning calorimetry (DSC),[264,265] FTIR-ATR[266] and thermogravimetric analysis (TGA)[267] are suitable for this regard. Also, water permeation through membranes was studied in a simplified way, which was based on assuming local equilibrium where chemical potential was the only overall gradient. The study of other variables that not considered in this study, such as thermal and mechanical gradients can be found elsewhere.[2,268-271]

References

(1) G. Merle; Wessling, M.; Nijmeijer, K. *Journal of Membrane Science* **2011**, *377*, 1.

(2) M. Eikerling; Kulikovsky, A. In Polymer Electrolyte Fuel Cells: Physical Principles of Materials and Operation; CRC Press: **2014**, p 365.

(3) K. Scott; Shukla, A. K. *Reviews in Environmental Science and Bio/Technology*, **2004**, *3*, 273.

(4) S. J. Hamrock; Yandrasits, M. A. *Polymer Reviews* **2006**, *46*, 219.

(5) A. Z. Weber; Newman, J. Chemical Reviews 2004, 104, 4679.

(6) O. T. Holton; Stevenson, J. W. Platinum Metals Review 2013, 57.

(7) W. P. Teagan; Bentley, J.; Barnett, B. Journal of Power Sources 1998, 71, 80.

(8) L. Carrette; Friedrich, K. A.; Stimming, U. *Fuel Cells* **2001**, *1*, 5.

(9) C. S. Gittleman; Coms, F. D.; Lai, Y.-H. In *Polymer Electrolyte Fuel Cell Degradation*; Matthew, M., Emin Caglan, K., T. Nejat VezirogluA2 - Matthew Mench, E. C. K., Veziroglu, T. N., Eds.; Academic Press: Boston, **2012**, p 15.

(10) T. Ishimoto; Nagumo, R.; Ogura, T.; Ishihara, T.; Kim, B.; Miyamoto, A.; Koyama, M. *J Electrochem Soc* **2010**, *157*, B1305.

(11) J. Peron; Mani, A.; Zhao, X.; Edwards, D.; Adachi, M.; Soboleva, T.; Shi, Z.; Xie, Z.; Navessin, T.; Holdcroft, S. *Journal of Membrane Science* **2010**, *356*, 44.

(12) P. Berg; Promislow, K.; St. Pierre, J.; Stumper, J.; Wetton, B. *J Electrochem Soc* **2004**, *151*, A341.

(13) M. Adachi; Navessin, T.; Xie, Z.; Li, F. H.; Tanaka, S.; Holdcroft, S. *Journal of Membrane Science* **2010**, *364*, 183.

(14) M. G. Izenson; Hill, R. W. *Journal of Fuel Cell Science and Technology* **2004**, *2*, 1.

(15) M. Matthew *Fuel cell engines*; John Wiley & Sons, Inc., **2008**,87.

(16) D. L. Fritz; Allen, J. S. *ECS Transactions* **2009**, *25*, 49.

(17) S. S. Kocha; Deliang Yang, J.; Yi, J. S. *AIChE Journal* **2006**, *52*, 1916.

(18) R. Devanathan *Energy & Environmental Science* **2008**, *1*, 101.

(19) W. T. Grubb, US Patent 2,913,511, **1959**.

(20) H. Pu *Polymers for PEM Fuel Cells*; John Wiley & Sons, **2014**, 92.

(21) K. A. Mauritz; Moore, R. B. *Chemical Reviews* **2004**, *104*, 4535.

(22) S. Bose; Kuila, T.; Nguyen, T. X. H.; Kim, N. H.; Lau, K.-t.; Lee, J. H. *Progress in Polymer Science* **2011**, *36*, 813.

(23) M. P. Rodgers; Shi, Z.; Holdcroft, S. *Fuel Cells* **2009**, *9*, 534.

(24) B. Mecheri; Felice, V.; Zhang, Z.; D'Epifanio, A.; Licoccia, S.; Tavares, A. C. *The Journal of Physical Chemistry C* **2012**, *116*, 20820.

(25) B. Mecheri; Felice, V.; D'Epifanio, A.; Tavares, A.; Licoccia, S. *ECS Transactions* **2011**, *35*, 99.

(26) B. Muriithi; Loy, D. A. *ACS Applied Materials & Interfaces* **2012**, *4*, 6766.

(27) N. H. Jalani; Datta, R. *Journal of Membrane Science* **2005**, *264*, 167.

(28) M. Moradi; Moheb, A.; Javanbakht, M.; Hooshyari, K. *International Journal of Hydrogen Energy* **2016**, *41*, 2896.

(29) G.-B. Jung; Tseng, C.-C.; Yeh, C.-C.; Lin, C.-Y. *International Journal of Hydrogen Energy* **2012**, *37*, 13645.

(30) X. Li; Ma, H.; Wang, H.; Zhang, S.; Jiang, Z.; Liu, B.; Guiver, M. D. *RSC Advances* **2015**, *5*, 53870.

(31) J. Peron; Edwards, D.; Haldane, M.; Luo, X.; Zhang, Y.; Holdcroft, S.; Shi, Z. *Journal of Power Sources* **2011**, *196*, 179.

(32) A. S. Aricò; Di Blasi, A.; Brunaccini, G.; Sergi, F.; Dispenza, G.; Andaloro, L.; Ferraro, M.; Antonucci, V.; Asher, P.; Buche, S.; Fongalland, D.; Hards, G. A.; Sharman, J. D. B.; Bayer, A.; Heinz, G.; Zandonà, N.; Zuber, R.; Gebert, M.; Corasaniti, M.; Ghielmi, A.; Jones, D. J. *Fuel Cells* **2010**, *10*, 1013.

(33) R. B. Moore; Martin, C. R. *Macromolecules* **1989**, *22*, 3594.

(34) X. Luo; Holdcroft, S.; Mani, A.; Zhang, Y.; Shi, Z. *Physical Chemistry Chemical Physics* **2011**, *13*, 18055.

(35) J. Li; Pan, M.; Tang, H. *RSC Advances* **2014**, *4*, 3944.

(36) L. Ghassemzadeh; Marrony, M.; Barrera, R.; Kreuer, K. D.; Maier, J.; Müller, K. *Journal of Power Sources* **2009**, *186*, 334.

(37) L. Yu; Lin, F.; Xu, L.; Xi, J. *RSC Advances* **2016**, *6*, 3756.

(38) N. Rajalakshmi; Dhathathreyan, K. S. *Chemical Engineering Journal* **2007**, *129*, 31.

(39) K. Lee; Zhang, L.; Zhang, J. In *PEM Fuel Cell Electrocatalysts and Catalyst Layers: Fundamentals and Applications*; Zhang, J., Ed.; Springer Science & Business Media: **2008**; p 6.

(40) P. Gerald; Claude, G. *Proton Conductors: Solids, Membranes and Gels - Materials and Devices*; Cambridge University Press**1992**; 300.

(41) K. Ahmet; Adam, Z. W. In *Polymers for Energy Storage and Delivery: Polyelectrolytes for Batteries and Fuel Cells*; American Chemical Society: **2012**; Vol. 1096, p 175.

(42) M. A. Hickner; Pivovar, B. S. *Fuel Cells* **2005**, *5*, 213.

(43) K. D. Kreuer *Journal of Membrane Science* **2001**, *185*, 29.

(44) T. D. Gierke; Munn, G. E.; Wilson, F. C. *Journal of Polymer Science: Polymer Physics Edition* **1981**, *19*, 1687.

(45) T. D. Gierke; Munn, G. E.; Wilson, F. C. *J. Polym. Sci., Polym. Phys. Ed.* **1981**, *19*, 1687.

(46) G. Gebel *Polymer* **2000**, *41*, 5829.

(47) L. Rubatat; Rollet, A. L.; Gebel, G.; Diat, O. *Macromolecules* **2002**, *35*, 4050.

(48) M.-H. Kim; Glinka, C. J.; Grot, S. A.; Grot, W. G. *Macromolecules* **2006**, *39*, 4775.

(49) K.-D. Kreuer; Portale, G. *Advanced Functional Materials* **2013**, *23*, 5390.

(50) F. I. Allen; Comolli, L. R.; Kusoglu, A.; Modestino, M. A.; Minor, A. M.; Weber, A. Z. *ACS Macro Letters* **2015**, *4*, 1.

(51) D. Wu; Paddison, S. J.; Elliott, J. A. *Macromolecules* **2009**, *42*, 3358.

(52) K. D. Kreuer; Schuster, M.; Obliers, B.; Diat, O.; Traub, U.; Fuchs, A.; Klock, U.; Paddison, S. J.; Maier, J. *Journal of Power Sources* **2008**, *178*, 499.

(53) S. J. Paddison; Elliott, J. A. *The Journal of Physical Chemistry A* **2005**, *109*, 7583.

(54) B. Loppinet; Gebel, G. *Langmuir* **1998**, *14*, 1977.

(55) R. Y. M. Huang; Shao, P.; Feng, X.; Burns, C. M. *Journal of Membrane Science* **2001**, *192*, 115.

(56) Z. Lu; Polizos, G.; Macdonald, D. D.; Manias, E. *J Electrochem Soc* **2008**, *155*, B163.

(57) Y. S. Kim; Dong, L.; Hickner, M. A.; Glass, T. E.; Webb, V.; McGrath, J. E. *Macromolecules* **2003**, *36*, 6281.

(58) A. Siu; Schmeisser, J.; Holdcroft, S. *The Journal of Physical Chemistry B* **2006**, *110*, 6072.

(59) A. Roudgar; Narasimachary, S. P.; Eikerling, M. *The Journal of Physical Chemistry B* **2006**, *110*, 20469.

(60) K.-D. Kreuer *Chemistry of Materials* **1996**, *8*, 610.

(61) P. Choi; Jalani, N. H.; Thampan, T. M.; Datta, R. *Journal of Polymer Science Part B: Polymer Physics* **2006**, *44*, 2183.

(62) K.-D. Kreuer; Rabenau, A.; Weppner, W. *Angewandte Chemie International Edition in English* **1982**, *21*, 208.

(63) K. D. Kreuer *Solid State Ionics* **2000**, *136–137*, 149.

(64) S. Ge; Li, X.; Yi, B.; Hsing, I.-M. *J Electrochem Soc* **2005**, *152*, A1149.

(65) M. H. Eikerling; Berg, P. *Soft Matter* **2011**, *7*, 5976.

(66) T. J. Peckham; Schmeisser, J.; Rodgers, M.; Holdcroft, S. *Journal of Materials Chemistry* **2007**, *17*, 3255.

(67) T. Ous; Arcoumanis, C. *Journal of Power Sources* **2013**, *240*, 558.

(68) M. Eikerling; Kharkats, Y. I.; Kornyshev, A. A.; Volfkovich, Y. M. *J Electrochem Soc* **1998**, *145*, 2684.

(69) M. Eikerling *J Electrochem Soc* **2006**, *153*, E58.

(70) Z. Lu; Rath, C.; Zhang, G.; Kandlikar, S. G. *International Journal of Hydrogen Energy* **2011**, *36*, 9864.

(71) M. Adachi; Navessin, T.; Xie, Z.; Frisken, B.; Holdcroft, S. *J Electrochem Soc* **2009**, *156*, B782.

(72) T. Berning *International Journal of Hydrogen Energy* **2011**, *36*, 9341.

(73) F. Chen; Su, Y.-G.; Soong, C.-Y.; Yan, W.-M.; Chu, H.-S. *Journal of Electroanalytical Chemistry* **2004**, *566*, 85.

(74) K.-H. Choi; Peck, D.-H.; Kim, C. S.; Shin, D.-R.; Lee, T.-H. *Journal of Power Sources* **2000**, *86*, 197.

(75) W. Dai; Wang, H.; Yuan, X.-Z.; Martin, J. J.; Yang, D.; Qiao, J.; Ma, J. *International Journal of Hydrogen Energy* **2009**, *34*, 9461.

(76) D. García-Nieto; Barragán, V. M. *Electrochimica Acta* **2015**, *154*, 166.

(77) S. Qu; Li, X.; Ke, C.; Shao, Z.-G.; Yi, B. *Journal of Power Sources* **2010**, *195*, 6629.

(78) A. Z. Weber; Newman, J. *J Electrochem Soc* **2003**, *150*, A1008.

(79) S. Deabate; Gebel, G.; Huguet, P.; Morin, A.; Pourcelly, G. *Energy & Environmental Science* **2012**, *5*, 8824.

(80) M. Adachi *PhD thesis* **Spring 2010**, Simon Fraser University.

(81) J. T. A. Zawodzinski; Derouin, C.; Radzinski, S.; Sherman, R. J.; Smith, V. T.; Springer, T. E.; Gottesfeld, S. *J Electrochem Soc* **1993**, *140*, 1041.

(82) A. S. Nistor, George; Racles, Carmen; Cazacu, Maria *Materiale Plastice (Bucharest, Romania)* **2011**, *48*, 33.

(83) P. W. Majsztrik; Satterfield, M. B.; Bocarsly, A. B.; Benziger, J. B. *Journal of Membrane Science* **2007**, *301*, 93.

(84) P. Majsztrik; Satterfield, B.; Bocarsly, A.; Benziger, J. B. *ECS Transactions* **2007**, *11*, 609.

(85) P. Majsztrik; Bocarsly, A.; Benziger, J. *The Journal of Physical Chemistry B* **2008**, *112*, 16280.

(86) N. Zhao; Edwards, D.; Shi, Z.; Holdcroft, S. *ECS Electrochemistry Letters* **2013**, *2*, F22.

(87) T. Romero; Mérida, W. *Journal of Membrane Science* **2009**, *338*, 135.

(88) K. Aotani; Miyazaki, S.-i.; Kubo, N.; Katsuta, M. *ECS Transactions* **2008**, *16*, 341.

(89) V. Baglio; Aricò, A. S.; Antonucci, V.; Nicotera, I.; Oliviero, C.; Coppola, L.; Antonucci, P. L. *Journal of Power Sources* **2006**, *163*, 52.

(90) X. Gong; Bandis, A.; Tao, A.; Meresi, G.; Wang, Y.; Inglefield, P. T.; Jones, A. A.; Wen, W. Y. *Polymer* **2001**, *42*, 6485.

(91) A. Guillermo; Gebel, G. r.; Mendil-Jakani, H.; Pinton, E. *The Journal of Physical Chemistry B* **2009**, *113*, 6710.

(92) R. Duplessix; Escoubes, M.; Rodmacq, B.; Volino, F.; Roche, E.; Eisenberg, A.; Pineri, M. In *Water in Polymers*; AMERICAN CHEMICAL SOCIETY: **1980**; Vol. 127, p 469.

(93) T. Takamatsu; Hashiyama, M.; Eisenberg, A. *Journal of Applied Polymer Science* **1979**, *24*, 2199.

(94) D. Rivin; Kendrick, C. E.; Gibson, P. W.; Schneider, N. S. *Polymer* **2001**, *42*, 623.

(95) D. J. Burnett; Garcia, A. R.; Thielmann, F. *Journal of Power Sources* **2006**, *160*, 426.

(96) D. T. Hallinan; Elabd, Y. A. *The Journal of Physical Chemistry B* **2009**, *113*, 4257.

(97) M. B. Satterfield; Benziger, J. B. *The Journal of Physical Chemistry B* **2008**, *112*, 3693.

(98) A. Kongkanand *The Journal of Physical Chemistry C* **2011**, *115*, 11318.

(99) P. M. Mangiagli; Ewing, C. S.; Xu, K.; Wang, Q.; Hickner, M. A. *Fuel Cells* **2009**, *9*, 432.

(100) T. E. Springer; Zawodzinski, T. A.; Gottesfeld, S. *J Electrochem Soc* **1991**, *138*, 2334.

(101) T. Okada; Xie, G.; Gorseth, O.; Kjelstrup, S.; Nakamura, N.; Arimura, T. *Electrochimica Acta* **1998**, *43*, 3741.

(102) N. Grossi; Espuche, E.; Escoubes, M. *Separation and Purification Technology* **2001**, *22–23*, 255.

(103) X. Ye; Douglas LeVan, M. *Journal of Membrane Science* **2003**, *221*, 147.

(104) C. W. Monroe; Romero, T.; Mérida, W.; Eikerling, M. *Journal of Membrane Science* **2008**, *324*, 1.

(105) N. S. Schneider; Rivin, D. *Polymer* **2010**, *51*, 671.

(106) B. Kientiz; Yamada, H.; Nonoyama, N.; Weber, A. Z. *Journal of Fuel Cell Science and Technology* **2011**, *8*, 011013.

(107) S. Hietala; Maunu, S. L.; Sundholm, F. *Journal of Polymer Science Part B: Polymer Physics* **2000**, *38*, 3277.

(108) M. Saito; Arimura, N.; Hayamizu, K.; Okada, T. *The Journal of Physical Chemistry B* **2004**, *108*, 16064.

(109) J. E. Hensley; Way, J. D. *Journal of Power Sources* **2007**, *172*, 57.

(110) T. Ohkubo; Kidena, K.; Ohira, A. *Macromolecules* **2008**, *41*, 8688.

(111) S. Ochi; Kamishima, O.; Mizusaki, J.; Kawamura, J. *Solid State Ionics* **2009**, *180*, 580.

(112) K. Kidena; Ohkubo, T.; Takimoto, N.; Ohira, A. *European Polymer Journal* **2010**, *46*, 450.

(113) Q. Zhao; Majsztrik, P.; Benziger, J. *The Journal of Physical Chemistry B* **2011**, *115*, 2717.

(114) Y. Tabuchi; Ito, R.; Tsushima, S.; Hirai, S. *Journal of Power Sources* **2011**, *196*, 652.

(115) P. Choi; Jalani, N. H.; Datta, R. *J Electrochem Soc* **2005**, *152*, E84.

(116) V. Stannett *Journal of Membrane Science* **1978**, *3*, 97.

(117) L. Schreiber; Schonherr, J. In *Water and Solute Permeability of Plant Cuticles: Measurement and Data Analysis*; Springer Berlin Heidelberg: Berlin, Heidelberg, **2009**, p 53.

(118) N. E. Schlotter; Furlan, P. Y. *Polymer* **1992**, *33*, 3323.

(119) C. A. Kumins *Journal of Polymer Science Part C: Polymer Symposia* **1965**, *10*, 1.

(120) J. Park; Shin, J. H.; Park, J.-K. *Analytical Chemistry* **2016**, *88*, 3781.

(121) L. W. McKeen In *Permeability Properties of Plastics and Elastomers (Third Edition)*; William Andrew Publishing: Oxford, **2012**, p 1.

(122) J. G. Wijmans; Baker, R. W. *Journal of Membrane Science* **1995**, *107*, 1.

(123) Q. Duan; Wang, H.; Benziger, J. *Journal of Membrane Science* **2012**, *392–393*, 88.

(124) K. Jiao and X. Li, *Progress in Energy and Combustion Science*, **2011**, 37, 221-291.

(125) M. Bass; Berman, A.; Singh, A.; Konovalov, O.; Freger, V. *The Journal of Physical Chemistry B* **2010**, *114*, 3784.

(126) V. Freger *The Journal of Physical Chemistry B* **2008**, *113*, 24.

(127) M. Bass; Berman, A.; Singh, A.; Konovalov, O.; Freger, V. *Macromolecules* **2011**, *44*, 2893.

(128) B. Kientiz; Yamada, H.; Nonoyama, N.; Weber, A. Z. *Journal of Fuel Cell Science and Technology* **2011**, *8*, 011013.

(129) J. Tang; Yuan, W.; Zhang, J.; Li, H.; Zhang, Y. *RSC Advances* **2013**, *3*, 8947.

(130) A. Z. Weber; Newman, J. *J Electrochem Soc* **2004**, *151*, A311.

(131) M. Bass; Freger, V. *Polymer* **2008**, *49*, 497.

(132) Q. He; Kusoglu, A.; Lucas, I. T.; Clark, K.; Weber, A. Z.; Kostecki, R. *The Journal of Physical Chemistry B* **2011**, *115*, 11650.

(133) J. R. O'Dea; Economou, N. J.; Buratto, S. K. *Macromolecules* **2013**, *46*, 2267.

(134) S. Huo; Deng, H.; Chang, Y.; Jiao, K. *International Journal of Hydrogen Energy* **2012**, *37*, 18389.

(135) M. Ji; Wei, Z. *Energies* **2009**, *2*, 1057.

(136) H.-S. Shiau; Zenyuk, I. V.; Weber, A. Z. *ECS Transactions* **2015**, *69*, 985.

(137) X. Luo; Holdcroft, S. *Journal of Membrane Science* **2016**, *520*, 155.

(138) A. G. Wright; Fan, J.; Britton, B.; Weissbach, T.; Lee, H.-F.; Kitching, E. A.; Peckham, T. J.; Holdcroft, S. *Energy & Environmental Science* **2016**, *9*, 2130.

(139) A. G. Wright; Holdcroft, S. *ACS Macro Letters* **2014**, *3*, 444.

(140) G. Job; Herrmann, F. *European Journal of Physics* **2006**, *27*, 353.

(141) N. Zhao; Edwards, D.; Lei, C.; Wang, K.; Li, J.; Zhang, Y.; Holdcroft, S.; Shi, Z. *Journal of Power Sources* **2013**, *242*, 877.

(142) R. W. Baker; Wijmans, J. G.; Huang, Y. *Journal of Membrane Science* **2010**, *348*, 346.

(143) J. G. Wijmans *Journal of Membrane Science* **2003**, *220*, 1.

(144) T. J. Peckham; Schmeisser, J.; Holdcroft, S. *The Journal of Physical Chemistry B* **2008**, *112*, 2848.

(145) L. A. Zook; Leddy, J. *Analytical Chemistry* **1996**, *68*, 3793.

(146) V. M. Barragán; Ruíz-Bauzá, C.; Villaluenga, J. P. G.; Seoane, B. *Journal of Colloid and Interface Science* **2004**, *277*, 176.

(147) R. Borup; Meyers, J.; Pivovar, B.; Kim, Y. S.; Mukundan, R.; Garland, N.; Myers, D.; Wilson, M.; Garzon, F.; Wood, D.; Zelenay, P.; More, K.; Stroh, K.; Zawodzinski, T.; Boncella, J.; McGrath, J. E.; Inaba, M.; Miyatake, K.; Hori, M.; Ota, K.; Ogumi, Z.; Miyata, S.; Nishikata, A.; Siroma, Z.; Uchimoto, Y.; Yasuda, K.; Kimijima, K.-i.; Iwashita, N. *Chemical Reviews* **2007**, *107*, 3904.

(148) J. Healy; Hayden, C.; Xie, T.; Olson, K.; Waldo, R.; Brundage, M.; Gasteiger, H.; Abbott, J. *Fuel Cells* **2005**, *5*, 302.

(149) C. Lim; Ghassemzadeh, L.; Van Hove, F.; Lauritzen, M.; Kolodziej, J.; Wang, G. G.; Holdcroft, S.; Kjeang, E. *Journal of Power Sources* **2014**, *257*, 102.

(150) T. H. Yu; Sha, Y.; Liu, W.-G.; Merinov, B. V.; Shirvanian, P.; Goddard, W. A. *Journal of the American Chemical Society* **2011**, *133*, 19857.

(151) M. Danilczuk; Coms, F. D.; Schlick, S. *The Journal of Physical Chemistry B* **2009**, *113*, 8031.

(152) A. Laconti; Liu, H.; Mittelsteadt, C.; McDonald, R. *ECS Transactions* **2006**, *1*, 199.

(153) L. Ghassemzadeh; Holdcroft, S. *Journal of the American Chemical Society* **2013**, *135*, 8181.

(154) M. Danilczuk; Coms, F. D.; Schlick, S. *Fuel Cells* **2008**, *8*, 436.

(155) F. D. Coms *ECS Transactions* **2008**, *16*, 235.

(156) A. Pozio; Silva, R. F.; De Francesco, M.; Giorgi, L. *Electrochimica Acta* **2003**, *48*, 1543.

(157) C. Chen; Levitin, G.; Hess, D. W.; Fuller, T. F. *Journal of Power Sources* **2007**, *169*, 288.

(158) L. Gubler; Dockheer, S. M.; Koppenol, W. H. *ECS Transactions* **2011**, *41*, 1431.

(159) D. E. Curtin; Lousenberg, R. D.; Henry, T. J.; Tangeman, P. C.; Tisack, M. E. *Journal of Power Sources* **2004**, *131*, 41.

(160) C. Zhou; Guerra, M. A.; Qiu, Z.-M.; Zawodzinski, T. A.; Schiraldi, D. A. *Macromolecules* **2007**, *40*, 8695.

(161) Y. Akiyama; Sodaye, H.; Shibahara, Y.; Honda, Y.; Tagawa, S.; Nishijima, S. *Journal of Power Sources* **2010**, *195*, 5915.

(162) S. H. Almeida; Kawano, Y. *Polymer Degradation and Stability* **1998**, *62*, 291.

(163) F. M. Collette; Lorentz, C.; Gebel, G.; Thominette, F. *Journal of Membrane Science* **2009**, *330*, 21.

(164) F. M. Collette; Thominette, F.; Mendil-Jakani, H.; Gebel, G. *Journal of Membrane Science* **2013**, *435*, 242.

(165) L. Ghassemzadeh; Peckham, T. J.; Weissbach, T.; Luo, X.; Holdcroft, S. *Journal of the American Chemical Society* **2013**, *135*, 15923.

(166) M. P. Rodgers; Bonville, L. J.; Kunz, H. R.; Slattery, D. K.; Fenton, J. M. *Chemical Reviews* **2012**, *112*, 6075.

(167) J. Qiao; Saito, M.; Hayamizu, K.; Okada, T. *J Electrochem Soc* **2006**, *153*, A967.

(168) K. Hongsirikarn; Mo, X.; Goodwin Jr, J. G.; Creager, S. *Journal of Power Sources* **2011**, *196*, 3060.

(169) M. A. Quiroga; Malek, K.; Franco, A. A. *J Electrochem Soc* **2016**, *163*, F59.

(170) M. Marrony; Barrera, R.; Quenet, S.; Ginocchio, S.; Montelatici, L.; Aslanides, A. *Journal of Power Sources* **2008**, *182*, 469.

(171) C. Bas; Flandin, L.; Danerol, A. S.; Claude, E.; Rossinot, E.; Alberola, N. D. *Journal of Applied Polymer Science* **2010**, *117*, 2121.

(172) V. Eswaraiah; Balasubramaniam, K.; Ramaprabhu, S. *Journal of Materials Chemistry* **2011**, *21*, 12626.

(173) D. A. Caulk; Brenner, A. M.; Clapham, S. M. *J Electrochem Soc* **2012**, *159*, F518.

(174) T. F. Fuller; Newman, J. *J Electrochem Soc* **1992**, *139*, 1332.

(175) S. Koter *Journal of Membrane Science* **2000**, *166*, 127.

(176) M. V. Bagal; Gogate, P. R. *Ultrasonics Sonochemistry* **2014**, *21*, 1.

(177) Y. Watanabe; Nakashima, Y. *Journal of Groundwater Hydrology* **2001**, *43*, 13.

(178) T. J. Peckham; Holdcroft, S. *Advanced Materials* **2010**, *22*, 4660.

(179) M. Eikerling; Kornyshev, A. A. *Journal of Electroanalytical Chemistry* **2001**, *502*, 1.

(180) A. Mani; Holdcroft, S. *Journal of Electroanalytical Chemistry* **2011**, *651*, 211.

(181) C. Zhang; Zhou, W.; Zhang, L.; Chan, S. H.; Wang, Y. *International Journal of Hydrogen Energy* **2015**, *40*, 4666.

(182) A. S. Aricò; Stassi, A.; Modica, E.; Ornelas, R.; Gatto, I.; Passalacqua, E.; Antonucci, V. *Journal of Power Sources* **2008**, *178*, 525.

(183) A. S. Aricò; Baglio, V.; Lufrano, F.; Stassi, A.; Gatto, I.; Antonucci, V.; Merlo, L. In *High Temperature Polymer Electrolyte Membrane Fuel Cells: Approaches, Status, and Perspectives*; Li, Q., Aili, D., Hjuler, H. A., Jensen, J. O., Eds.; Springer International Publishing: Cham, **2016**, p 5.

(184) M. Gebert; Ghielmi, A.; Merlo, L.; Corasaniti, M.; Arcella, V. *ECS Transactions* **2010**, *26*, 279.

(185) J. Peron; Edwards, D.; Haldane, M.; Luo, X. Y.; Zhang, Y. M.; Holdcroft, S.; Shi, Z. Q. *Journal of Power Sources* **2011**, *196*, 179.

(186) M. G. De Angelis; Lodge, S.; Giacinti Baschetti, M.; Sarti, G. C.; Doghieri, F.; Sanguineti, A.; Fossati, P. *Desalination* **2006**, *193*, 398.

(187) D. Gorri; De Angelis, M. G.; Giacinti Baschetti, M.; Sarti, G. C. *Journal of Membrane Science* **2008**, *322*, 383.

(188) Y. Jeon; Hwang, H.-k.; Park, J.; Hwang, H.; Shul, Y.-G. *International Journal of Hydrogen Energy* **2014**, *39*, 11690.

(189) R. Devanathan; Dupuis, M. *Physical Chemistry Chemical Physics* **2012**, *14*, 11281.

(190) E. E. Boakye; Yeager, H. L. *Journal of Membrane Science* **1992**, *69*, 155.

(191) V. Arcella; Ghielmi, A.; Tommasi, G. *Annals of the New York Academy of Sciences* **2003**, *984*, 226.

(192) M. Eikerling; Kornyshev, A. A.; Kuznetsov, A. M.; Ulstrup, J.; Walbran, S. *The Journal of Physical Chemistry B* **2001**, *105*, 3646.

(193) K.-D. Kreuer *Solid State Ionics* **2013**, *252*, 93.

(194) T. A. Zawodzinski, Jr.; Gottesfeld, S.; Shoichet, S.; McCarthy, T. J. *Journal of Applied Electrochemistry* **1993**, *23*, 86.

(195) T. Van Nguyen; Nguyen, M. V.; Lin, G.; Rao, N.; Xie, X.; Zhu, D.-M. *Electrochemical and Solid-State Letters* **2006**, *9*, A88.

(196) G. A. Giffin; Haugen, G. M.; Hamrock, S. J.; Di Noto, V. *Journal of the American Chemical Society* **2012**, *135*, 822.

(197) N. J. Economou; O'Dea, J. R.; McConnaughy, T. B.; Buratto, S. K. *RSC Advances* **2013**, *3*, 19525.

(198) G. Beamson; Alexander, M. R. *Surface and Interface Analysis* **2004**, *36*, 323.

(199) X. Luo; Ghassemzadeh, L.; Holdcroft, S. *International Journal of Hydrogen Energy* **2015**, *40*, 16714.

(200) R. Jiang; Mittelsteadt, C. K.; Gittleman, C. S. *J Electrochem Soc* **2009**, *156*, B1440.

(201) M. J. Cheah; Kevrekidis, I. G.; Benziger, J. *The Journal of Physical Chemistry B* **2011**, *115*, 10239.

(202) S. A. Eastman; Kim, S.; Page, K. A.; Rowe, B. W.; Kang, S.; Soles, C. L.; Yager, K. G. *Macromolecules* **2012**, *45*, 7920.

(203) G. S. Hwang; Parkinson, D. Y.; Kusoglu, A.; MacDowell, A. A.; Weber, A. Z. *ACS Macro Letters* **2013**, *2*, 288.

(204) M. Thomas; Escoubes, M.; Esnault, P.; Pineri, M. *Journal of Membrane Science* **1989**, *46*, 57.

(205) Y. Yamamoto; Ferrari, M. C.; Baschetti, M. G.; De Angelis, M. G.; Sarti, G. C. *Desalination* **2006**, *200*, 636.

(206) M. J. Park; Downing, K. H.; Jackson, A.; Gomez, E. D.; Minor, A. M.; Cookson, D.; Weber, A. Z.; Balsara, N. P. *Nano Letters* **2007**, *7*, 3547.

(207) S. S. Jang; Molinero, V.; Çağın, T.; Goddard, W. A. *The Journal of Physical Chemistry B* **2004**, *108*, 3149.

(208) G. F. Brunello; Mateker, W. R.; Lee, S. G.; Choi, J. I.; Jang, S. S. *Journal of Renewable and Sustainable Energy* **2011**, *3*, 043111.

(209) H. Xu; Kunz, H. R.; Bonville, L. J.; Fenton, J. M. *J Electrochem Soc* **2007**, *154*, B271.

(210) S. Lu; Pan, J.; Zhuang, L.; Lu, J. *Meeting Abstracts* **2008**, *MA2008-02*, 1075.

(211) M. Cifrain; Kordesch, K. In *Handbook of Fuel Cells – Fundamentals, Technology and Applications*; Vielstich, W., Lamm, A., Gasteiger, H. A., Eds.; John Wiley & Sons, Ltd, Chichester: **2003**; Vol. 1, p 267.

(212) J. B. Goodenough *Advanced Materials* **1996**, *8*, 866.

(213) X. Cheng; Shi, Z.; Glass, N.; Zhang, L.; Zhang, J.; Song, D.; Liu, Z.-S.; Wang, H.; Shen, J. *Journal of Power Sources* **2007**, *165*, 739.

(214) J. R. Varcoe; Atanassov, P.; Dekel, D. R.; Herring, A. M.; Hickner, M. A.; Kohl, P. A.; Kucernak, A. R.; Mustain, W. E.; Nijmeijer, K.; Scott, K.; Xu, T.; Zhuang, L. *Energy & Environmental Science* **2014**, *7*, 3135.

(215) M. A. Hickner; Herring, A. M.; Coughlin, E. B. *Journal of Polymer Science Part B: Polymer Physics* **2013**, *51*, 1727.

(216) X. Ren; Price, S. C.; Jackson, A. C.; Pomerantz, N.; Beyer, F. L. *ACS Applied Materials & Interfaces* **2014**, *6*, 13330.

(217) E. A. Weiber; Jannasch, P. *ChemSusChem* **2014**, *7*, 2621.

(218) K. W. Han; Ko, K. H.; Abu-Hakmeh, K.; Bae, C.; Sohn, Y. J.; Jang, S. S. *The Journal of Physical Chemistry C* **2014**, *118*, 12577.

(219) O. D. Thomas; Soo, K. J. W. Y.; Peckham, T. J.; Kulkarni, M. P.; Holdcroft, S. *Journal of the American Chemical Society* **2012**, *134*, 10753.

(220) L.-c. Jheng; Hsu, S. L.-c.; Lin, B.-y.; Hsu, Y.-l. *Journal of Membrane Science* **2014**, *460*, 160.

(221) X. Yan; Gu, S.; He, G.; Wu, X.; Zheng, W.; Ruan, X. *Journal of Membrane Science* **2014**, *466*, 220.

(222) B. Zhang; Gu, S.; Wang, J.; Liu, Y.; Herring, A. M.; Yan, Y. *RSC Advances* **2012**, *2*, 12683.

(223) Y. Zha; Disabb-Miller, M. L.; Johnson, Z. D.; Hickner, M. A.; Tew, G. N. *Journal of the American Chemical Society* **2012**, *134*, 4493.

(224) T. A. Zawodzinski; Neeman, M.; Sillerud, L. O.; Gottesfeld, S. *The Journal of Physical Chemistry* **1991**, *95*, 6040.

(225) Y. Zhao; Yoshimura, K.; Shishitani, H.; Yamaguchi, S.; Tanaka, H.; Koizumi, S.; Szekely, N.; Radulescu, A.; Richter, D.; Maekawa, Y. *Soft Matter* **2016**, *12*, 1567.

(226) V. D. Noto; Giffin, G. A.; Vezzu, K.; Nawn, G.; Bertasi, F.; Tsai, T.-h.; Maes, A. M.; Seifert, S.; Coughlin, E. B.; Herring, A. M. *Physical Chemistry Chemical Physics* **2015**, *17*, 31125.

(227) Y. Li; Liu, Y.; Savage, A. M.; Beyer, F. L.; Seifert, S.; Herring, A. M.; Knauss, D. M. *Macromolecules* **2015**, *48*, 6523.

(228) M. Tuckerman; Laasonen, K.; Sprik, M.; Parrinello, M. *The Journal of Chemical Physics* **1995**, *103*, 150.

(229) D. Marx *ChemPhysChem* **2007**, *8*, 209.

(230) K. N. Grew; Chiu, W. K. S. *J Electrochem Soc* **2010**, *157*, B327.

(231) C. Chen; Tse, Y.-L. S.; Lindberg, G. E.; Knight, C.; Voth, G. A. *Journal of the American Chemical Society* **2016**, *138*, 991.

(232) M. E. Tuckerman; Marx, D.; Parrinello, M. *Nature* **2002**, *417*, 925.

(233) K. M. Hugar; Kostalik, H. A.; Coates, G. W. *Journal of the American Chemical Society* **2015**, *137*, 8730.

(234) M. A. Vandiver; Caire, B. R.; Pandey, T. P.; Li, Y.; Seifert, S.; Kusoglu, A.; Knauss, D. M.; Herring, A. M.; Liberatore, M. W. *Journal of Membrane Science* **2016**, *497*, 67.

(235) Y. Liu; Wang, J.; Yang, Y.; Brenner, T. M.; Seifert, S.; Yan, Y.; Liberatore, M. W.; Herring, A. M. *The Journal of Physical Chemistry C* **2014**, *118*, 15136.

(236) A. G. Wright; Weissbach, T.; Holdcroft, S. *Angewandte Chemie International Edition* **2016**, *55*, 4818.

(237) V. J. Bharath; Millichamp, J.; Neville, T. P.; Mason, T. J.; Shearing, P. R.; Brown, R. J. C.; Manos, G.; Brett, D. J. L. *Journal of Membrane Science* **2016**, *497*, 229.

(238) T. D. Myles; Kiss, A. M.; Grew, K. N.; Peracchio, A. A.; Nelson, G. J.; Chiu, W. K. S. *J Electrochem Soc* **2011**, *158*, B790.

(239) T. D. Myles; Kiss, A.; Grew, K.; Peracchio, A.; Chiu, W. *ECS Transactions* **2010**, *33*, 1923.

(240) L. Zhu; Pan, J.; Wang, Y.; Han, J.; Zhuang, L.; Hickner, M. A. *Macromolecules* **2016**, *49*, 815.

(241) H.-S. Dang; Jannasch, P. *Macromolecules* **2015**, *48*, 5742.

(242) K. B. Daly; Benziger, J. B.; Panagiotopoulos, A. Z.; Debenedetti, P. G. *The Journal of Physical Chemistry B* **2014**, *118*, 8798.

(243) H. Azher; Scholes, C. A.; Stevens, G. W.; Kentish, S. E. *Journal of Membrane Science* **2014**, *459*, 104.

(244) M. Holz; Heil, S. R.; Sacco, A. *Physical Chemistry Chemical Physics* **2000**, *2*, 4740.

(245) C. E. Evans; Noble, R. D.; Nazeri-Thompson, S.; Nazeri, B.; Koval, C. A. *Journal of Membrane Science* **2006**, *279*, 521.

(246) Z.-H. Yang *RSC Advances* **2015**, *5*, 1213.

(247) M. G. Marino; Melchior, J. P.; Wohlfarth, A.; Kreuer, K. D. *Journal of Membrane Science* **2014**, *464*, 61.

(248) G. Dorenbos *Journal of Power Sources* **2015**, *276*, 328.

(249) M. Adachi; Romero, T.; Navessin, T.; Xie, Z.; Shi, Z.; Mérida, W.; Holdcroft, S. *Electrochemical and Solid-State Letters* **2010**, *13*, B51.

(250) Z. Zhang; Martin, J.; Wu, J.; Wang, H.; Promislow, K.; Balcom, B. J. *Journal of Magnetic Resonance* **2008**, *193*, 259.

(251) S. Tsushima; Ikeda, T.; Koido, T.; Hirai, S. *J Electrochem Soc* **2010**, *157*, B1814.

(252) Q. He; Ren, X. *Journal of Power Sources* **2012**, *220*, 373.

(253) M. Hara; Kimura, T.; Nakamura, T.; Shimada, M.; Ono, H.; Shimada, S.; Miyatake, K.; Uchida, M.; Inukai, J.; Watanabe, M. *Langmuir* **2016**, *32*, 9557.

(254) Y. Jin; Fujiwara, K.; Hibino, T. *Electrochemical and Solid-State Letters* **2010**, *13*, B8.

(255) S. Tsushima; Tsubota, A.; Tabuchi, Y.; Hirai, S. *ECS Transactions* **2009**, *25*, 1433.

(256) R. Guan; Dai, H.; Li, C.; Liu, J.; Xu, J. *Journal of Membrane Science* **2006**, *277*, 148.

(257) A. Sabetghadam; Mohammadi, T. *Polymer Engineering & Science* **2010**, *50*, 2392.

(258) J. Ran; Wu, L.; Lin, X.; Jiang, L.; Xu, T. *RSC Advances* **2012**, *2*, 4250.

(259) S. S. He; Frank, C. W. *Journal of Materials Chemistry A* **2014**, *2*, 16489.

(260) T.-H. Tsai; Maes, A. M.; Vandiver, M. A.; Versek, C.; Seifert, S.; Tuominen, M.; Liberatore, M. W.; Herring, A. M.; Coughlin, E. B. *Journal of Polymer Science Part B: Polymer Physics* **2013**, *51*, 1751.

(261) A. D. Mohanty; Ryu, C. Y.; Kim, Y. S.; Bae, C. *Macromolecules* **2015**, *48*, 7085.

(262) D.-Y. Park; Kohl, P. A.; Beckham, H. W. *The Journal of Physical Chemistry C* **2013**, *117*, 15468.

(263) X. Dong; Xue, B.; Qian, H.; Zheng, J.; Li, S.; Zhang, S. *Journal of Power Sources* **2017**, *342*, 605.

(264) S. J. Lue; Song-Jiang, S. *Journal of Macromolecular Science: Physics* **2009**, *48*, 114.

(265) I. Nicotera; Coppola, L.; Rossi, C. O.; Youssry, M.; Ranieri, G. A. *The Journal of Physical Chemistry B* **2009**, *113*, 13935.

(266) M.-C. Ferrari; Catalano, J.; Giacinti Baschetti, M.; De Angelis, M. G.; Sarti, G. C. *Macromolecules* **2012**, *45*, 1901.

(267) V. Saarinen; Kreuer, K. D.; Schuster, M.; Merkle, R.; Maier, J. *Solid State Ionics* **2007**, *178*, 533.

(268) R. Zaffou; Kunz, H. R.; Fenton, J. M. *ECS Transactions* **2006**, *3*, 909.

(269) S. Kim; Mench, M. M. *ECS Transactions* **2008**, *13*, 89.

(270) S. Kim; Mench, M. *ECS Transactions* **2008**, *16*, 575.

(271) R. S. Fu; Preston, J. S.; Pasaogullari, U.; Shiomi, T.; Miyazaki, S.; Tabuchi, Y.; Hussey, D. S.; Jacobson, D. L. *J Electrochem Soc* **2011**, *158*, B303.